Molecular Vibrational Dynamics in Solution Investigated by Stationary and Time-Resolved Infrared Spectroscopy

Dissertation
zur
Erlangung des Doktorgrades (Dr. rer. nat)
der
Mathematisch-Naturwissenschaftlichen Fakultät
der
Rheinischen Friedrich-Wilhelms-Universität Bonn

vorgelegt von
Jeannine Gleim
aus Hachenburg

Bonn
2021

Angefertigt mit Genhemigung der Mathematisch-Naturwissenschaftlichen Fakultät der Rheinischen Friedrich-Wilhelms Universität Bonn.

1. Gutachter: Prof. Dr. Peter Vöhringer
2. Gutachter: Prof. Dr. Barbara Kirchner

Tag der mündlichen Prüfung: 27.09.2021
Erscheinungsjahr: 2021

Contents

Abstract

Within this thesis, the time-resolved pump-probe and the two-dimensional mid-infrared spectroscopy were applied to investigate ultrafast processes in the condensed phase. Therefore, the stretching vibration ν_3 of the cyanate anion or the carbon dioxide were selected as a vibrational probe for the studies of their aqueous solutions under isobaric heating from 303 K up to 603 K. Herein, the time constants of the vibrational energy relaxation and the underlying mechanism were unraveled. For cyanate and carbon dioxide in aqueous solution, a solvent-assisted sequential intramolecular vibrational redistribution was considered. Within this mechanism, the vibrational excess energy is intramolecular redistributed from the initially excited ν_3 into the bending mode. From here, the energy is transferred to a solvent's resonant mode, where the excess energy is subsequently redistributed within the solvent. The time constants of the intermolecular energy transfer to the solvent's resonant mode were observed by the time-resolved pump-probe spectroscopy. In case of the CO_2/H_2O system, the time constant of the intramolecular energy redistribution was obtained from the correlation time used for the simulation of the temperature-dependent stationary infrared spectra based on the Kubo-Anderson general stochastic theory. The vibrational energy relaxation mechanisms of the investigated OCN^- and CO_2 aqueous solutions were then classified into and discussed in the context of the series of other pseudohalide anions, which were investigated earlier.

The two-dimensional mid-IR spectroscopy was applied to investigate the intramolecular dynamics of *trans*-4-methoxybut-3-en-2-one and its rotamers in C_2Cl_4. The ν(C=C) and the ν(C=O) stretching vibrations were used as vibrational probes. The two-dimensional infrared spectra were then analyzed in the context to assign the cross peaks to the corresponding vibrational modes of the different rotamers of this molecule. Furthermore, the conformational dynamics were investigated. The occurrence of additional cross peaks at the earliest delay time of 600 fs were attributed to a dimerization of two rotamers in solution.

Chapter 1

Introduction

Since the Nobel price in chemistry was awarded to A. H. Zewail *for his studies of the transition states of chemical reactions using femtosecond spectroscopy* in 1999 [1], the field of ultrafast spectroscopy established and resulted in numerous applications. Those are, for example, the absorption [2,3] and the emission spectroscopy [4,5], but also the photofragment spectroscopy [6–8] as an example. The focus of the field of the ultrafast spectroscopy is to address chemical reactions, involving displacements of charges, the rearrangement of atoms, the breaking and formation of bonds, such as covalent, ionic, hydrogen and van-der-Waals bonds [3, 9, 10]. All of these processes occur on a time scale of tens of femtoseconds to picoseconds describing a temporal range of molecular motions [11–13].

In the last decades, liquids and solutions were the systems under investigation [14–19]. The understanding of ultrafast processes in liquid phase is still limited because of the mixing of translational, vibrational and rotational degrees of freedom. Additionally, the solute-solvent interactions are complex considering the tight intermolecular packing of the molecules and associated many-body interactions [3, 10, 20–22].

For the investigation of ultrafast dynamics in solution, it is reasonable to use vibrational probes, which show characteristic interactions with light in the infrared (IR) spectral range. In the last decades, triatomic pseudohalide anions were often used as vibrational probes in different solvents [23–25]. Interactions with IR light result in excitations of the pseudohalides' ν_3 stretching vibrations at around 2000 cm^{-1} [23–28]. The excitation of these stretching vibrations are used as model systems [23–25] to investigate the interactions between the anions and the solvent as well as the vibrational energy relaxation (VER) mechanisms. Especially H_2O as a solvent is of particular interest due to its strong hydrogen bonds [3,10,15,20–22]. Phenomena such as dynamics within the solvent shell of the dissolved pseudohalide anions and the process of the vibrational energy redistribution within the hydrogen-bonded network of the solvent were investigated [23–25, 27, 28]. Within the studies of Hochstrasser and coworker [23],

Li et al. [26] and Lenchenkov et al. [24], the VER time constants of N_3^-, OCN^- and SCN^- in H_2O under ambient conditions were given. They observed that the relaxation time of the azide anion is faster than that of the cyanate or thiocyanate anion. Furthermore, they suggested that both, an intermolecular vibrational energy transfer (VET) from the solute to the solvent and an solvent-assisted intramolecular vibrational redistribution (IVR) are present in the systems. In the last years, the Vöhringer group investigated the azide [27,29,30], the thiocyanate [28,31,32] and the selenocyanate [32] anions dissolved in H_2O and D_2O for different thermodynamic conditions with the aim to clarify the underlying VER mechanisms. While under ambient conditions, a concurring of a VET and an IVR is present, the relaxation mechanism under non-ambient conditions resulted in a pure VET for the thiocyanate and selenocyanate anions in aqueous solutions [28, 32]. The cyanate anion as a further pseudohalide anion was not investigated under non-ambient conditions yet. Therefore, it will be studied under isobaric heating at a pressure of 500 bar by means of the time-resolved pump-probe spectroscopy. Furthermore, it has to be investigated whether an isotropically labeling results in a change of the relaxation time constant or of the underlying mechanism. The results are then classified into and discussed in the context of the results of the aqueous azide, thiocyanate and selenocyanate solutions.

The triatomic molecule carbon dioxide and its aqueous solution is quite interesting to investigate for several reasons. On one hand, the carbon dioxide is isoelectronic to the pseudohalide anions, but neutral charged and should therefore have a similar vibrational energy relaxation mechanism as the pseudohalide anions in H_2O have. On the other hand, it is well known as a gas responsible for climate change and its reduction and storage is brought into focus recently [33–37].

In several publications [38–41], the reduction and prevention of emerging carbon dioxide is discussed. An exemplaric proposal to reduce and store emitted CO_2 is the so called *Carbon Capture and Storage* (CCS) strategy [34]. Herein, the carbon dioxide is directly captured from industry, purified and compressed. For storage, different methods are considered, such as the storage of compressed CO_2 in deep geological formations [34,39] or in the deep ocean [34]. For the process of purification, the use of ionic liquids is investigated. Recently, a large number of investigations of CO_2 in different ionic liquids were published [42–48] with the aim to understand the interactions of carbon dioxide with the ionic liquids as well as to investigate the structural and rotational dynamics. The carbon dioxide in an ionic liquid is a quite challenging system due to its complex solvation structure as carbon dioxide dissolved in H_2O is, but astonishingly few information about the latter considering the vibrational energy relaxation mechanisms

can be found, except of a conference contribution of Hamm et al. [49]. Hence, in one chapter of this work, it is focused on the vibrational energy relaxation of CO_2 dissolved in H_2O under isobaric heating at a pressure of 500 bar using the carbon dioxide's asymmetric stretching vibration as a vibrational probe.

Due to the electron configuration, the carbon dioxide is isoelectronic to the pseudohalide anions N_3^-, OCN^-, SCN^- and $SeCN^-$. Therefore, it is assumed that the vibrational energy relaxation mechanism of CO_2 in H_2O should be similar to those of the aqueous pseudohalide solutions. Within the scope of this work, the time constants and the relaxation mechanism of the aqueous CO_2 and pseudohalide anion solutions are compared and discussed.

The comprehension of dynamics is not only necessary for the investigation of inter- and intramolecular interactions, but also for the chemical reactivity. The latter can be affected tremendously by the stereo-chemistry of large molecules [50, 51]. Within the scope of this work, the *trans*-4-methoxybut-3-en-2-one serves as an example to investigate the stereo-chemistry and the intramolecular interactions. Therefore, a solvent is chosen, which prevents intermolecular interactions with the solute. The *trans*-4-methoxybut-3-en-2-one finds numerous applications as a precursor to pharmacological active species [52, 53], e. g. in the synthesis of resorcinol derivatives [50], as well as to biologically or optically important molecules [54, 55]. A suitable method to investigate the conformational dynamics in solution is the so-called two-dimensional infrared spectroscopy [56–60]. It is advantageous over pump-probe spectroscopy, because it combines high temporal resolution with structural sensitivity and is therefore used within the scope of this work. As vibrational probes for the investigation of the *trans*-4-methoxybut-3-en-2-one, the strongly coupled vibrations of the C=C and C=O bonds are selected.

This thesis is divided into three chapters. The first one deals with the theoretical background relevant for this work. It is followed by a chapter, in which the experimental setup of the home-built pump-probe spectrometer is shown and explained. In the third chapter, the results of the investigation of CO_2 and OCN^- including its isotopologues in aqueous solution are discussed by means of the time-resolved pump-probe spectroscopy. Then the investigation of the *trans*-4-methoxybut-3-en-2-one in C_2Cl_4 using the two-dimensional infrared spectroscopy is presented. This work is then concluded with a summary and outlook.

Chapter 2

Theoretical background

This chapter deals with the theoretical background relevant for this work. Starting with the theory of molecular vibrations and vibrational spectroscopy, the principle of time- and frequency-resolved infrared spectroscopy is explained afterwards, while the text concentrates on the main topics. For a more-in-depth explanation, the reader is referred to relevant literature cited in the text.

2.1 Molecular vibrations

Vibrational spectroscopy treats interactions such as absorption, emission or scattering of electromagnetic radiation with molecules in the infrared spectral region [11, 12, 61]. Within the scope of this work, radiation in the range from 4 µm to 6 µm is used.

Vibrations of diatomic molecules

Vibrations can be attributed to attractive and repulsive forces, and easily described by the model of a linear harmonic oscillator (HO). In a classical treatment, the motions can be characterized by Hooke's law [11, 61, 62], whereas in a quantum mechanical treatment, the stationary Schrödinger equation needs to be solved [12]. In the latter case, energies (E_v) are obtained from the eigenvalues of the Hamiltonian according to

$$E_v = h\nu_0 \left(v + \frac{1}{2}\right), \quad v = 0, 1, 2, \ldots. \tag{2.1}$$

Here, h corresponds to Planck's constant, v to the vibrational quantum number and ν_0 to the frequency of the harmonic oscillator. The energy levels of the quantum mechanically treated harmonic oscillator are quantized regarding their energy (see figure 2.1, black), and posses equal energetic distances.

For a diatomic molecule, the corresponding frequency can be determined by means of

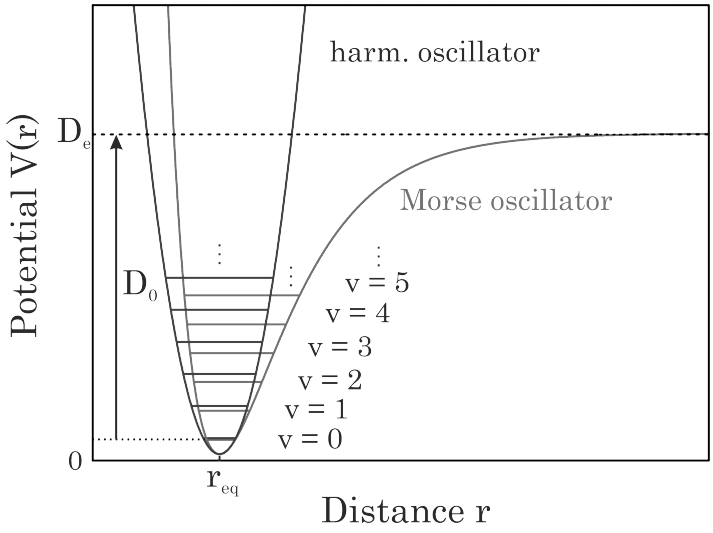

Figure 2.1: Comparison of a harmonic (black) and Morse (gray) potential at same equilibrium distances r_{eq} for their potential minima. Discrete energy levels are highlighted. Dissociation energy D_0 regarding the minimum of the corresponding potential and dissociation boundary D_e are inserted.

the reduced mass μ_{red} according to

$$\nu_0 = \frac{1}{2\pi}\sqrt{\frac{k}{\mu_{red}}} \qquad \mu_{red} = \frac{m_1 \cdot m_2}{m_1 + m_2}, \tag{2.2}$$

where m_i denotes the mass of an atom i of the molecule, and k its force constant. Based on equation (2.2), it is obvious that the larger the force constant k or the lower the reduced mass the higher the oscillator frequency is.

The model of the harmonic oscillator (HO) exhibits a big disadvantage, since it cannot describe the dissociation of bonds under formation of their fragments. For that, a suitable description was proposed by P. M. Morse [63]. He suggested a model, in which a bond between two atoms weakens with increasing energy due to a so-called anharmonicity. The corresponding potential (see figure 2.1, gray) is given by the empirical approach

$$V(r) = D_e \left[1 - e^{-\beta(r-r_{eq})}\right]^2 \qquad \beta = \nu_0 \left(\frac{2\pi^2\, c\, \mu_{red}}{D_e\, h}\right)^{1/2}, \tag{2.3}$$

where D_e corresponds to the dissociation energy of the potential, h to Planck's constant, and β to a constant depending on the frequency ν_0, the speed of light c, the reduced mass μ_{red} and D_e. The solution of the time-independent Schrödinger equation of the Morse oscillator results in a finite number of discrete energy levels, which are no longer

equidistant in spacing. The energies of this potential can be described with

$$E_v = h\,\nu_0\,\left(v+\frac{1}{2}\right) - h\,\nu_0\,x_e\left(v+\frac{1}{2}\right)^2, \tag{2.4}$$

where

$$x_e = \frac{h\,\nu_0}{4\,D_e} \tag{2.5}$$

is the anharmonic constant. The zero point energy

$$E_0 = \frac{h\,\nu_0}{2}\left(1-\frac{x_e}{2}\right) \tag{2.6}$$

deviates from that by the harmonic oscillator with the factor $(1 - x_e/2)$. The Morse potential is well suited to describe intramolecular vibrations. However, when an additional external potential perturbs these vibrations, which, for instance, is the case in liquids and solids when hydrogen bonds are attendant, a more suited potential must be used. In that case, developed by R. Schroeder and E. R. Lippincott, it considers a van-der-Waals repulsion as well as an electrostatic potential between the involved atoms X, Y forming the hydrogen bond $\mathrm{X-H--Y}$ [64–66].

Vibrations of polyatomic molecules

To specify the position of each atom of a molecule, which consists of N atoms, $3N$ coordinates are required. Translational motions of the center of mass account for three degrees of freedom, rotational motions of a nonlinear molecule as a whole for three as well. Such a system of N particles has $3N-6$ vibrational degrees of freedom. Linear molecules constitute an exception having $3N-5$ degrees of freedom, because the nuclei do not rotate about the molecular axis [67]. To describe the motions of the nuclei, a rectangular coordinate system is affixed to the equilibrium position of each nucleus. Let ξ_i be a displacement along one of the axes associated with the coordinate system of the ith nucleus

$$\xi_i = r_i - r_{i,eq}, \tag{2.7}$$

with r_i the actual position, and $r_{i,eq}$ the equilibrium position of the ith nucleus. The potential energy $V(\xi_1,\ldots,\xi_{3N})$ is then evolved as a Taylor series expansion about the

equilibrium position $\xi_i = 0$ according to [12]

$$V(\xi_1, \ldots, \xi_{3N}) = V(\xi_1 = 0, \ldots, \xi_{3N} = 0) + \sum_i \left(\frac{\partial V}{\partial \xi_i}\right)_0 \xi_i + \frac{1}{2!} \sum_{i,j} \left(\frac{\partial^2 V}{\partial \xi_i \, \partial \xi_j}\right)_0 \xi_i \, \xi_j + \ldots . \tag{2.8}$$

The sub-scripted zeros indicate that the derivatives are calculated at the equilibrium position. The first term of the Taylor series expansion corresponds to the potential energy in equilibrium, and is set equal to zero, while the first derivatives are all zero since this term is referred to when all atoms are in their equilibrium position. The second derivatives describe a matrix of generalized force constants k_{ij} [12, 62]

$$k_{ij} = \left(\frac{\partial^2 V}{\partial \xi_i \partial \xi_j}\right)_0 . \tag{2.9}$$

The potential is then given by

$$V(\xi_1, \ldots, \xi_N) = \frac{1}{2} \sum_{i,j} k_{ij} \, \xi_i \, \xi_j . \tag{2.10}$$

Investigating a diatomic molecule, and rewriting the sum with $i, j = [1, 2]$ results in

$$V(\xi_1, \xi_2) = \frac{1}{2} k_{11} \, \xi_1^2 + \frac{1}{2} k_{12} \, \xi_1 \, \xi_2 + \frac{1}{2} k_{21} \, \xi_2 \, \xi_1 + \frac{1}{2} k_{22} \, \xi_2^2 . \tag{2.11}$$

With $k = k_{11} = k_{22} = -k_{12} = -k_{21}$, the potential is

$$V(\xi_1, \xi_2) = \frac{1}{2} k (\xi_1^2 - 2\xi_1 \xi_2 + \xi_2^2) = \frac{1}{2} k (\xi_1 - \xi_2)^2 . \tag{2.12}$$

Using $\xi_1 = r_1 - r_{eq}$ and $\xi_2 = r_2 - r_{eq}$, the equation describing the potential energy of a diatomic molecule results in

$$V(\xi_1, \xi_2) = \frac{1}{2} k \left((r_1 - r_{eq}) - (r_2 - r_{eq})\right)^2 = \frac{1}{2} k \left(r_1 - r_2\right)^2 \tag{2.13}$$

corresponding to the one-dimensional potential of a harmonic oscillator.

The total energy of the investigated system is then given by the sum of the potential

(V) and the kinetic energy (T) with

$$E = T + V = \frac{1}{2}\sum_i m_i\,\dot{\xi}_i^2 + \frac{1}{2}\sum_{i,j} k_{ij}\,\xi_i\,\xi_j. \tag{2.14}$$

Investigating for example a linear molecule with B-A-B structure, the matrix of force constants K_{ij} is given in mass-weighted coordinates q_i [12]

$$K_{ij} = \begin{pmatrix} \frac{k}{m_B} & \frac{-k}{\sqrt{m_A m_B}} & 0 \\ \frac{-k}{\sqrt{m_A m_B}} & \frac{2k}{m_A} & \frac{-k}{\sqrt{m_A m_B}} \\ 0 & \frac{-k}{\sqrt{m_A m_B}} & \frac{k}{m_B} \end{pmatrix}. \tag{2.15}$$

To determine the quantum-mechanical eigen values and eigen functions, the matrix of generalized force constants has to be diagonalized by solving the following secular equation

$$\det(K_{ij} - \kappa \cdot I) = 0. \tag{2.16}$$

Here, κ corresponds to mass-weighted force constants and I to the identity matrix [12]. The corresponding eigen vectors Q_i can be attributed to normal modes of the investigated system. Using a total mass $M = m_A + 2\,m_B$ of the linear B-A-B molecule, the corresponding normal modes are described by [12]

$$\begin{aligned} Q_1 &= \frac{1}{\sqrt{M}}(m_B\,\xi_1 + m_A\,\xi_2 + m_B\,\xi_3),\ \kappa_1 = 0 \\ Q_2 &= \sqrt{\frac{m_B}{2}}(\xi_1 - \xi_3),\ \kappa_2 = \frac{k}{m_B} \\ Q_3 &= \frac{1}{\sqrt{2M}}(m_B\,\xi_1 - 2\,m_A\,\xi_2 + m_B\,\xi_3),\ \kappa_3 = \frac{k\,M}{m_A\,m_B}. \end{aligned} \tag{2.17}$$

Normal mode Q_1 describes a translation, Q_2 a symmetric stretching, and Q_3 an asymmetric stretching vibration.

So far, the displacement along one of the three axes of inertia has been presented. Investigating now a displacement along all three axes, a linear triatomic B-A-B molecule possesses $3N - 5 = 4$ normal modes. These are exemplary shown for a carbon dioxide

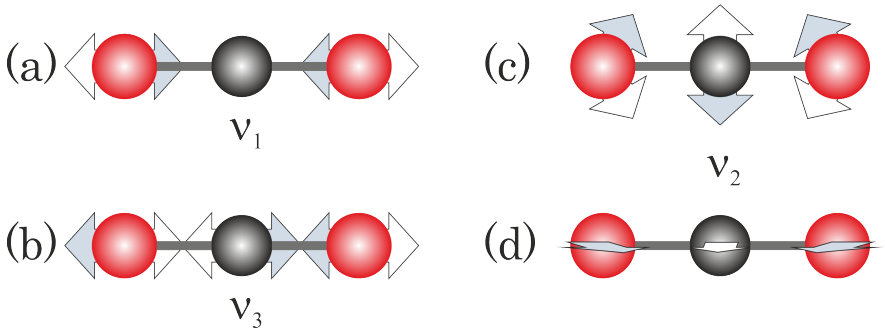

Figure 2.2: Normal modes of the linear carbon dioxide (CO_2) molecule. Arrows indicate forth (gray) and back (white) motion. In (a), the normal mode corresponds to a symmetric, in (b) to an asymmetric stretching vibration and (c)+(d) to a double degenerated bending motion.

(CO_2) molecule in figure 2.2. The normal mode displayed in figure 2.2 (a) corresponds to the symmetric stretching vibration ($\nu_1 = \nu_s$). The gray arrows indicate the forth, the white one the back motions. Figure 2.2 (b) pictures the asymmetric stretching vibration ($\nu_3 = \nu_{as}$), while (c) and (d) show the double degenerated bending vibrations ($\nu_2 = \nu_b$).

2.2 Vibrational spectroscopy

As mentioned at the beginning of this chapter, light in the infrared spectral range is able to excite molecular vibrations, but only some of them are infrared (IR)-active. A gross selection rule states that a transition from a vibrational energy level to another is allowed if the transition dipole moment ($\boldsymbol{\mu}$) changes along the vibrational coordinate [12, 62]. The transition dipole moment ($\boldsymbol{\mu}$) can be described by

$$\boldsymbol{\mu} = \sum_i \delta_i \cdot \mathbf{r}_i \tag{2.18}$$

with a partial charge δ_i of atom i and the distance $\mathbf{r}_i$ from atom i to the center of mass. In a quantum mechanical manner, the above introduced gross selection rule implies that

$$\langle \psi_m \left| \boldsymbol{\mu} \right| \psi_n \rangle \overset{!}{\neq} 0 \tag{2.19}$$

for an IR-active transition between vibrational states n and m [12]. Here, ψ_m and ψ_n describe wave functions of the involved vibrational states. The dipole operator can be

then evolved as a Taylor series expansion according to

$$\boldsymbol{\mu} = \boldsymbol{\mu}_0 + \sum_i \left(\frac{\partial \boldsymbol{\mu}}{\partial Q_i}\right)_0 Q_i + \frac{1}{2!}\sum_{i,j}\left(\frac{\partial^2 \boldsymbol{\mu}}{\partial Q_i\,\partial Q_j}\right)_0 Q_i\,Q_j + \ldots, \tag{2.20}$$

where the $Q_{i,j}$ denotes the linear combination of mass-weighted coordinates as described in section 2.1. The sub-scripted zeros indicate that the corresponding functions are determined when the system is in its equilibrium position, i. e. $Q_i = 0$. In the following, the expansion is truncated after the second term assuming that the electric transition dipole moment of a molecule is expected to vary linearly with the extension of the bond for small displacements [12]. This holds if partial charges of the involved atoms are independent of the internuclear distance. Applying then the quantum mechanical notation, eq. (2.19) results in

$$\langle \psi_m \,|\boldsymbol{\mu}|\, \psi_n \rangle = \underbrace{\boldsymbol{\mu}_0 \,\langle \psi_m | \psi_n \rangle}_{=0} + \underbrace{\sum_i \left(\frac{\partial \boldsymbol{\mu}}{\partial Q_i}\right)_0 \langle \psi_m \,|Q_i|\, \psi_n \rangle}_{=\mu_{mn}} \neq 0. \tag{2.21}$$

The first term is equal to zero due to the orthogonality of vibrational functions within the same electronic state $\langle \psi_m | \psi_n \rangle$, while the second term is abbreviated with μ_{nm}, and has to be non-zero for an IR-active vibration. In the context of the normal modes of CO_2, this means that two of the three vibrations (ν_2 or ν_b, and ν_3 or ν_{as}) are non-zero, thus, they are IR-active. The third one corresponding to the symmetric stretching vibration leads to $(\partial \boldsymbol{\mu}/\partial Q_1) = 0$, i.e. this mode is IR-inactive.

The strength of a transition can be determined by means of the transition dipole moment, more precisely the strength of a transition is proportional to the square of the absolute value of the transition dipole moment, i. e. $|\mu_{mn}|^2$.

However, it has to be distinguished between gross selection rules and specific selection rules. The former state the properties, which a molecule have to possess in order to show a particular type of transition, while the latter include statements about changes in quantum numbers occurring during transitions [12]. A specific selection rule regarding vibrational transitions of modes i, i. e. $v_i \rightarrow v_i'$, states that $v_i' = v_i \pm 1$ holds for a harmonic oscillator.

Rotational-vibrational spectroscopy

In general, the vibrational transition ($\Delta v = \pm 1$) of a molecule is accompanied by a simultaneous rotational one, where the rotational quantum number J has to change with

$\Delta J = \pm 1$ (specific selection rule for rotational transitions). The combined rotational and vibrational transitions feature a pronounced fine structure, which is presented for CO_2 in figure 2.3 (b). To understand the fine structure, it is referred to figure 2.3 (a) where an energy level scheme of a linear rotor is shown.

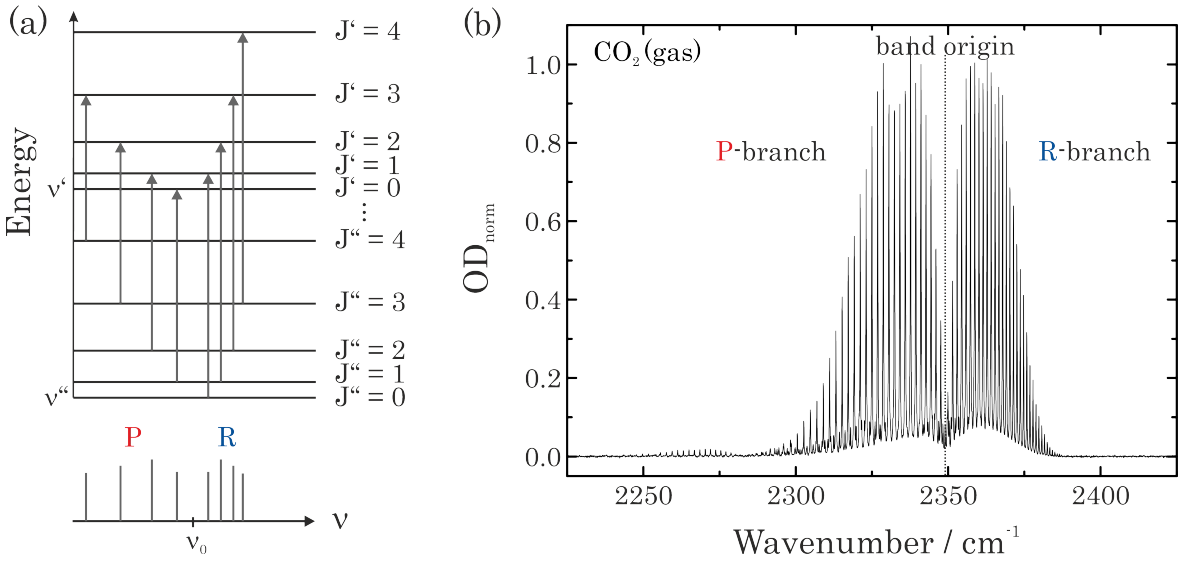

Figure 2.3: (a) Scheme of possible rotational-vibrational transitions of a linear rotator considering the specific selection rules. The lines located at the low frequency side correspond to the P-branch, those at the high frequency to the R-branch.
(b) Normalized stationary absorption spectrum of gaseous carbon dioxide. Branches and band origin are allocated.

The total energy E_{tot} of a harmonic oscillator and rigid linear rotator consists of the vibrational energy E_{vib} and the rotational energy E_{rot}

$$\begin{aligned} E_{tot}(v, J) &= E_{vib}(v) + E_{rot}(J) \\ &= h\nu_0 \left(v + \frac{1}{2}\right) + BJ(J+1). \end{aligned} \tag{2.22}$$

Here, B corresponds to the rotational constant of a molecule and ν_0 to the frequency of the harmonic oscillator. The transition frequency $\nu(v \to v + \Delta v, J \to J + \Delta J)$ is then

$$\nu(v \to v + \Delta v, J \to J + \Delta J) = \nu_0(v' - v'') + B/h\,[J'(J'+1) - J''(J''+1)] \tag{2.23}$$

with v" and J" being the rotational and vibrational quantum numbers in the lower level, while v' and J' are those of the upper level. Applying the specific selection rules

$\Delta v = +1$ and $\Delta J = +1$, equation (2.23) results in

$$\nu(v \to v+1, J \to J+1) = \nu_0 + 2\,B/h\,(J+1), \tag{2.24}$$

or respectively $\Delta v = +1$ and $\Delta J = -1$ in

$$\nu(v \to v+1, J \to J-1) = \nu_0 - 2\,B/h\,J. \tag{2.25}$$

The rotational-vibrational spectrum consists of two well separated groups of lines, the R-branch ($\Delta v = +1, \Delta J = +1$, eq. (2.24)) and the P-branch ($\Delta v = +1, \Delta J = -1$, eq. (2.25)). Due to the fact that $\Delta J = 0$ is forbidden, the pure vibrational transition cannot be observed. However, its spectral position indicates the so-called band origin. In figure 2.3 (b), a section of a gas phase spectrum of atmospheric carbon dioxide is depicted. Here, a broad absorption band with a pronounced fine structure can be observed covering the spectral range from 2270 cm^{-1} to 2400 cm^{-1}. The fine structure is well separated in two branches, red (P-branch)- and blue (R-branch)-shifted from the band origin which is located at around 2349 cm^{-1}. The frequency separations between neighboring lines change within a branch, i.e. they converge with increasing rotational quantum number J in R-branches, while they diverge in P-branches. If J is high enough, the branches may degrade and pass through a head [12, 62], after which the frequencies of the subsequent lines with increasing J approach the spectral position of the band origin again instead of moving away from it. This is due to the dependence of the rotational constant *B(v)* on the vibrational state. Using the method of combination differences, the rotational constant of the lower (B'') and upper level (B') can be determined according to

$$\tilde{\nu}_{R(J)} - \tilde{\nu}_{P(J)} = 2\,B'\,(2J+1) \tag{2.26}$$

with a common lower rotational level and

$$\tilde{\nu}_{R(J)} - \tilde{\nu}_{P(J+2)} = 2\,B''\,(2J+3) \tag{2.27}$$

with a common upper rotational level. The intensity of the lines reflects the degree of population and the degeneracy in the lower rotational level J''. The population $p_{v'',J''}$ of a certain state $|v'', J''\rangle$ can be calculated according to the Boltzmann distribution,

i.e.

$$p_{v'',J''} = \frac{(2J''+1) \cdot \mathrm{e}^{-E_{v'',J''}\,\beta}}{\sum\limits_{v'',J''} (2J''+1) \cdot \mathrm{e}^{-E_{v'',J''}\,\beta}} \tag{2.28}$$

with $\beta = 1/(k_B\,T)$.

Stationary absorption spectroscopy

In this work, stationary absorption spectra are obtained by irradiating a chemical probe with a broad-band light source. The intensity of the transmitted radiation is detected with a Fourier transform interferometer as an interferogram in the spatial domain. Its Fourier-transformation provides the spectral resolved intensity distribution $I(\nu)$. The frequency-dependent transmission $T(\nu)$ is given by

$$T(\nu) = \frac{I(\nu)}{I_0(\nu)}, \tag{2.29}$$

where $I_0(\nu)$ denotes the intensity of light before entering the sample, and $I(\nu)$ the transmitted one. The negative decadic logarithm of the transmission defines the frequency-dependent optical density $\mathrm{OD}(\nu)$ according to

$$\mathrm{OD}(\nu) = -lg(T(\nu)) = lg\left(\frac{I_0(\nu)}{I(\nu)}\right), \tag{2.30}$$

which is linked to the molar decadic extinction coefficient $\varepsilon(\nu)$, the concentration c_x of the chemical probe, and the layer thickness d of the used cell by Lambert-Beer's law

$$\mathrm{OD}(\nu) = \varepsilon(\nu) \cdot c_x \cdot d. \tag{2.31}$$

The obtained stationary spectra solely provide information on the spectral position of IR active normal modes, but no information about underlying dynamics and strengths of intermolecular interactions. These are available from time-resolved measurements which are introduced in the next section [15, 57, 68]. Ultra-short laser pulses within the femto- (fs) to picosecond (ps) regime are applied to study the vibrational energy relaxation, the spectral diffusion of vibrational resonant modes as well as reorientational dynamics between solute and solvent.

2.3 Time and frequency resolved mid-infrared spectroscopy

In general, an external electric field $E(t)$ induces a macroscopic polarization $P(t)$ in a material.

$$P(t) = P^{(1)}(t) + P^{(2)}(t) + P^{(3)}(t) + \dots$$

$$= \varepsilon_0 \cdot \left(\underbrace{\chi^{(1)} \cdot E(t)}_{\text{linear optics}} + \underbrace{\chi^{(2)} \cdot E(t) \cdot E(t) + \chi^{(3)} \cdot E(t) \cdot E(t) \cdot E(t) + \dots}_{\text{nonlinear optics}} \right) \tag{2.32}$$

with the vacuum- dielectric constant ε_0, and an electric susceptibility $\chi^{(n)}$ as a (n+1) rank tensor. It has to be discerned between linear optical processes, which can be fully characterized by first order polarization $P^{(1)}$, and nonlinear ones described by second order or higher polarizations $P^{(n)}$. Second order polarization $P^{(2)}$ describes sum- or difference-frequency mixing, which only occurs in non-centrosymmetric systems [69]. Third order polarization $P^{(3)}$ is the lowest one in fluids and gases for nonlinear optical processes. The generated time-dependent macroscopic polarization creates a signal field $E^{(3)}_{sig}$ [68], which contains information about the underlying dynamic processes. For that, at least three interactions with the external electric field are necessary. The experimental generation and detection of the signal field can be done with various techniques. Two of them are presented in the following.

Pump-probe spectroscopy

For nonlinear spectroscopy in pump-probe geometry, three IR-laser pulses in the fs- to ps-regime are required. A first pulse, the so-called pump pulse, with wave vector k_1 is used to excite the molecules under investigation, which prior are in their thermal equilibrium defined by the Boltzmann distribution (see eq. (2.28)). The pump pulses has to interact twice with the system to generate a third order signal field. This means that the wave vectors k_1 and k_2 are connected by $k_1 = k_2$ [56]. The excitation of the sample results in an altered absorption, which is interrogated by a second IR-laser pulse, the probe pulse, with wave vector k_3. This altered absorption evolves in time, and can be measured by applying a varying temporal delay between pump and probe pulses. The signal field is emitted in the direction of the probe pulse and possesses the wave vector $k_s = -k_1 + k_2 + k_3 = k_3$ [56]. Within the experiments of this work, the

detection takes place wavelength-resolved and $E_{sig}^{(3)}$ is superimposed with the electric field of the probe beam as a local oscillator for heterodyne detection [68]. In figure 2.4, the optical layout of the used pump-probe spectrometer is shown.

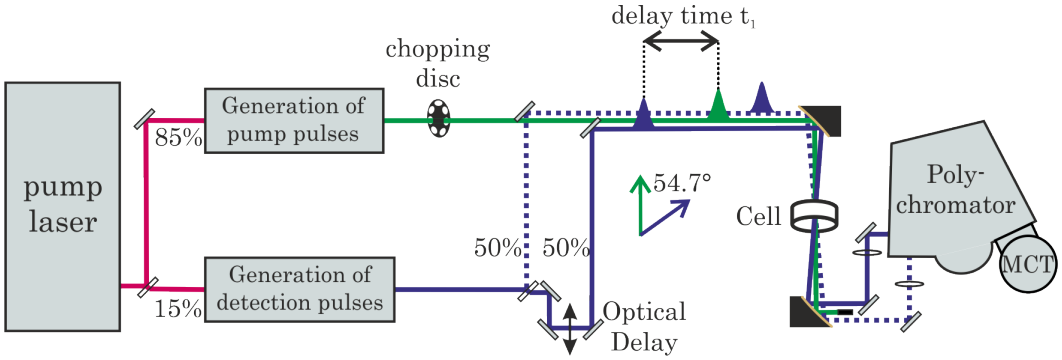

Figure 2.4: Optical layout of a pump-probe spectrometer. The red solid line corresponds to the light pulses emitted from the laser source, the green solid line represents the beam path of the pump pulses, while blue lines indicate detection pulses. The latter are divided into probe (solid line) and reference (dotted line) pulses. (MCT: MCT-array (HgCdTe))

To operate the spectrometer, the light pulses emitted from the laser source (red line) are divided with an intensity ratio of 85 % to 15 % into pump (green line) and detection (blue line) pulses. The required frequencies in the mid-IR regime are generated by second order nonlinear processes using an optical parametric amplifier with subsequent difference frequency generation [70, 71]. Afterwards, the detection pulses are divided with equal energies into probe (blue solid line) and reference pulses (blue dotted line). The reference pulses are directed into the sample cell on a beam path, which ensures that they always arrive at the cell before the pump and probe pulses do. To generate a specific temporal delay t_1 between pump and probe pulses, a computer controlled translation stage equipped with two mirrors is inserted into the optical path of the probe pulses. When pump and probe pulses pass the sample cell simultaneously, the temporal delay between both is equal to zero. The difference of the spatial delay of pump (l_{pu}) and probe (l_{pr}) pulses divided by the speed of light c determines the temporal delay t_1 according to

$$t_1 = \frac{l_{pu} - l_{pr}}{c}. \tag{2.33}$$

A spatial delay of 0.3 µm correlates to a temporal delay of roughly 1 fs.

Once the pulses have passed the sample cell, the pump pulses are blocked. The probe and the reference pulses are guided at slightly different heights through a polychromator, where they disperse similarly. Both, probe and reference pulses, are then detected separately and wavelength-dependent using a dual row MCT (HgCdTe) detector (see

figure 2.4). In this way, the optical density OD(λ) can be determined for each laser pulse according to

$$\mathrm{OD}(\lambda) = lg\left(\frac{I_{reference}(\lambda)}{I_{probe}(\lambda)}\right). \tag{2.34}$$

In general, the pump-induced changes of the absorption spectra are relatively small, i. e. $\Delta I/I_{ref,probe} << 1$ where ΔI is the pump-induced change in intensity. To separate this amount from the absorptive signal contributions, one can make use of the differential optical density ΔOD. Therefore, synchronized with the repetition rate of the laser every other second pump pulse is blocked by a chopping disc. This results in a differential optical density of the perturbed ($\mathrm{OD}_{w/pump}$) and the unperturbed system ($\mathrm{OD}_{w/o\ pump}$) according to

$$\Delta\mathrm{OD}(\lambda, t_1) = \mathrm{OD}_{w/pump}(\lambda, t_1) - \mathrm{OD}_{w/o\ pump}(\lambda). \tag{2.35}$$

The differential optical density $\Delta\mathrm{OD}(\lambda, t_1)$ contains the pure pump-induced response of the system. A generalized interpretation of the response will be discussed in the following.

As mentioned at the beginning of this chapter, the pump pulse perturbs the thermal equilibrium of the investigated sample. This is shown in a simplified scheme of a three-energy level system of an anharmonic oscillator (see figure 2.5 (a)-(c)).

At the beginning, the molecules (indicated by open circles) are located almost only in the ground state ($|0\rangle$) according to a Boltzmann distribution with $k_BT << h\nu$ under ambient conditions. The incoming pump pulse will lead to an excitation of a part of the molecules from the vibrational ground $|0\rangle$ to the first excited state $|1\rangle$ (b). The probe pulse, temporally delayed to the excitation pulse, detects the changes in absorption (c). Those are on one hand that the ground-state absorption is weakened since less molecules are available resulting in a ground-state bleach (GB). Furthermore, a stimulated emission (SE) from the first excited into the ground-state induced by the probe pulse effectively further reduces the absorption observed on $|0\rangle \rightarrow |1\rangle$ transition. On the other hand, the probe pulse can cause an excitation of molecules from the first ($|1\rangle$) to the second excited state ($|2\rangle$), which describes a transient absorption (TA). In (a)-(c), the second excited state in harmonic approximation is highlighted with a dotted line. The difference between harmonic and anharmonically lowered second excited state ($|2\rangle$) corresponds to the diagonal anharmonicity Δ. Calculating the differential optical density results in two signal contributions of the transient spectra shown in figure 2.5 (d). They are displayed as ΔmOD as a function of the frequency ν. The ground-

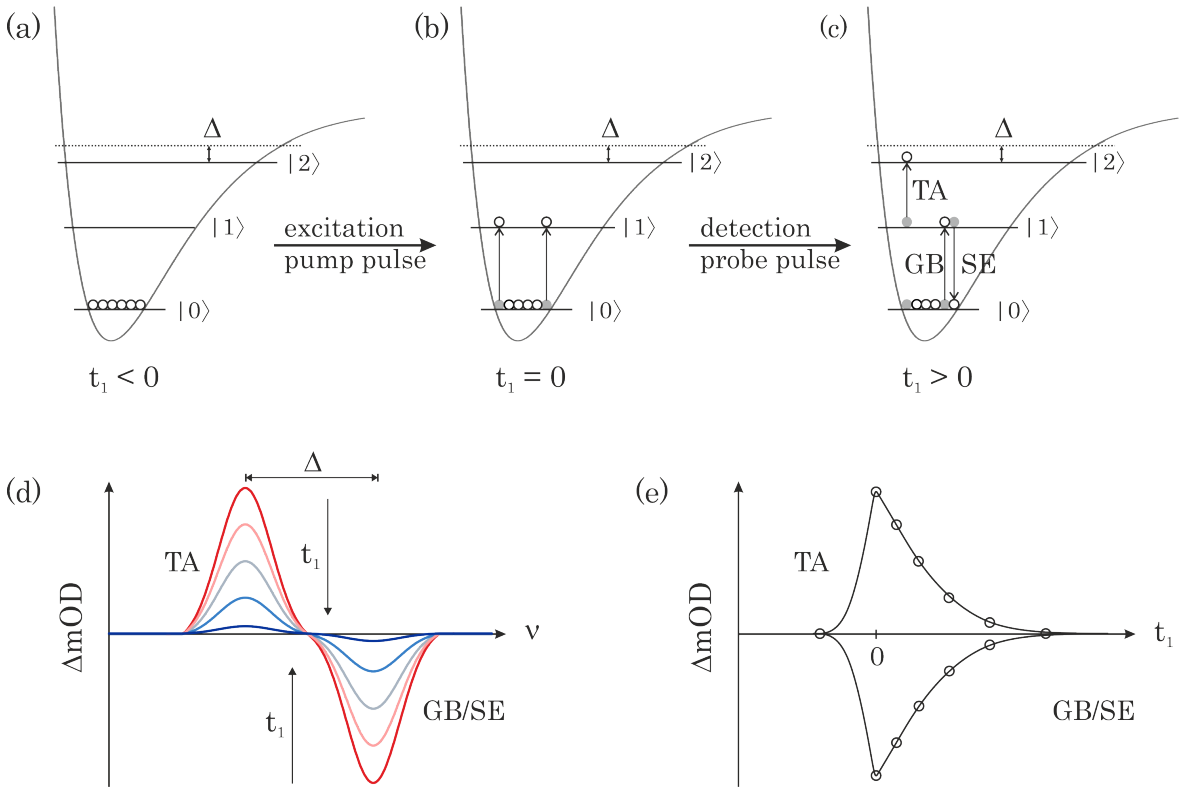

Figure 2.5: Pump-probe signal contributions.
(a)-(c) Anharmonic potential with three energy level scheme to illustrate the temporal evolution of the distribution before and after excitation. Circles display molecules.
(d) Transient spectra observed for a molecule with an anharmonic potential for different temporal delays $t_1 > 0$ (red to blue, early to late delay times).
(e) Transients (or kinetic traces) for TA and GB/SE.

state bleach as well as the stimulated emission cause a negative signal contribution emerging both at the same transition frequency, while the transient absorption creates a positive one. Due to the anharmonicity, the TA is red-shifted with respect to the GB/SE. Increasing the temporal delay (t_1) usually results in a decrease in differential optical density (ΔOD) of the transient spectra. If so, the excited population relaxes back into the ground-state. Figure 2.5 (d) shows the transient spectra for five different delay times (from red to blue, early to late delay times). A plot of the maximum of the transient absorption and the ground-state bleach / the stimulated emission as a function of the delay time t_1 can be used to determine the relaxation time. This representation is called a transient or kinetic trace (see figure 2.5 (e)). It allows an analysis of the mechanism for vibrational energy relaxation (VER).

Two-dimensional IR spectroscopy

Two-dimensional IR spectroscopy is a powerful technique to investigate intra- and intermolecular interactions. The interactions find expressions in the couplings of vibrational modes, which give rise to characteristic infrared bands. The advantage of the 2D-IR spectroscopy is its structural sensitivity and high temporal resolution [56–60]. This originates from the fact that couplings depend sensitively on the relative distances and orientations between functional groups. Furthermore, the investigation of 2D-IR line shapes provides a possibility to monitor the heterogeneity and the dynamics of the environment surrounding the oscillator [56, 60]. In general, 2D-IR spectra can be collected in either frequency-frequency, time-frequency or time-time domain [56, 72]. The former two have in common that they are realized in pump-probe geometry, in which the emitted field is detected frequency-resolved using a combination of a polychromator with an array detector (see section 2.3).

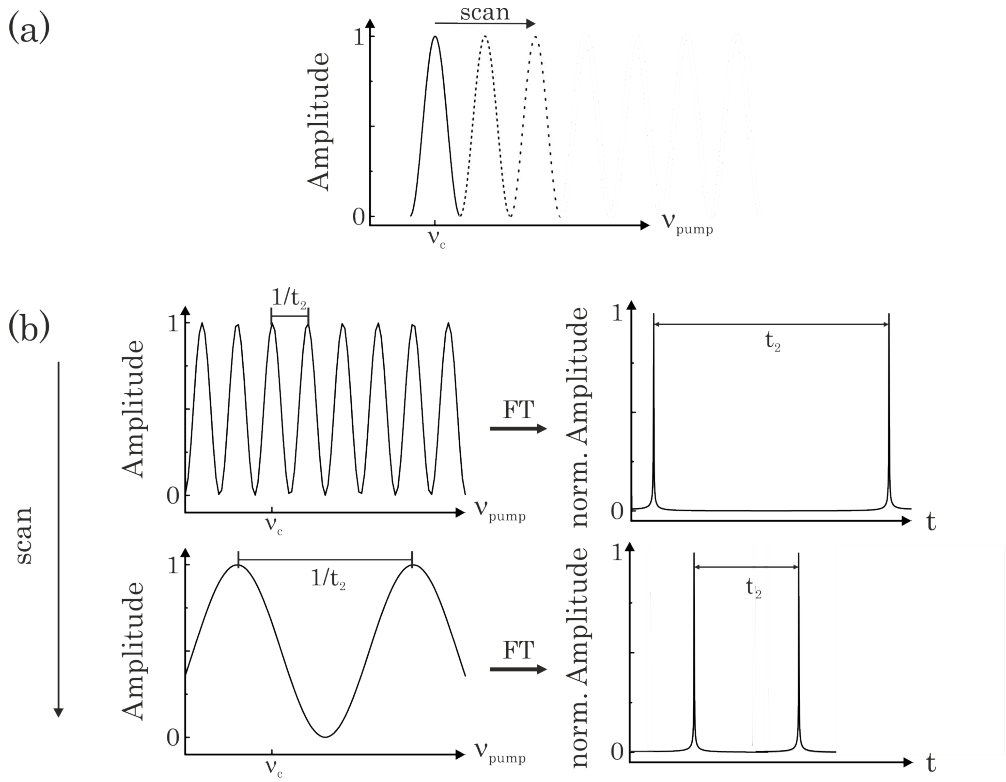

Figure 2.6: Pump pulse sequences in frequency- (a) and time-frequency domain before and after Fourier transformation (FT) (b). The center frequency of the vibrational mode of interest is indicated with ν_c and the temporal delay t_2 is a coherence time. (Based on [56], fig. 1.9)

In the frequency-frequency domain, the sample is spectral excited by a narrow-band pump pulse, which is generated either using an etalon [66, 68] or a pulse shaper [56,

73]. Recording then pump-probe spectra with such a pump pulse, and scanning its center frequency across the vibrational modes of interest (see figure 2.6 (a)), transient spectra are obtained as a function of the temporal delay t_1 (population time) for each pump frequency. Due to the additional spectral information regarding the excitation frequency, the obtained data can be presented in 2D-IR spectra or contour plots. For that, the probe frequency ν_{Probe} is displayed on the abscissa, while the pump frequency ν_{Pump} on the ordinate [56, 66, 68, 74]. The signal intensity is given with a color code at each point with coordinate (ν_{Pump},ν_{Probe}). The above described method in frequency-frequency domain is called hole-burning 2D-IR spectroscopy [16]. However, it has the disadvantage of a low frequency resolution as well as long measuring times [56, 75]. These circumstances can be overcome by recording 2D-IR spectra in the time-frequency domain. Herein, many narrow pump pulses spaced such that they span the frequency range of interest like a sinusoidal wave are used simultaneously [56]. Scanning the periodicity of the pump spectrum (see figure 2.6 (b)), each vibrational mode with center frequency ν_c will be brought in and out of resonance with the pump. To separate then the frequency components, a Fourier transformation of the measured emitted field regarding the coherence time t_2 is taken. This means that a sequence of two pump pulses, which are temporally delayed to each other, are interacting with the sample. To realize this method experimentally, either a Mach-Zehnder interferometer [72, 74, 76] or a pulse shaper [56, 73] is implemented in the pump path of the pump-probe spectrometer. This technique is called Fourier-transform 2D-IR spectroscopy in pump-probe geometry. An optical layout is shown as a scheme in figure 2.7.

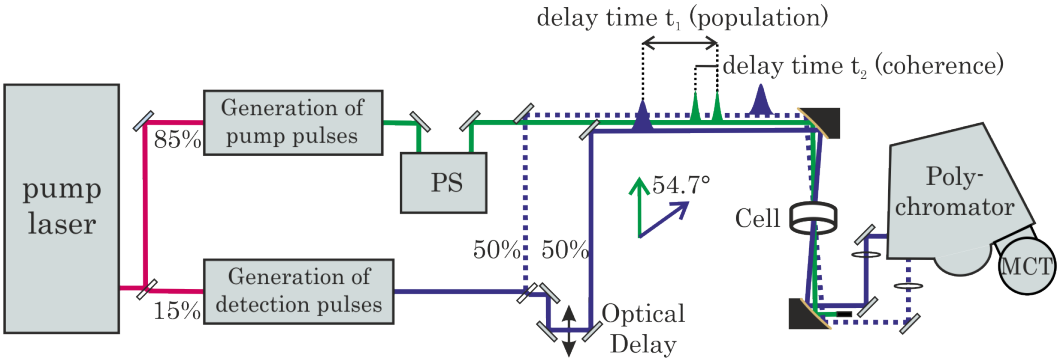

Figure 2.7: Experimental setup of a 2DIR-spectrometer in pump-probe geometry. (PS: pulse shaper, MCT: HgCdTe detector)

It is similar to the pump-probe setup in figure 2.4, but supplemented by a pulse shaping unit (PS). The advantage of a pulse shaper is that it is easy to implement in pump-probe geometry and it simultaneously produces 2D-IR spectra with high frequency and

time resolution [75, 77]. Furthermore, it can be used in both, the frequency-frequency and time-frequency domain [77].

In general, the desired signal is superimposed by scatter and transient absorption background. The former occurs, when light from one of the pump pulses is scattered from the sample into the direction of the emitted field, so that it is detected heterodyne as well. Both, scatter and transient absorption background, can be separated from the signal by phase cycling [56, 77]. It is taken advantage that the phase of the pump-induced signal in the sample depends on the difference between the phase ϕ_1 of the first and ϕ_2 of the second pump pulse, i. e. $\Delta\phi_{12} = \phi_1 - \phi_2$, while the contributions from scatter and transient absorption background are related either to ϕ_1 or ϕ_2 [56]. Using a phase cycling scheme, in which the difference between the phase of first and second pulses are $\Delta\phi_{12} = \pi$ and $\Delta\phi_{12} = 0$, the background contributions are removed by subtracting the obtained signals S, i. e. $S(\Delta\phi_{12} = \pi) - S(\Delta\phi_{12} = 0)$. More details can be found in [56, 77].

In the following, characteristic 2D-IR spectra are presented and explained. To begin with, two independent oscillators with slightly different vibrational frequencies ν_{osc1} and ν_{osc2} are considered. Their corresponding energy schemes are shown in figure 2.8 (a), whereby those are restricted to the ground state $|0\rangle$, the first $|1\rangle$ and second $|2\rangle$ excited states. It is assumed that the oscillators can be described by anharmonic potentials with energies $E(|0\rangle_i) = 0$, $E(|1\rangle_i) = h\nu_{\mathrm{osc},1}$ and $E(|2\rangle_i) = 2h\nu_{\mathrm{osc},i} - \Delta_{ii}$. As discussed in section 2.3, three transitions can occur for each oscillator, which are indicated in figure 2.8 (a) with arrows and corresponding numbers. These interactions are ground-state bleach (transitions 1 and 4), stimulated emission (transitions 2 and 6) and transient absorption (transitions 3 and 5). Figure 2.8 (b) shows the corresponding 2D-IR spectrum including the stationary absorption spectrum on top. As mentioned before, the probe frequency ν_{Probe} is displayed on the abscissa, the pump frequency ν_{Pump} on the ordinate. For the indicated diagonal, $\nu_{\mathrm{Probe}} = \nu_{\mathrm{Pump}}$ holds. In contour plots, a pump-induced reduction (increase) of the detected intensity is marked with blue (red) colors. According to this notation, in blue colored contours the sum of the GB and the SE for each oscillator is visualized as an on-diagonal peak at $\nu_{\mathrm{Probe}} = \nu_{\mathrm{Pump}} = |1\rangle_1$ for the low-frequency oscillator $|\nu_{\mathrm{osc1}}\rangle$, and $\nu_{\mathrm{Probe}} = \nu_{\mathrm{Pump}} = |1\rangle_2$ for the high-frequency one $|\nu_{\mathrm{osc2}}\rangle$. Red colored contour lines indicate the TA, which is shifted to lower frequencies compared to the GB and the SE. This is due to the anharmonicity of the potential, which can be described by the diagonal anharmonic shift Δ_{ij} with $i = j$. According to the "projection slice theorem" [56], a sum of the transient spectra of all pump frequencies is equivalent to a pump-probe spectrum recorded with a broad-band excitation at

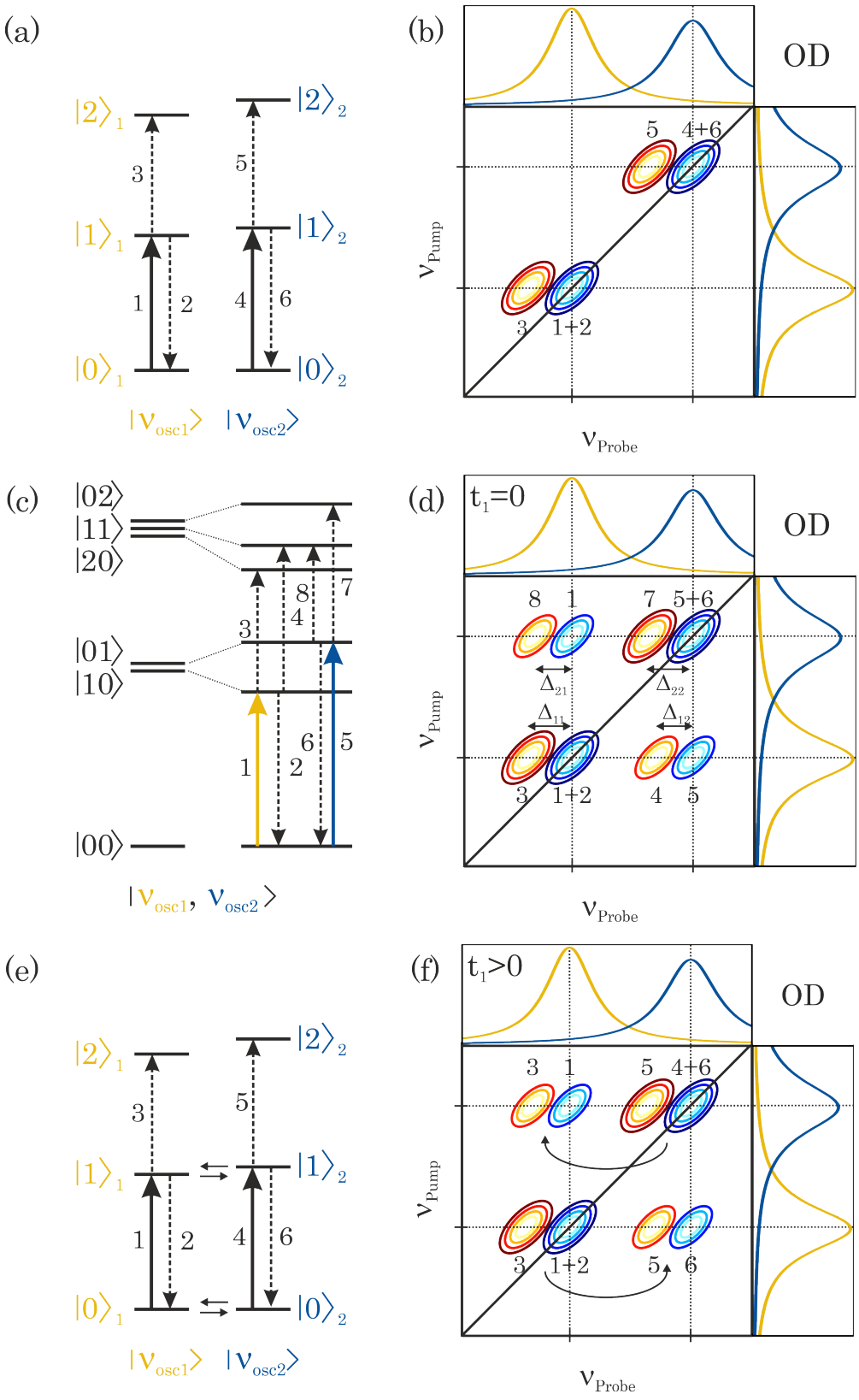

Figure 2.8: Energy-level scheme and contour plots for two uncoupled (a+b), coupled (c+d) and exchanging (e+f) oscillators.

a certain population time.

Next, two coupled oscillators $|\nu_{\mathrm{osc1}}, \nu_{\mathrm{osc2}}\rangle$ within one molecule are considered. Their energy level scheme consists of a common ground state $|00\rangle$, the first excited state of the low frequency oscillator $|10\rangle$ as well as that of the high frequency oscillator $|01\rangle$ and their second excited states $|20\rangle$ and $|02\rangle$. Furthermore, both oscillators contribute to a combination tone $|11\rangle$. The notation $|ij\rangle$ denotes a state with i quanta of excitation in the first mode and j quanta of excitation in the second mode. All mentioned states are presented in figure 2.8 (c). Here, the uncoupled mode states are shown on the left column of the level scheme describing the energies of the oscillators before coupling. On the right column those after coupling (eigenstates) are depicted. If the anharmonicity is small, i. e. $\Delta_{ij} << \nu_{\mathrm{osc},i}$, then the selection rules of harmonic oscillators approximately apply, i. e. only one oscillator can be changed by one quantum of energy at a certain time. This means that the transition $|10\rangle \rightarrow |20\rangle$ is dipole allowed, whereas $|10\rangle \rightarrow |02\rangle$ is forbidden. The 2D-IR spectrum of two coupled oscillators originates as follows. Assuming the pump frequency is scanned across the resonances of the two oscillators. Once, ν_{Pump} comes into resonance with an eigenstate, e. g. with the low frequency oscillator, the transition $|00\rangle \rightarrow |10\rangle$ (transition 1 in figure 2.8 (c, d)) will be pumped. The subsequent probe pulse gives rise to the transitions labeled 2, 3 and 4 (see figure 2.8 (c, d)). Furthermore, the probe pulse will observe a bleach of both oscillators resulting in transitions 1 and 5, since the population of the common ground state is diminished. Transitions 1 (GB), 2 (SE) and 3 (TA) are known from pump-probe spectra, transitions 4 and 5 are new and occur when the oscillators are coupled (here, with a common ground state). The latter ones arise in the off-diagonal region (figure 2.8 (d)) and are called cross peaks owning the off-diagonal anharmonicity Δ_{12}. When the pump frequency comes into resonance with the high frequency oscillator, the transition $|00\rangle \rightarrow |01\rangle$ (transition 5) will be pumped. The probe pulse leads to the transitions labeled 5 (GB), 6 (SE), 7 (TA) as well as 8 due to the transition from the state $|01\rangle$ into the combination tone $|11\rangle$, and 1, since the ground state population is diminished. Again, the on-diagonal peaks 5, 6 and 7 are known from pump-probe spectra, while transitions 1 and 8 occur as off-diagonal peaks with an off-diagonal anharmonicity Δ_{21}. The anharmonic shifts of the on-diagonal peaks are denoted Δ_{11} for the low frequency oscillator and Δ_{22} for the high frequency one. All cross peaks emerge instantaneously, i. e. they can be observed at earliest population times t_1.

The cross peaks can occur dynamically, i. e. not prompt, as illustrated in figure 2.8 (e), (f). Assuming that two conformers (*cis* and *trans*) are investigated. If one conformer, e. g. *cis*, is pumped, but converts during the population time t_1 into the *trans* conformer,

then the oscillator was initially pumped at the *cis* conformer (e.g. transition 1) but is now probed at the frequency of the *trans* conformer (transitions 4 and 6). This dynamic creates cross peaks on one side of the diagonal (transitions 5 and 6), the reverse reaction on the other side of the diagonal. This process is called chemical exchange (see figure 2.8 (e, f)). The exchange rates range from femtoseconds to the vibrational lifetime of the oscillator [56]. Inspecting a series of 2D-IR spectra for different population times, information about the exchange rates of the conformational transformations can be obtained from the relative intensities of the signal contributions [56, 78].

Line shape and broadening

In the previous section, the absorptions of coupled oscillators were discussed assuming that they can be presented as an ensemble of identical molecules. But usually, there are time-dependent variations in structure and environment of the molecules in an ensemble. Descriptive examples are hydrogen bonds, for instance between dissolved carbon dioxide and H_2O or cyanate anions and H_2O. Each solute molecule will sit in a different hydrogen bonded environment, which influences its potential. This leads to a redshift of the vibrational frequency of the solute molecules in solution compared to the situation in gas phase. Furthermore, the hydrogen bonds create a network which is rather dynamically than rigid. At each instant of time, each solvent molecule will have a different vibrational frequency so that all molecules together create a distribution of frequencies [56]. This distribution is inhomogeneous if probed transitions frequencies of the solvent molecules do not change on the time scale of the pulse sequence. In general, each molecule possesses an intrinsic line width that cannot be narrower than dictated by its vibrational lifetime. This is due to the uncertainty of energy of an excited state with finite lifetime [56], which is described by Heisenberg's uncertainty principle. The intrinsic line width is attributed to the line width broadening mechanism and is often called homogenous line width [56, 79].

To study an inhomogeneous broadening of vibrational lifetimes, the Kubo-Anderson general stochastic theory [80, 81] of line shape can be applied and will be discussed in the following.

The theory was originally formulated by Kubo and Anderson to describe the shape or profile of spectral lines and to study interactions and motions of physical systems by means of nuclear magnetic resonance (NMR) spectroscopy [80, 81]. However, it has also been proven adequate for characterization of spectral line widths of vibrational transitions [56, 82]. Firstly, it is supposed that an oscillator with center frequency ν_0 is

randomly perturbed. Its proper frequency ν is modulated in time in a random fashion according to

$$\nu(t) = \nu_0 + \nu_1(t). \tag{2.36}$$

Here, ν_0 is time-independent, and $\nu_1(t)$ can be described by a stochastic process [83]. The equation of motion of the oscillator is

$$\frac{\mathrm{d}x}{\mathrm{d}t} = \mathrm{i}\ \nu(t)\ x(t), \tag{2.37}$$

where the real part of x is the coordinate of the oscillator and the imaginary part the momentum [83]. Solving the differential equation with an initial value x_0 results in

$$x(t) = x_0\ \exp\left[\mathrm{i}\int_0^t \nu(t')\mathrm{d}t'\right]. \tag{2.38}$$

The corresponding time correlation function is

$$\langle x^*(0)\ x(t)\rangle = \left\langle x_0^*\ x_0\ \exp\left[\mathrm{i}\int_0^t v(t')\mathrm{d}t'\right]\right\rangle. \tag{2.39}$$

If x_0 is independent of $\nu(t)$, the correlation function simplifies to

$$\langle x^*(0)\ x(t)\rangle = \mathrm{e}^{\mathrm{i}\nu_0 t}\ \phi(t) \tag{2.40}$$

with

$$\phi(t) = \left\langle \exp\left(\mathrm{i}\int_0^t \nu_1(t')\mathrm{d}t'\right)\right\rangle. \tag{2.41}$$

The power spectrum is then obtained from the Wiener-Khintchine theorem [82]

$$I(\nu') = \frac{1}{2\pi}\int_{-\infty}^{\infty} \phi(t)\ \mathrm{e}^{-\mathrm{i}\nu' t}\mathrm{d}t, \tag{2.42}$$

where $\nu' = \nu - \nu_c$ describes the difference of the actual frequency ν from the center frequency ν_c.

Secondly, it is supposed that the stochastic process described by $\nu_1(t)$ is stationary,

i. e.

$$\langle \nu_1(t) \rangle = 0. \tag{2.43}$$

Its correlation function is then given to be equal to

$$\langle \nu_1(t_0)\ \nu_1(t_0+t) \rangle = \left\langle \nu_1^2 \right\rangle \psi(t), \tag{2.44}$$

where $\langle \nu_1^2 \rangle$ and the function $\psi(t)$ characterize the physics of the random frequency modulations and are assumed to be known [82].

Using equation (2.44), equation (2.41) results in

$$\phi(t) = \exp\left[- \left\langle \nu_1^2 \right\rangle \int_0^t (t-\tau)\psi(\tau)\mathrm{d}\tau \right]. \tag{2.45}$$

The corresponding power spectrum is

$$I(\nu) = \frac{1}{2} \int_{-\infty}^{\infty} \mathrm{d}t\ \exp\left[-\mathrm{i}\nu t - \Delta^2 \int_0^t (t-\tau)\psi(\tau)\mathrm{d}\tau \right], \tag{2.46}$$

where $\Delta^2 = \langle \nu_1^2 \rangle$, describes a measure of the magnitude of the random frequency modulation. Furthermore,

$$\tau_c = \int_0^{\infty} \psi(\tau)\mathrm{d}\tau = \frac{1}{\langle \nu_1^2 \rangle} \int_0^{\infty} \langle \nu_1(t_0)\ \nu_1(t_0+t) \rangle\, \mathrm{d}t \tag{2.47}$$

characterizes the correlation time of this modulation [83].

Thirdly, if the correlation function of $\nu_1(t)$ decays in a single exponential fashion, i. e.

$$\psi(t) = \exp\left(-t/\tau_c\right), \tag{2.48}$$

then equation (2.45) becomes

$$\phi(t) = \exp\left[-\Delta^2 \tau_c \left(t - \tau_c\ \left(1 - \mathrm{e}^{-t/\tau_c} \right) \right) \right] = \exp\left[-\alpha^2 \left(\frac{t}{\tau_c} - 1 + \mathrm{e}^{-t/\tau_c} \right) \right] \tag{2.49}$$

with [83]

$$\alpha = \Delta\ \cdot\ \tau_c\ . \tag{2.50}$$

Considering now two limits of α.

(1) $\alpha \to \infty$ and $\tau_c \to \infty$: Then $\phi(t)$ vanishes unless t is very small. Thus, eq. (2.49) is approximated by

$$\phi(t) = \exp\left(-\frac{\Delta^2}{2}t^2\right). \tag{2.51}$$

The power spectrum results in

$$I(\nu) = \frac{1}{\sqrt{2\pi}\Delta}\exp\left(-\frac{\nu^2}{2\Delta^2}\right), \tag{2.52}$$

and is described by a Gaussian function [83].

(2) $\alpha \to 0$: The spectrum becomes narrower, a phenomenon called motional narrowing [83].

In the following, it is assumed that the correlation function of the frequency modulation decays single exponentially (eq. (2.48)) within the correlation time τ_c according to equation (2.47). In a short time approximation, where $t << \tau_c$ holds, the correlation function remains undamped, thus $\psi(t) \approx \text{const} = 1$ [83], and

$$\phi(t) = \exp\left(-\frac{1}{2}\Delta^2\, t^2\right) \tag{2.53}$$

describes the average over all possible distributions of the modulation ν_1. Each oscillator has coherent motion during this short time, thus, the dynamical coherence is dominant [83]. For long times $t >> \tau_c$, one obtains [83]

$$\phi(t) = \exp\left(-\gamma(t) + \delta\right), \tag{2.54}$$

with

$$\gamma = \Delta^2\tau_c = \Delta\ \alpha, \quad \delta = \Delta^2 \int_0^\infty \tau\ \psi(\tau)\mathrm{d}\tau, \tag{2.55}$$

as long time approximation of the correlation functions, and the corresponding spectrum is Lorentzian [83]

$$I(\nu) = \frac{\mathrm{e}^\delta}{\pi}\frac{\gamma}{\nu^2 + \gamma^2} \tag{2.56}$$

and with consideration of the center frequency ν_c

$$I(\nu) \propto \frac{1}{\pi} \frac{\gamma}{(\nu - \nu_c)^2 + \gamma^2}. \tag{2.57}$$

To conclude, if $\alpha > 1$, and thus, $t << \tau_c$ the short time approximation is suitable. The spectrum can be described by a Gaussian (eq. (2.52)). If $\alpha < 1$ and $t >> \tau_c$, the long time approximation is valid and the corresponding spectrum is Lorentzian [83]. Transitions between the conditions $\alpha > 1$ and $\alpha < 1$, i. e. $\alpha \approx 1$, show a Lorentzian shape at the center, while the wings are close to a Gaussian one.

2.4 Fermi's golden rule

In this section, a derivation of Fermi's golden rule is given [12,82,84–86]. It describes a transition rate from a perturbed discrete initial state $|i\rangle$ to a final one $|f\rangle$. The latter is nestled into a continuum of bath states with which the discrete initial state can couple. A scheme of the described system is shown in figure 2.9.

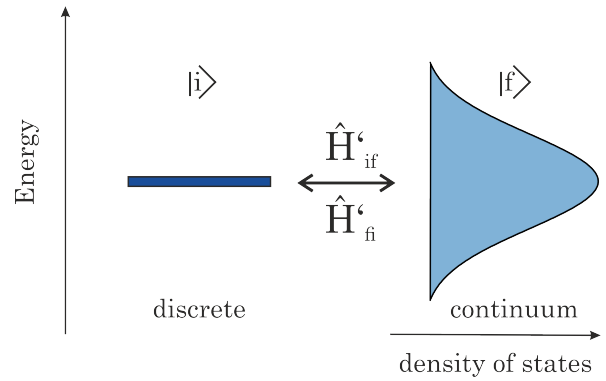

Figure 2.9: Scheme of a quantum mechanical system underlying Fermi's golden rule. An oscillator at an initial, discrete state $|i\rangle$ interacts with a continuum of final bath states $|f\rangle$.

The presented quantum mechanical system can be described with time-dependent perturbation theory. Here, the time-dependent Schrödinger equation for a system described with Hamiltonian $\mathbf{H}$

$$\mathbf{H}\psi = \mathrm{i}\hbar \frac{\partial}{\partial t}\psi, \tag{2.58}$$

is applied. $\hbar$ denotes the reduced Planck constant and ψ a wave function. $\mathbf{H}$ is separated according to

$$\mathbf{H} = \mathbf{H}_0 + \mathbf{H}'(t), \tag{2.59}$$

where $\mathbf{H}_0$ is the time-independent Hamiltonian for which the eigenfunctions $|n\rangle$ are known and $\mathbf{H}'$(t) the time-dependent perturbation. Assuming an orthonormal basis with eigenfunctions $|i\rangle$ and $|f\rangle$ with $f = 2, 3, 4, ...$ for an unperturbed case leads to

$$\mathbf{H}_0 = E_i \left|i\right\rangle \left\langle i\right| + \sum_{f=2}^{\infty} E_f \left|f\right\rangle \left\langle f\right| . \tag{2.60}$$

For the perturbation term $\mathbf{H}'(t)$, it is assumed that it allows coupling between state $|i\rangle$ and the manifold $|f\rangle$ only, i. e. $\mathbf{H}'_{f,f} = 0$, $\mathbf{H}'_{i,f} = \mathbf{H}'_{f,i} \neq 0$ for all f. Then it can be written

$$\mathbf{H}'(t) = \sum_{f=2}^{\infty} \mathbf{H}'_{i,f}(t) \left|i\right\rangle \left\langle f\right| + \mathbf{H}'_{f,i}(t) \left|f\right\rangle \left\langle i\right| . \tag{2.61}$$

The waveform solving the time-dependent Schrödinger equation can be written as a linear combination of eigenfunctions of the unperturbed system with time-dependent factor $C_i(t)$ and $C_f(t)$ [82]

$$\psi(t) = C_i(t) \left|i\right\rangle + \sum_{f=2}^{\infty} C_f(t) \left|f\right\rangle . \tag{2.62}$$

The aim is now to determine the transition rate for a case, in which the system is in state $|i\rangle$ at $t = 0$. Thus, the boundary conditions

$$C_i(t = 0) = 1, C_f(t = 0) = 0 \tag{2.63}$$

are used. The transition rate of the perturbed initial state to a final one is the temporal evolution of $|C_i(t)|^2$. It describes the probability of finding the system in state $|i\rangle$ at time t [82].

Substituting eq. (2.62) into eq. (2.58) and multiplying with $|i\rangle$ or respectively $|f\rangle$ leads to

$$\begin{aligned} \hbar \frac{\mathrm{d}}{\mathrm{d}t} C_i &= -\,\mathrm{i} E_i C_i - \mathrm{i} \sum_{f=2}^{\infty} \mathbf{H}'_{i,f} C_f \\ \hbar \frac{\mathrm{d}}{\mathrm{d}t} C_f &= -\,\mathrm{i} E_f C_f - \mathrm{i} \sum_{f=2}^{\infty} \mathbf{H}'_{f,i} C_i . \end{aligned} \tag{2.64}$$

Assuming, that the manifold f constitutes of a continuum of states, then the summation over f discrete quantum number converts into an integral over the energy of the

continuum. Considering Green's function [82], the temporal evolution of $C(t)$ results in

$$C_i(t) = C_i(0) \exp\left(-\frac{\mathrm{i}E_i t}{\hbar} - \frac{1}{2}\frac{\Gamma t}{\hbar}\right) \tag{2.65}$$

and

$$|C_i(t)|^2 = \exp\left(-\frac{\Gamma t}{\hbar}\right). \tag{2.66}$$

The transition probability is then described with the rate constant $\Gamma/\hbar$ with

$$\Gamma = 2\pi \left|\mathbf{H}'_{i,f}\right|^2 \rho_f(E_f), \tag{2.67}$$

where ρ_f denotes the density of states in the f manifold. As mentioned earlier, $\left|\mathbf{H}'_{i,f}\right|^2$ denotes the coupling term or interaction matrix element [85]. Summarized, the initially excited state $|i\rangle$ decays mono-exponentially with a rate constant

$$k = \frac{\Gamma}{\hbar} = \frac{2\pi}{\hbar} \left|\mathbf{H}'_{i,f}\right|^2 \rho_f(E_f). \tag{2.68}$$

This equation is used to describe intra- and intermolecular relaxation processes.

Spectral overlap

In the previous section (2.4), Fermi's golden rule was derived. Therefore, a system consisting of an isolated discrete initial state $|i\rangle$ and a final one $|f\rangle$ nestled into a continuum of bath states was assumed. Within the scope of this work, Fermi's golden rule is applied to systems consisting of a solute and a solvent investigated at different temperatures by means of time-resolved pump-probe and stationary absorption spectroscopy. The initially excited solute state corresponds to the discrete initial state $|i\rangle$, which couples to a spectral broad solvent's mode consisting of a continuum of bath states.

To apply Fermi's golden rule, it is necessary to receive experimental data for the density of states $\rho_f(E_f)$. However, it cannot be measured directly. An estimation can be done based on the proportionality of the density of energy-accepting states to the molar decadic extinction coefficient $\varepsilon_{solv}(\nu)$ of the solvent [28]. The proportional factor depends then on the strength of the corresponding transition and thus, on the square of the absolute value of the transition dipole moment $|\mu|^2$ [12] (see section 2.2). If

the initial state $|i\rangle$ is energetically infinitesimal small, the proportionality between the density of states and the molar decadic extinction coefficient still holds. But in real systems, the initial state $|i\rangle$ possesses a finite band width (see section 2.3), so that an overlap integral between both states $|i\rangle$ and $|f\rangle$ at various temperatures T

$$\rho(T) \propto \int_0^\infty \varepsilon_{solv}(\nu, T) \cdot \varepsilon_{solu}(\nu, T)\, \mathrm{d}\nu \tag{2.69}$$

has to be calculated [28]. Here, ν denotes the frequency and $\varepsilon_{solu}(\nu, T)$ the temperature-dependent molar decadic extinction coefficient of the solute. Since the solubility of the solute in the solvent varies with temperature, the area under the extinction curve of the solute is used to normalize the overlap integral in equation (2.69) according to

$$\rho(T) \propto S(T) = \frac{\int_0^\infty \varepsilon_{solv}(\nu, T) \cdot \varepsilon_{solu}(\nu, t)\, \mathrm{d}\nu}{\int_0^\infty \varepsilon_{solu}(\nu, T)\, \mathrm{d}\nu}, \tag{2.70}$$

where *S(T)* denotes the normalized spectral overlap integral. Consequently, equation (2.68) can be rewritten as

$$k \propto \frac{2\pi}{\hbar} \left|\mathbf{H}'_{i,f}\right|^2 S(T). \tag{2.71}$$

2.5 Theory of a resonance energy transfer

The theory of a resonance energy transfer, also known as the Förster theory, deals with an intra- or resonant intermolecular energy transfer from an energy donor (D) to an energy acceptor (A). In general, the derivation of this theory is similar to that of Fermi's golden rule given previously. The Förster theory is based on the Hamiltonian of a system $\mathbf{H}$, which consists of an Hamiltonian of a donor $\mathbf{H}_D$, that of an acceptor $\mathbf{H}_A$ and that of an interaction of donor and acceptor $\mathbf{H}_{DA}$

$$\mathbf{H} = \mathbf{H}_D + \mathbf{H}_A + \mathbf{H}_{DA}. \tag{2.72}$$

Under the assumption that the Born-Oppenheimer approximation holds, the nuclei of both the energy donor and the energy acceptor will not move significantly during the energy transfer. Thus, the Hamiltonian of the system is described with the electronic Hamiltonian of the energy donor, acceptor and of the interaction Hamiltonian [87]. The latter ($\mathbf{H}^{el}_{DA}$) is approximated by splitting the intermolecular electronic interac-

tions in monopole-monopole, monopole-dipole and dipole-dipole interactions and thus depends on the distance of the energy donor to the energy acceptor. The interaction Hamiltonian can be approximated by the potential, which is

$$V = \sum_i \frac{q_i}{|\mathbf{R}_i|}. \tag{2.73}$$

Here, q_i represents the charges separated by a fixed distance $\mathbf{R}_i$, expressed by the coordinates x_i, y_i and z_i. The contributions from q_i to the potential can be expanded in a Taylor series in $|\mathbf{R}_i|$ as

$$\begin{aligned} V(\mathbf{R}) = &\sum_i q_i \ |\mathbf{R}_i|^{-1} + \sum_i q_i \left(x_i \frac{\partial(|\mathbf{R}_i|^{-1})}{\partial x_i} + y_i \frac{\partial(|\mathbf{R}_i|^{-1})}{\partial y_i} + z_i \frac{\partial(|\mathbf{R}_i|^{-1})}{\partial z_i} \right) \\ &+ \frac{1}{2} \sum_i q_i \Bigg(x_i x_i \frac{\partial^2(|\mathbf{R}_i|^{-1})}{\partial x_i^2} + x_i y_i \frac{\partial^2(|\mathbf{R}_i|^{-1})}{\partial x_i \partial y_i} + x_i z_i \frac{\partial^2(|\mathbf{R}_i|^{-1})}{\partial x_i \partial z_i} \\ &+ x_i y_i \frac{\partial^2(|\mathbf{R}_i|^{-1})}{\partial y_i \partial x_i} + y_i y_i \frac{\partial^2(|\mathbf{R}_i|^{-1})}{\partial y_i^2} + y_i z_i \frac{\partial^2(|\mathbf{R}_i|^{-1})}{\partial y_i \partial z_i} \\ &+ x_i z_i \frac{\partial^2(|\mathbf{R}_i|^{-1})}{\partial z_i \partial x_i} + y_i z_i \frac{\partial^2(|\mathbf{R}_i|^{-1})}{\partial z_i \partial y_i} + z_i z_i \frac{\partial^2(|\mathbf{R}_i|^{-1})}{\partial z_i^2} \Bigg). \end{aligned} \tag{2.74}$$

The first sum is the monopole potential if all the charges are located exactly at the origin. The second sum describes the dipole interactions, while the third one involves the nine components of the quadrupole distribution [87]. If the molecules have no net charges, the main contributions of $\mathbf{H}^{el}$ usually come from dipole-dipole interactions [82, 87]. The derivatives of $|\mathbf{R}_i|^{-1}$ with respect to x_i, y_i and z_i can be written as derivatives with respect to the coordinates of a point

$$\frac{\partial(|\mathbf{R}_i|^{-1})}{\partial x_i} = -\frac{\partial(|\mathbf{R}_i|^{-1})}{\partial x} \frac{x}{|\mathbf{R}_i|^3}. \tag{2.75}$$

With this, the dipole potential results in

$$V(\mathbf{R}) = \frac{1}{|\mathbf{R}|^3} \sum_i (q_i \ x_i \ x_i + q_i \ y_i \ y_i + q_i \ z_i \ z_i) = \frac{\boldsymbol{\mu}_i \ \mathbf{R}_i}{|\mathbf{R}|^3}. \tag{2.76}$$

The field $\mathbf{E}$ at $\mathbf{R}$ is then

$$\mathbf{E}(\mathbf{R}) = -\nabla V(\mathbf{R}) = -\nabla\left(\frac{\boldsymbol{\mu}\,\mathbf{R}}{|\mathbf{R}|^3}\right) = -\boldsymbol{\mu}\,|\mathbf{R}|^{-3} \;-\; (\boldsymbol{\mu}\mathbf{R})\nabla(|\mathbf{R}|^{-3}) \tag{2.77}$$

$$= -\boldsymbol{\mu}\,|\mathbf{R}|^{-3} + 3\,\boldsymbol{\mu}\mathbf{R}^2\,|\mathbf{R}|^{-5}\,.$$

The interaction matrix element $\mathbf{H}^{el}_{DA}$ can be approximated by the field of the dipole potential at distance $\mathbf{R}_{DA}$

$$\mathbf{H}^{el}_{DA} \approx \left(\frac{3n}{2n^2+1}\right)^2 \left\{(\boldsymbol{\mu}_A\,\boldsymbol{\mu}_D)\;|\mathbf{R}_{DA}|^{-3} \;-3\;(\boldsymbol{\mu}_A\,\mathbf{R}_{DA})\;(\boldsymbol{\mu}_D\,\mathbf{R}_{DA})\,|\mathbf{R}_{DA}|^{-5}\right\}. \tag{2.78}$$

The factor $(3n/(2n^2+1))^2$ represents a dielectric screening in a medium with the refractive index n, $\boldsymbol{\mu}_i$ is the dipole vector for electrons of the functional group i and $\mathbf{R}_{DA}$ the vector from the center of a functional group A to the center of a functional group D within a molecule (see figure 2.10). Vectors $\boldsymbol{\mu}_A$, $\boldsymbol{\mu}_D$ and the distance vector $\mathbf{R}_{DA}$ are illustrated in figure 2.10.

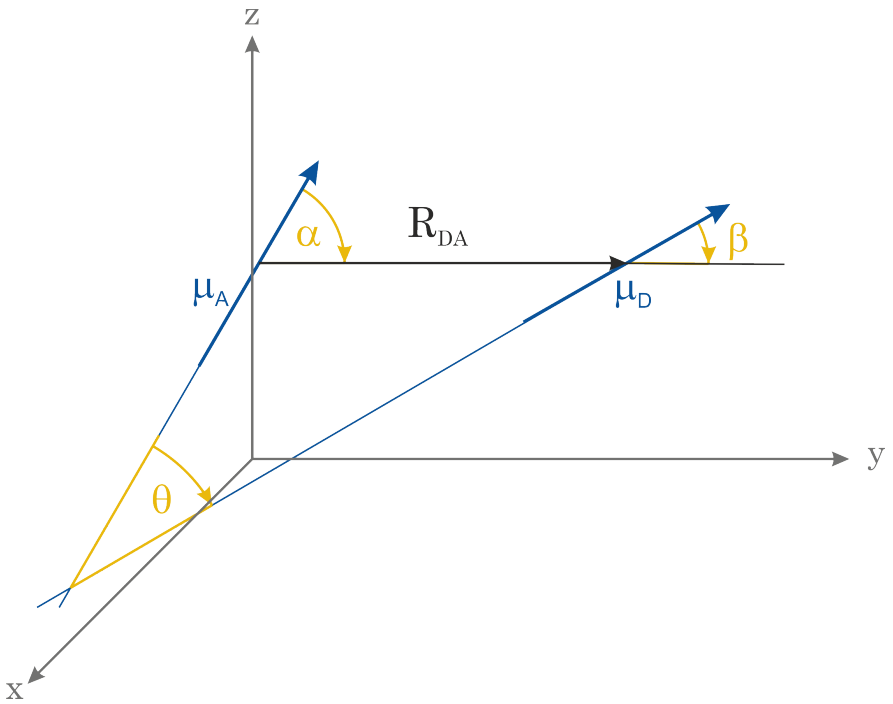

Figure 2.10: Scheme of dipole moments $\boldsymbol{\mu}_i$ of two functional groups within a molecule. The distance between the center of the first and that of the second dipole moment is given by the vector $\mathbf{R}_{DA}$ (black). Three angles (α, β, θ) (yellow) describe the orientation of both dipole moments and are shown within the scheme.

The angles α, β and θ describe the orientation of the dipole moments and are used in

the calculation of the scalar products of $\boldsymbol{\mu}_A\boldsymbol{\mu}_D$, $\boldsymbol{\mu}_A\mathbf{R}_{DA}$ and $\boldsymbol{\mu}_D\mathbf{R}_{DA}$ as

$$\begin{aligned}\boldsymbol{\mu}_A \cdot \boldsymbol{\mu}_D &= |\boldsymbol{\mu}_A|\ |\boldsymbol{\mu}_D|\ cos(\theta)\\ \boldsymbol{\mu}_A \cdot \mathbf{R}_{DA} &= |\boldsymbol{\mu}_A|\ |\mathbf{R}_{DA}|\ cos(\alpha)\\ \boldsymbol{\mu}_D \cdot \mathbf{R}_{DA} &= |\boldsymbol{\mu}_D|\ |\mathbf{R}_{DA}|\ cos(\beta).\end{aligned} \tag{2.79}$$

Equation (2.78) is then

$$\begin{aligned}\mathbf{H}^{el}_{DA} &= \left(\frac{3n}{2n^2+1}\right)^2 \left(\frac{|\boldsymbol{\mu}_A|\ |\boldsymbol{\mu}_D|\cos(\theta)}{|\mathbf{R}_{DA}|^3} - \frac{3\ (|\boldsymbol{\mu}_A|\,|\mathbf{R}_{DA}|\cos(\alpha))\,(|\boldsymbol{\mu}_D|\,|\mathbf{R}_{DA}|\cos(\beta))}{|\mathbf{R}_{DA}|^5}\right)\\ &= \left(\frac{3n}{2n^2+1}\right)^2 \left(\frac{\sqrt{D_A}\sqrt{D_D}\cos(\theta)}{|\mathbf{R}_{DA}|^3} - \frac{3\left(\sqrt{D_A}\cos(\alpha)\sqrt{D_D}\cos(\beta)\right)}{|\mathbf{R}_{DA}|^3}\right)\\ &= \left(\frac{3n}{2n^2+1}\right)^2 \left(\frac{\sqrt{D_A}\sqrt{D_D}\ (\cos(\theta) - 3\ \cos(\alpha)\cos(\beta))}{|\mathbf{R}_{DA}|^3}\right).\end{aligned} \tag{2.80}$$

Here, $\sqrt{D_{DA(i)}}$ is the magnitude of $\boldsymbol{\mu}_i$ and describes the dipole strength. Eq. (2.80) can be also written as

$$\mathbf{H}^{el}_{DA} = \left(\frac{3n}{2n^2+1}\right)^2 \left(\sqrt{D_{DA(A)}}\sqrt{D_{DA(D)}}\ \kappa\ |\mathbf{R}_{DA}|^{-3}\right) \tag{2.81}$$

with an orientation factor $\kappa = \cos(\theta) - 3\cos(\alpha)\cos(\beta)$.

Chapter 3

Experimental setup

This chapter will serve as a presentation of the extension of the home-built pump-probe spectrometer to one for also recording two-dimensional infrared (2D-IR) spectra. For that purpose, the operation principle of the implemented pulse shaper is explained, and its specifications are discussed. Furthermore, the upgrades of the existing high-temperature high-pressure equipment as well as the sample preparation are presented. In the last section, the post-processing of experimental data is explained, which was used for the analysis of the data recorded within the scope of this work.

3.1 Time-resolved mid-infrared spectroscopy

The spectrometer, introduced in this section, consists of two independently tunable mid-IR light sources delivering ultra-short pulses, a pulse shaper and a home-built pump-probe experiment with a polychromator for detection of the emitted radiation. It is suitable for performing pump-probe experiments as well as for recording 2D-IR spectra and was implemented together with Jörg Lindner based on earlier setups in the Vöhringer group [66, 74].

Optical beam path

A scheme of the optical setup is shown in figure 3.1 and will be discussed in detail in the following. The abbreviations and technical details are given in parenthesis (abbreviation; company, product name or specifications) within the text.

A commercially available Titan-Sapphire (Ti:Sa) laser (Spectra Physics, Solstice Ace) with an output power of 6 W is used to operate three different experimental setups. The one, described and used within this work, receives about one third of the available power, i. e. 2.1 W. The outgoing laser light has a wavelength of 800 nm and a pulse duration of around 50 fs at a repetition rate of 1 kHz. The primary power of 2.1 W is divided using a dielectric coated beam splitter with a reflectance of 85 %. The reflected

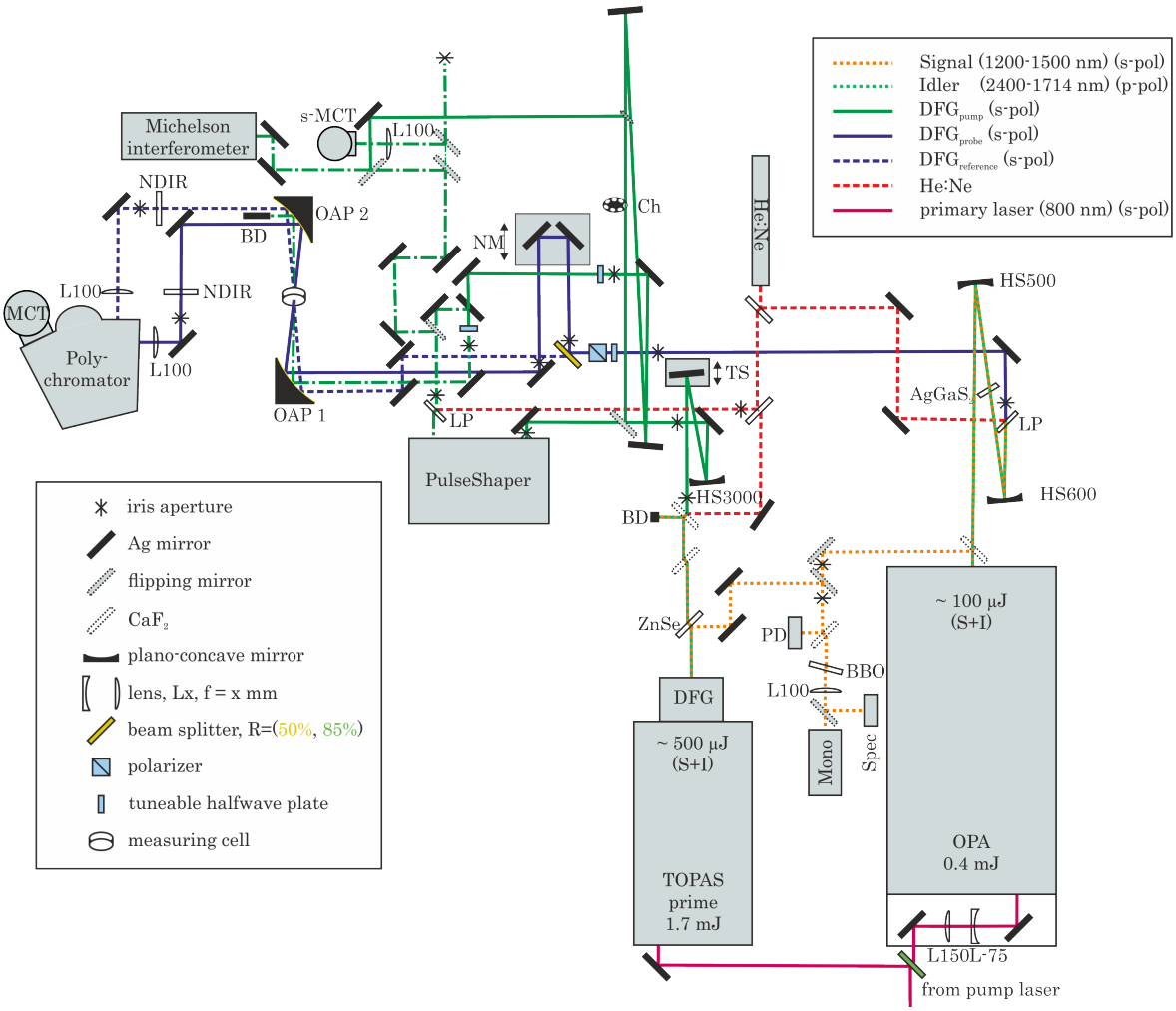

Figure 3.1: Scheme of the experimental setup of the time-resolved IR spectrometer. $AgGaS_2$: silver gallium sulfide crystal ($\theta = 39°$,$\phi = 45°$, type-I); BBO: barium β-borate crystal ($\theta = 19.8°$, $\phi = 0°$, type-I); BD: beam dump; CaF_2: Calcium fluoride substrate ($d = 5$ mm); Ch: rotating punch disc (Chopper); FM: folding mirror; He:Ne: Helium-Neon laser; HSx: plano concave mirror (ROC =-x mm); Lx: lense (ROC = +x mm); LP: long pass filter; MCT: MCT array (HgCdTe); s-MCT: single MCT; Mono: Monochromator; NDIR: neutral density filter for IR light; NM: Nanomover, computer controlled delay stage; OAP: off-axis parabolic mirror ($RFL = 101.6$ mm, $d = 2\,''$, 90°); OPA: optical parametric amplifier, home-built; PD: photo diode; Spec: Spectrometer for visible specral range; TOPAS: optical parametric amplifier, Light Conversion; TS: translation stage; ZnSe: ZnSe beamsplitter with Ge coating.

primary laser light (1.7 mJ) is directed into a computer controlled, commercial available optical parametric amplifier (OPA)(TOPAS; Light Conversion, TOPAS prime). The TOPAS provides a Signal wave (available in a spectral range from 1140 nm up to 1580 nm) and a corresponding Idler wave (2680 nm to 1620 nm). Both collinear traveling waves are used for a subsequent difference frequency generation (DFG) to generate ultra-short laser pulses in the mid-infrared (mid-IR) regime. For that, both waves are

spatially separated, then collinear and temporally overlapped and finally directed in a type-I $AgGaS_2$ ($\theta = 39°$, $\phi = 45°$) crystal. Afterwards, Signal and Idler waves are separated from the difference frequency using a Ge coated ZnSe beam splitter (ZnSe; Altechna, ZnSe coated with Ge, HR_s = (1.26-1.53) µm (>99 %), HR_p = (1.67-2.18) µm (>98 %), HT_p = (2.8-20) µm, $AOI = 45°$). The generated difference frequency in the mid-IR is used in the following setup as the pump pulses. The remaining part of the Signal wave is utilized to monitor the pulse-to-pulse stability with a Ge photo diode (PD; GPD Optoelectronics, GM8) and the spectral position with a polychromator. For the latter, the Signal wave is frequency doubled and focused onto the entrance slit of a monochromator (Mono; Bausch und Lomb, 33-96-76, 600 grooves mm^{-1}, Detector: Hamamatsu, S3901-512Q, 512 Pixels) or a spectrometer (Spec; Ocean Optics, STS-VIS spectrometer). The mid-IR light passing the ZnSe beam-splitter, traverse a calcium fluoride (CaF_2) substrate, which is inserted to collinear overlap a fraction of the light of a Helium-Neon laser (He:Ne; Melles Griot, $P = 15$ mW, $\lambda = 632.816$ nm) with the pump beam. With the help of apertures integrated in the experimental setup and a power meter, the invisible infrared pulses can be spatially overlapped with the visible light of the He:Ne laser.

The transmitted (15 %, $P = 0.4$ W) primary laser light is directed towards a home-built OPA. It was originally built as a two-stage collinear optical parametric amplifier by Seehusen [66] based on the publications of Hamm et al. [70] and Kaindl et al. [71]. As part of this work, the existing OPA was redesigned. The amplification within the first stage proceeds now non-collinear in a type-II barium β-borate crystal ($\theta = 28°$, $\phi = 30°$) and in the second stage collinear in the same crystal. The generated Signal and Idler waves are spatially and temporally overlapped for the oncoming difference frequency generation. A flipping mirror can be inserted in the output beam of the OPA to monitor the pulse-to-pulse stability and the spectral position of the Signal wave with the above mentioned photo diode and polychromator. Following the beam path, Signal and Idler waves are focused with a concave mirror (HS500; plano-concave mirror, radius of curvature ROC = -500 mm) into a type-I $AgGaS_2$ crystal and finally collimated (HS600; plano-concave mirror, ROC = -600 mm). The generated mid-IR pulses are used as probe pulses. The non-converted Signal and Idler waves are separated using a long-pass filter (LP) (Spectrogon, LP-2440 nm), which also serves for overlapping the visible He:Ne laser light with the invisible mid-IR pulses (see figure 3.1).

In the detection path, the generated pulses pass a combination of an adjustable half-wave plate (Alphalas, tuneable phase retardation plate ($\lambda/2$)) and a wire-grid polarizer

(Optometrics), which allows the attenuation of the pulse intensities. Afterwards, the pulses are split at a ratio of about one-to-one into reference and probe pulses. The latter ones are directed via mirrors to a computer controlled delay stage (NM; Melles Griot, Nanomover) before probe and reference pulses reach the sample chamber. Here, they are focused into the sample cell and collimated behind by a pair of off-axis parabolic (OAP) mirrors (OAP1 and OAP2; Thorlabs, reflected focal length RFL = 101.6 mm, d = 2 ″, 90°), respectively. Subsequently, both beams are focused onto the entrance slits of a polychromator (Polychromator; HORIBA Jobin Yvon, iHR320) using plano-convex lenses (CaF_2, focal length f = +100 mm). Inside the polychromator, reference and probe pulses traverse with an offset in height a blazed grating (75, 100, 150 or 300 grooves mm^{-1}), disperse similarly and finally, are mapped onto two lines of a 2 x 32 pixel mercury cadmium telluride detector (MCT; Infrared Associates). The electrical signals originating from the MCT-array were amplified and digitized with commercial available electronics (Infrared Associates, MCT-6400) and directed to a PC, which also controls the polychromator and the translation stage. To avoid saturation of the detector, the intensity of the pulses can be further attenuated with the help of specific reflective neutral density filters for IR light (NDIR; Thorlabs, OD range 0.3 to 2.0, λ = (2 - 16) µm), which are inserted into the optical path before the pulses are focused onto the slits of the polychromator.

The pump pulses traverse a manually controllable translation stage (TS) with an adjoining concave mirror (HS3000; plano-concave mirror, ROC = -3000 mm) to collimate the pump pulse beam before it enters the pulse shaper (PulseShaper; PhaseTech spectroscopy shaping science, QuickShape IR). Inside, the pump pulses are modulated in shape, width and center frequency (for application of pump-probe spectroscopy) or they are used to generate a pulse sequence with adjustable temporal delay (for application in 2D-IR spectroscopy). Afterwards, the beam passes a half-wave plate (Alphalas, tuneable phase retardation plate ($\lambda/2$)) setting a relative angle of 54.7° (magic angle) between the polarization of pump and probe pulses. In this configuration, signal contributions from reorientational dynamics are diminished. Subsequently, the pump pulses are focused into the sample cell with the aforementioned off-axis parabolic mirror OAP1, then collimated with OAP2 and blocked afterwards with a beam dump.

To monitor the spectra of the pump pulses, an existing home-built Michelson interferometer is implemented into the experimental setup. Flipping mirrors allow to select beam paths to record interferogram of the pulses before entering and after leaving the pulse shaper. Furthermore, an interferogram of the pump pulses generated with the pulse shaper can be recorded using a single element MCT detector (s-MCT; Infrared

Associates, MCT-13-1.0).

Within the scope of this work, measurements are performed in the mid-IR regime, where atmospheric absorptions occur. To prevent distortions of the spectra delivered by DFG from the OPAs, the entire experimental setup was encapsulated and purged with dry air or nitrogen.

Principle of operation of a pulse shaper

In this section, the fundamental principle of operation of a pulse shaper in the mid-IR regime, implemented in the above described pump-probe spectrometer, will be explained.

The pulse shaper used within this work consists of two diffraction gratings, two off-axis parabolic mirrors in $4f$-geometry and an acousto optic modulator (AOM) based on a Ge-crystal (figure 3.2 (b)). The principle of the optical setup with lenses instead of mirrors is depicted in figure 3.2 (a), and is based on the concept presented by Froehly et al. [88].

The input beam is impinged on the first diffraction grating (figure 3.2 (a), left), where the different frequency components of the pulse are angular dispersed. The grating is placed in the back focal plane of the subsequent lens with focal length f. The latter collimates and focuses the dispersed components onto the Fourier plane, which is in its front focal plane. At the same time, the Fourier plane is in the back focal plane of a second lens, which collimates all frequency components and combines them on a second grating in the front focal plane into a single collimated beam [88, 89]. To modulate the phase and amplitude of an incoming pulse, a mask is inserted in the Fourier plane. Within this work, an acousto-optic modulator (AOM), whose application in the context of pulse shaping in the visible regime has been developed by Warren and coworkers in 1994 [90], is used to provide customized masks.

Both the $4f$-geometry as well as the application of an AOM are combined in the setup of a commercial available pulse shaper from PhaseTech spectroscopy shaping science, developed by M. T. Zanni and C. T. Middleton. To avoid unwanted dispersion and chromatic aberrations of ultra-short pulses with broad spectral bandwidth, the lenses are replaced by 1D off-axis parabolic mirrors [91]. A scheme of the adapted layout is shown in figure 3.2 (b). The incoming beam is reflected with a gold mirror onto the first diffraction grating, directing the angular dispersed frequency components onto the first off-axis parabolic mirror. The subsequent AOM based on a Ge-crystal is designed to

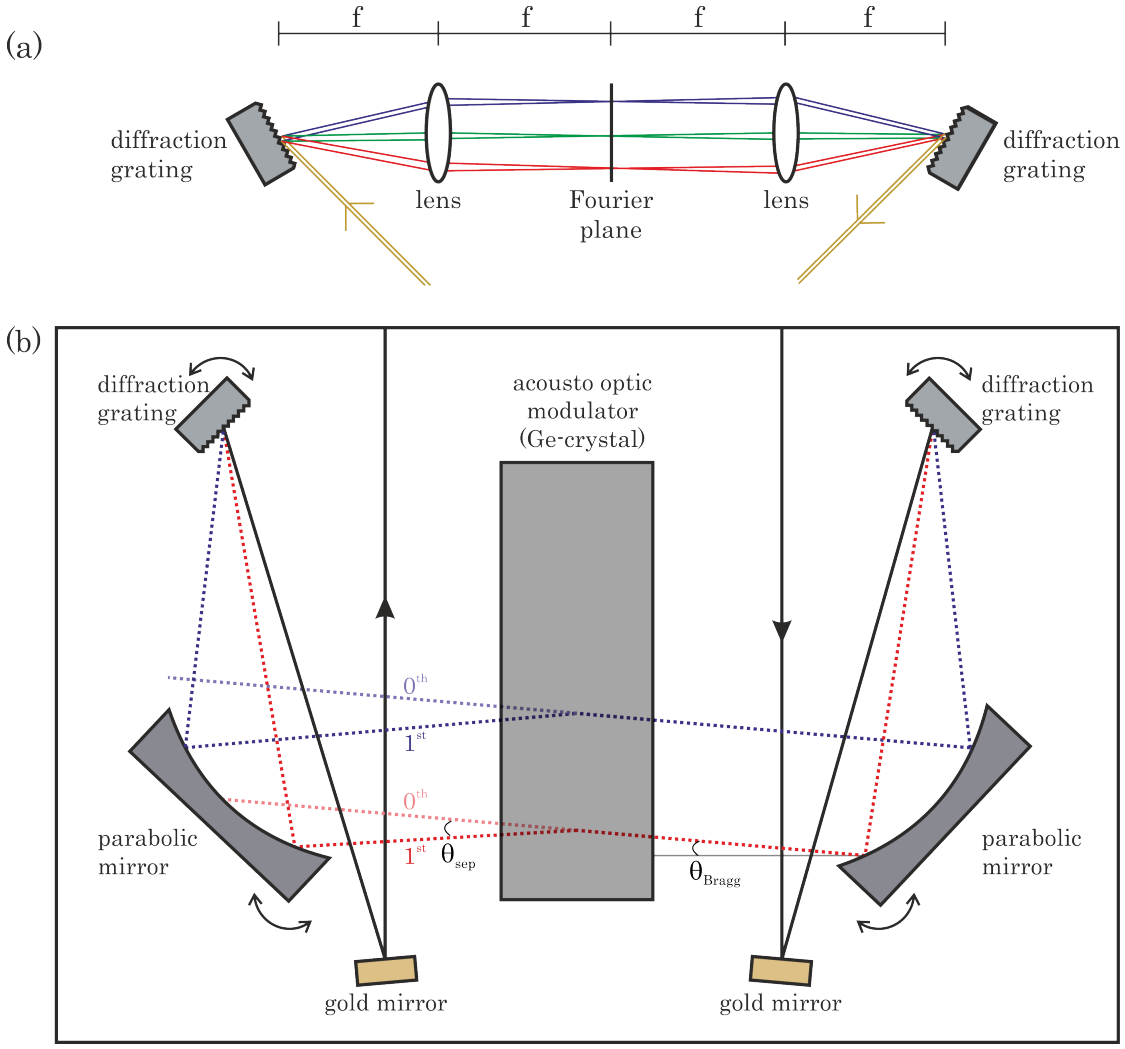

Figure 3.2: Optical layouts for pulse shaping.
(a) Scheme of $4f$-geometry based on the concept presented by Froehly et al. [88].
(b) Optical layout and beam path of the commercially available pulse shaper.

maximize diffraction of the input beam into a single first order direction. Its principle of operation is based on the acousto-optic effect describing the interaction of an acoustic wave with an electromagnetic field [92]. The following off-axis parabolic mirror directs the frequency components of the first order beam leaving the AOM towards a second grating, which combines them into a single collimated beam.

To operate the AOM, an arbitrary waveform generator (AWG) is needed. It generates desired waveforms, which are directed into a radio frequency (RF) power amplifier (RFA). Within the RFA, the AWG's temporal RF voltage signals are amplified and applied to the AOM. A piezoelectric transducer converts the RF voltage signal into a traveling acoustic wave [93] (see the scheme of the principle of the AOM in figure

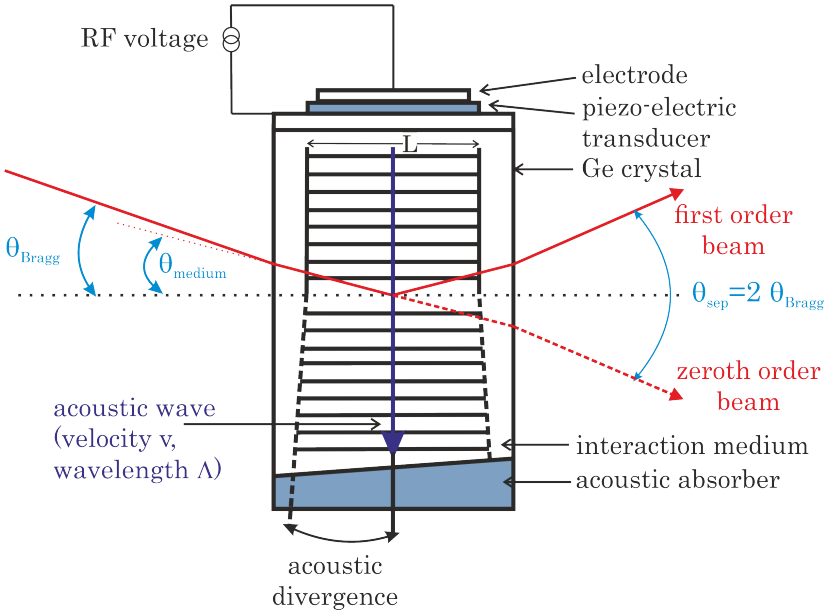

Figure 3.3: Scheme of the AOM principle adapted from [93]. A piezoelectric transducer converts the RF voltage signal into a traveling acoustic wave, which causes changes in the refractive index of germanium. The incoming laser beam with a Bragg angle (θ_{Bragg}) with respect to the normal on the optical surface of the Ge-crystal is deflected into zeroth and first order beam, which are separated by angel θ_{sep}.

3.3 [93]). This wave with wavelength Λ propagates through the crystal and causes periodic changes in the refractive index of germanium (photo-elastic effect), because it creates areas of compression and rarefaction [90, 93]. To avoid reflections of the acoustic wave creating secondary diffraction the acoustic wave hits an absorber [93]. If the interaction range (L) of the acoustic wave is large compared to the wavelength Λ, then the AOM operates in the Bragg regime[1] [92]. Herein, only first order diffraction as well as the transmitted zeroth order beam are observed.

The underlying acousto-optic effect can be introduced with a model, in which the interaction is described as a collision between photons and phonons [92]. The incident light wave can be comprehended as a particle flow of photons with energy E_{phot} and momentum $\mathbf{p}$

$$E_{\text{phot}} = h \cdot \frac{c}{\lambda}, \ \mathbf{p} = \frac{h}{2\pi} \cdot \mathbf{k} \tag{3.1}$$

where h denotes Planck's constant, λ the wavelength of a photon, c the speed of light and $\mathbf{k}$ the wave vector of a photon. Similarly, the acoustic wave can be thought of a quasi particle flow with energy E_{phon} and momentum $\mathbf{P}$

[1] Otherwise in the Raman-Nath regime, resulting in multiple diffraction orders [92].

$$E_{\text{phon}} = h \cdot \frac{\text{v}_{\text{Ge}}}{\Lambda},\ \mathbf{P} = \frac{h}{2\pi} \cdot \mathbf{K}. \tag{3.2}$$

Here, v_{Ge} describes the velocity of the acoustic wave in Ge, Λ the wavelength of a phonon and **K** its wave vector. From the conservation of energy and momenta, it follows

$$\begin{aligned} E_{sc} &= E_{\text{phot}} \pm E_{\text{phon}} = h\left(\frac{c}{\lambda} \pm \frac{\text{v}_{\text{Ge}}}{\Lambda}\right) \\ \mathbf{p}_{sc} &= \mathbf{p} \pm \mathbf{P} = \frac{h}{2\pi}(\mathbf{k} \pm \mathbf{K}) = \frac{h}{2\pi}\mathbf{k'}, \end{aligned} \tag{3.3}$$

where E_{sc} is the energy and $\mathbf{p}_{sc}$ the momentum of the scattered light. The latter equation is illustrated in figure 3.4, in which the wave vector **k'** is given by the addition of wave vectors **K** and **k**.

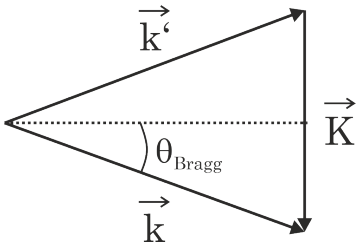

Figure 3.4: Illustration of conservation of momenta of photons and phonons with wave vector **k** of photons, **K** of phonons and **k'** as the addition of both vectors.

From this reflection, the Bragg angle can be calculated according to

$$\sin(\theta_{\text{Bragg}}) = \frac{1}{2}\frac{|\mathbf{K}|}{|\mathbf{k}|}. \tag{3.4}$$

With $K = |\mathbf{K}| = (2\pi)/\Lambda$ and $k = |\mathbf{k}| = (2\pi)/\lambda$, eq. (3.4) results in

$$\sin(\theta_{\text{Bragg}}) = \frac{1}{2}\frac{\lambda}{\Lambda}. \tag{3.5}$$

As can be seen from figures 3.3 and 3.4, the zeroth and first order are separated by an angle $\theta_{\text{sep}} = 2\,\theta_{\text{Bragg}}$.

With a given photon wavelength of $\lambda = 4.2$ µm as well as a phonon wavelength of $\Lambda = f/\text{v}_{\text{Ge}} = 13.64$ µm with $f = 75$ MHz [94] and $\text{v}_{\text{Ge}} = 5500$ ms^{-1} [95], a Bragg angle of $\theta_{\text{Bragg}} = 1.6°$ can be calculated. This angle is experimentally realized by rotating

the off-axis parabolic mirror mounted via the rotation stage. This varies the angle between the reflected beam from the off-axis parabolic mirror and the normal of the Ge-crystal's surface (see figure 3.2 (b)). A second off-axis parabolic mirror, mounted on another rotation stage, collimates the first order beam and directs it towards a second diffraction grating, where all the frequency components are recombined into a single beam. A second gold mirror is finally used to couple the beam out of the pulse shaper.

In general, deflection and propagation in the Ge-based AOM adds a linear chirp to the pulses, which is compensated by combining the mask for the desired experiment with one correcting for dispersion originating from the pulse shaper itself [96].

To account for the modulator performance and the output beam characteristics, the ratio of optic and acoustic divergence is considered, the so-called beta factor.

$$\beta = \frac{\lambda\, L\, f}{n\, \omega_0\, \mathrm{v_{Ge}}} \tag{3.6}$$

with the wavelength λ, the interaction length L of the Ge-crystal, the radio frequency f, the refractive index n, the beam waist ω_0 and the acoustic velocity $\mathrm{v_{Ge}}$. From this, it is obvious that the beta factor and thus, the diffraction efficiency reduces as the beam becomes increasing focussed [93].

Specifications of the pulse shaper

In the following subsection, specifications such as the efficiency as well as characteristic pump pulse spectra of the pulse shaper generated within the scope of this work are introduced.

Table 3.1: Efficiencies of the original (o) as well as of the modified (m) pulse shaper, specified with the constants g of the applied gratings for different wavelengths.

wavelength λ / µm	**grating constant g / grooves mm^{-1}**	**Efficiency**
4.76 (o)	300	30 %
4.28 (m)	300	45 %
6.15 (m)	150	30 %

The measurements were performed with a slightly modified [97, 98] pulse shaper. Its output efficiencies for two different wavelengths and gratings are summarized and com-

pared to those of the original optical setup in table 3.1. According to the specifications of PhaseTech, the pulse shaper has an output efficiency of more than 25 % at a wavelength of 5 µm [99], while the diffraction efficiency of the AOM is specified to around 80 % [100]. However, the slightly modifications of the pulse shaper result in similar, in some cases in increased output efficiencies.

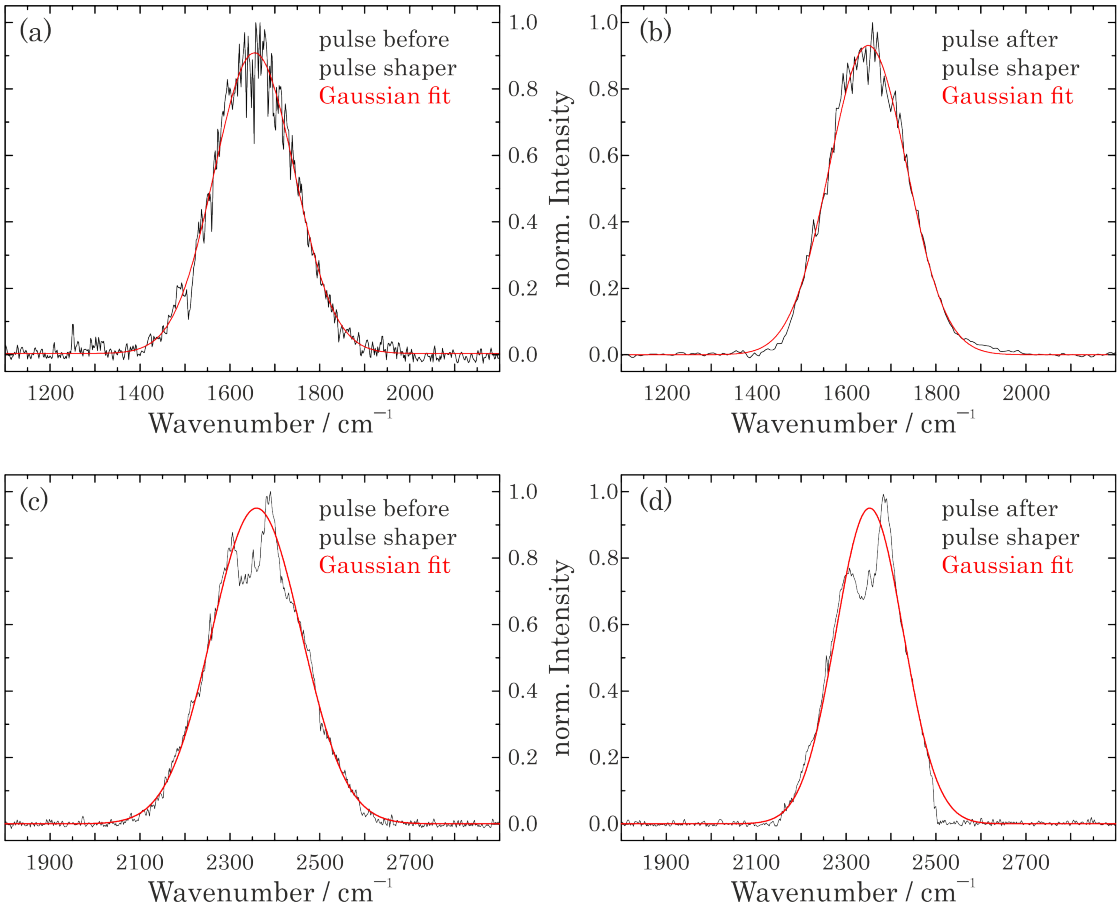

Figure 3.5: Spectra of pump pulses (black) before entering (a, c) and after leaving (b, d) the pulse shaper at a center wavenumber of 1650 cm^{-1} and 2350 cm^{-1}. The spectra were adapted with a Gaussian function (red line). Deviations of the experimental spectra in (c) and (d) from Gaussian shape originate from remaining CO_2 absorptions due to incomplete purging.

In figure 3.5, spectra of pump pulses are shown before entering (a, c) and after leaving (b, d) the modified pulse shaper. The spectra were recorded by means of the implemented Michelson interferometer, subsequently analyzed and adapted with a Gaussian function

$$f(\nu) = A \cdot \exp\left(-\frac{1}{2}\left(\frac{\nu - \nu_c}{w}\right)^2\right). \tag{3.7}$$

Here, A denotes the amplitude, ν a frequency, ν_c the center frequency and w the width of a pulse. Its full-width at half-maximum (FWHM) is then

$$\text{FWHM} = 2w\sqrt{\ln(4)}. \tag{3.8}$$

Before adapting the Gaussian function, a baseline correction was performed, where a straight line was subtracted, and the spectra were normalized afterwards. In figures 3.5 (c) and (d), the amplitude of the Gaussian is fixed to 0.95, because the pump pulse spectra are affected by remaining absorptions of atmospheric CO_2 at around 2350 cm^{-1} in the around 3 m long pathway from the DFG to the Michelson interferometer. The adapted parameters as well as the coefficient of determination[2] are given in table 3.2.

Table 3.2: Results of adapted Gaussian function for the pump pulse spectra of figure 3.5. Center frequency ν_c, amplitude A, FWHM as well as coefficient of determination R^2 are given.

	ν_c / cm^{-1}	Amplitude A	FWHM / cm^{-1}	R^2
(a)	(1654.7 ± 0.4)	(0.905 ± 0.003)	(209.5 ± 0.9)	0.980
(b)	(1649.1 ± 0.6)	(0.931 ± 0.005)	(203.4 ± 1.5)	0.994
(c)	(2359.2 ± 0.7)	0.95	(234.7 ± 1.3)	0.979
(d)	(2352.4 ± 0.7)	0.95	(176.8 ± 1.4)	0.961

In figures 3.5 (a, b) and table 3.2, it can be observed that the FWHM of the pulses decreases by 3 % when the pulses are directed into the pulse shaper and detected afterwards. This decrease is more pronounced in (d). Here, the deviation amounts to almost 25 % comparing the FWHM of the pulses before entering (c) and after leaving (d) the pulse shaper. The reason for this could be found in a misalignment of the pulse shaper. It has to be ensured that the incoming beam is on the acoustic axis and central to the aperture width of the AOM.

[2]R-squared or coefficient of determination is a measure to qualify the accuracy of a dependence between variables [101].

3.2 Stationary cell and high-temperature high-pressure cell

In this section, the stationary and the high-temperature high-pressure (HTHP) cell are shortly presented. A more in depth description can be found elsewhere [29, 102, 103].

The stationary cell consists of two CaF_2 windows with a radius of $r = 17$ mm and a thickness of $d = 4$ mm (Eksma Optics), which are held on a distance of 100 µm with a Teflon spacer. This cell can be equipped with valves linked to the cell body for filling under purging with nitrogen.

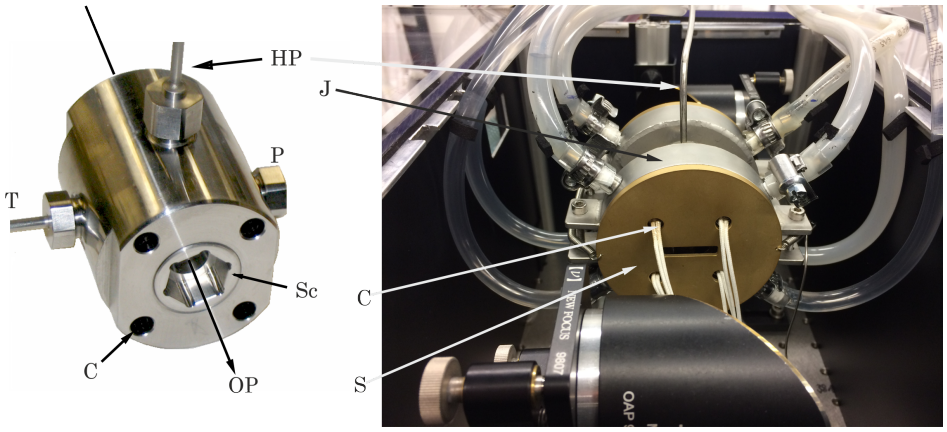

Figure 3.6: Scheme of the used high-temperature high-pressure cell (left side) [29] and implemented HTHP cell with external cooling jacket and shielding in experimental setup of the pump-probe spectrometer (right side).
C: opening for heating cartridge, HP: high-pressure supply, J: external cooling jacket, OP: optical path, P: filler plug, S: shielding, Sc: pressure screw, T: thermocouple.

The high-temperature high-pressure (HTHP) cell (see figure 3.6, left side) with an associated high-pressure system was built by the mechanical workshop of the Institut für Physikalische und Theoretische Chemie based on an already existing system [104]. The body of this cell is made from nickel containing alloy and is equipped with two stamps each including a sapphire window. The window is customized by Korth Kristalle and possesses a radius of $r = 2.5$ mm and a thickness of $d = 2.5$ mm. The upper side has a chamfered edge with an angle of 45°. The sapphire windows are sealed within the stamps with gaskets made from gold foil (Alpha Aesar, thickness $d = 25$ µm). A layer thickness of around 25 µm between the inner surfaces of the windows within the cell was realized.

To prevent heating of neighboring optical components of the experimental setup, a cooling jacket [103] (J; figure 3.6, right side) linked to an external water circuit was

necessary. Furthermore, shieldings (S) perpendicular to the optical path (OP; figure 3.6, left side) were added on both sides of the cell to avoid radiation of heat in this area. Both shieldings contain openings for beams traversing the cell as well as for four heating cartridges (C). Using the described HTHP cell equipped with the external cooling, measurements at a pressure of 500 bar and temperatures up to 603 K were possible.

3.3 Sample preparation

This section describes shortly the preparation of the investigated samples in this work. Table 3.3 gives a list of chemicals used. Solvents as well as the solutes were commercially available.

Table 3.3: Chemicals with degree of purity, isotopic composition and producer as used for measurements within the scope of this work. (CIL: Cambridge Isotope Laboratories)

Series of experiment	**Substance**	**Producer**	**Degree of purity (isotopic composition)**
CO_2 in H_2O	CO_2	Air Liquide	99.998 %
	H_2O	–	18 MΩ · cm, doubly deionized
OCN^- in H_2O	NaOCN	Sigma Aldrich	96 %
	$KO^{13}CN$	CIL	95 % (^{13}C: 98 %)
	$KO^{13}C^{15}N$	CIL	95 % (^{13}C: 99 %, ^{15}N: 98 %)
	H_2O	–	18 MΩ · cm, doubly deionized
trans-4-methoxybut-3-en-2-one in C_2Cl_4	*trans*-4-methoxybut-3-en-2-one	Sigma Aldrich	90 %
	C_2Cl_4	Acros	99 %

All samples were prepared under standard laboratory conditions. For preparation of an aqueous carbon dioxide solution, gaseous CO_2 was passed into 10 mL of deionized H_2O in a round-bottomed flask for 10 min. To transfer the solution directly into the high-pressure system, an excess of gaseous CO_2 in the gas-filled compartment of the flask as well as a pressure below that of the lab environment within the high-pressure system were applied. Consequently, a CO_2 concentration of 0.09 mol/L was achieved.

The concentrations of the three aqueous cyanate isotopologue solutions were adjusted to 0.10 mol/L, dissolving a mass of 65.01 mg of NaOCN, 82.12 mg of $KO^{13}CN$, and 83.12 mg of $KO^{13}C^{15}N$ in deionized H_2O. No purifications of the solutes were necessary.

Before preparing a solution of *trans*-4-methoxybut-3-en-2-one in C_2Cl_4, the solvent C_2Cl_4 was dried in advance by a molecular sieve. The *trans*-4-methoxybut-3-en-2-one was used without further purification, and the preparation of the solution was performed under purging with nitrogen. The concentration was set to 0.072 mol/L.

3.4 Post-processing of experimental data

The experimental data, which were measured within the scope of this work, were post processed. In the following section, the procedure is described.

The spectra recorded with the FTIR spectrometer (section 2.2) were taken over without any further post-processing. Using Lambert-Beer's law (eq. (2.30)), the optical density of the sample OD_{sample} as well as of the solvent $OD_{solvent}$ and the differential optical densities $\Delta OD = OD_{sample} - OD_{solvent}$ were determined. As a reference, the spectrum of the empty stationary or HTHP cell was applied to remove the background, which originates from the material of the cell windows. Table 3.4 lists the experimental settings, which were used to record the stationary absorption spectra.

Table 3.4: Parameters entered for measuring stationary absorption spectra using both the stationary as well as the HTHP cell.

Series of experiment	**Cell type**	**Number of Scans**	**Resolution / cm^{-1}**
CO_2 in H_2O	stationary	16	0.25
	HTHP	128	1
OCN^- in H_2O	stationary	128	1
	HTHP	128	1
trans-4-methoxybut-3-en-2-one in C_2Cl_4	stationary	16	0.5

In the following, the post-processing of the different series of experiments by means of pump-probe and 2D-IR spectroscopy is introduced.

Post-processing of experimental data of aqueous carbon dioxide solutions

The solution of CO_2 dissolved in deionized H_2O was excited with a narrow-band Gaussian-shaped pump pulse. The full-width at half-maximum of the pump pulse was adjusted to match that of the asymmetric stretching vibration of CO_2 (from 2325 cm^{-1} to 2375 cm^{-1}), the vibrational mode of interest. Since the line width of the $\nu_{as}(CO_2)$ mode rises with isobaric heating, the FWHM of the pump pulse was increased too, while its center frequency was set to 2343 cm^{-1} over the whole temperature range. Within the series of measurements, the polychromator described in section 3.1 was used applying a grating with 150 grooves mm^{-1}. To record the spectral narrow-band absorption of CO_2 more precisely, the number of pixels for detection is raised virtually. To achieve this, the center frequency of the polychromator is shifted n times in fractions of one n^{th} of the spectral pixel width of the array detector. This process is called stitching. Considering the number of grooves of the applied grating, the spectral pixel width is equal to a wavelength interval of 10 nm. Hence, a twofold stitching ($n = 2$) with $\lambda_{\mathrm{Poly}} = 4279$ nm and $\lambda'_{\mathrm{Poly}} = 4284$ nm was chosen to obtain $32 \cdot n = 64$ data points per delay time. However, it has to be considered that the effective spectral resolution of the polychromator is not enhanced.

An aqueous solution was investigated for eleven thermodynamic state points (pressure and temperature). For each condition, spectrally resolved pump-probe data were recorded in four runs, each one sampling 176 delay times. For each temporal delay, the signal was averaged over 1000 cycles consisting of recording $OD_{w/pump}$ and $OD_{w/o\,pump}$. The data were post-processed with the help of a self-written program in MATLAB using a graphical user interface (GUI). Within this program, data points at a specific delay time were sorted by wavelength and averaged over all runs. The data set of each delay time could be sighted individually to erase sporadic outliers due to fluctuations in laser stability (point-to-point fluctuations). To correct for a non-zero ΔOD base line, two pixels can be defined to estimate a polynomial function of first order, whose wavelength-dependent values are deducted from the data. Afterwards the abscissa was adjusted for each thermodynamic point. Uncertainties in the beam directions when entering the monochromator and some ambiguity in the focal position of the MCT array result in slight variations of the dispersion (in nm/Pixel) and the absolute wavelength calibration. Provided at least two signals with known wavelengths for calibration, the

wavelength scale can be corrected according to

$$\lambda_{corr} = \zeta \cdot \lambda_{orig} + \Delta\lambda. \tag{3.9}$$

Here, λ_{corr} is the corrected wavelength, λ_{orig} the one set at the polychromator, ζ a factor describing the compression or elongation of the wavelength axis and $\Delta\lambda$ an offset of the wavelength. To determine the parameter ζ and $\Delta\lambda$, either a suitable calibration component or characteristic and well-known resonances within the pump-probe spectrum can be used. In general, ζ is almost equal to one, while $\Delta\lambda$ can deviate by about 30 nm if the calibration of the abscissa was not performed before starting the experiment.

Post-processing of experimental data of aqueous cyanate solutions

Within the series of pump-probe measurements of aqueous cyanate solutions, the experiments were performed using a different polychromator[3] (AMKO, Multimode 4, focal length $f = 0.2$ m) than the one described above (section 3.1). Its center wavelength was adjusted to $\lambda_{Poly}(\mathrm{OCN^-}) = 4610$ nm, $\lambda_{Poly}(\mathrm{O^{13}CN^-}) = 4740$ nm and $\lambda_{Poly}(\mathrm{O^{13}C^{15}N^-}) = 4775$ nm. For each thermodynamic state point, two runs with 1000 pulses per delay time each and 166 delays per run were performed. The analysis of the experimental data was realized in a similar manner as described above.

Post-processing of two-dimensional experimental data

Time domain two-dimensional mid-IR spectra were recorded using the pulse shaper to generate a sequence of two pulses with delays increasing in 4 fs steps up to 3296 fs. A total number of 160 sequences per delay time (population time) between pump and probe pulse was set.

For each sequence, the recorded interferogram can contain artifacts due to truncation when the emitted signal has not fully decayed within the coherence time [56]. A Fourier transformation of such an interferogram gives a line shape with side lobes in the frequency domain, which can be avoided by multiplying a given function with the interferogram prior to its Fourier transformation, a procedure called apodization [105].

[3]These series of measurements were performed with the experimental setup described in section 3.1. However, at that time, neither the polychromator iHR320 nor the pulse shaper were available. Instead the AMKO polychromator and a chopping disk were used.

Within the scope of this work, a triangular apodization according to

$$f(t) = 1 - \frac{|t|}{t_{max}} \tag{3.10}$$

was applied. Here, t denotes the difference in and t_{max} the maximum delay of coherence time.

The observed signal intensities $I(\nu_{probe}, \nu_{pump})$ are displayed in contour plots. For better visibility of small signals, the intensity axis was non-linearly stretched with $f(I) = \tanh(2\ I)$. Afterwards, the post-processed data were normalized and plotted with 30 contours. The probe axis (abscissa) was dispersion corrected applying the procedure described above. Here, $\zeta = 1.005$ and $\Delta\lambda = 27$ nm were determined. The latter corresponds to a mean displacement of the abscissa by around 1.3 pixels. No further post-processing was applied.

Chapter 4

Results and discussion

This chapter is divided into three sections. The first one deals with the temperature-dependent stationary and time-resolved pump-probe measurements of molecular dissolved carbon dioxide in H_2O. In doing so, the temperature-dependent stationary FTIR spectra are analyzed and discussed in the context of the line shape theory of Kubo and Anderson (see section 2.3) [80, 81]. The pump-probe spectra in turn, are analyzed in the context of the vibrational energy redistribution mechanism.

The second section is then used to present and discuss temperature-dependent stationary and pump-probe spectra of three cyanate isotopologues dissolved in H_2O. These measurements follow up investigations of aqueous pseudohalide anions performed earlier in the Vöhringer group [28, 32, 106]. In the end of this section, the results are analyzed in the context of Fermi's golden rule and compared with those previously obtained for pseudohalide anions in H_2O. Furthermore, a comparison between the underlying vibrational energy redistribution mechanisms of CO_2 and OCN^- in H_2O is drawn.

In the third section, the two-dimensional infrared spectra of *trans*-4-methoxybut-3-en-2-one in tetrachloroethylene are presented with the aim to study the underlying conformational dynamics.

4.1 Infrared spectroscopy of carbon dioxide in liquid-to-supercritical H_2O

As it is known from the literature [107], the CO_2 and H_2O are in equilibrium with each other. The equilibrium between both can be described by the following equations

$$\begin{aligned} CO_{2(aq)} + 2\ H_2O &\rightleftharpoons {HCO_3}^-{}_{(aq)} + H_3O^+_{(aq)},\ K = 4.47 \cdot 10^{-7} \\ {HCO_3}^-{}_{(aq)} + H_2O &\rightleftharpoons {CO_3}^{2-}{}_{(aq)} + H_3O^+_{(aq)},\ K' = 4.68 \cdot 10^{-11}, \end{aligned} \tag{4.1}$$

K and K' being the equilibrium constants. At room temperature and a pressure of 1 bar, the equilibrium is shifted towards the reagents so that less than 1 % of CO_2 is hydrolyzed to H_2CO_3, ${HCO_3}^-$ or ${CO_3}^{2-}$ [107–109]. Thus, there is no influence on the measurements of dissolved CO_2 in H_2O due to hydrolyzed products.

The linear carbon dioxide molecule possesses $3N-5 = 4$ normal modes (see section 2.1, figure 2.2). They are attributed to the symmetric stretching vibration ν_s, the doubly-degenerated bending vibration ν_b and the asymmetric stretching vibration ν_{as}. The linear geometry of CO_2 combined with a center of inversion leads to a classification in a $D_{\infty h}$ point group, so that the rule of mutual exclusion[4] holds. The assignment of the normal modes to their corresponding spectroscopic activity can be found in section 2.1. In the context of the investigation of dissolved carbon dioxide in H_2O, the asymmetric stretching vibration of CO_2 is established as a vibrational probe for ultrafast mid-IR spectroscopy to investigate the dynamics and kinetics of this molecule in H_2O.

4.1.1 Temperature-dependent stationary absorption spectra of carbon dioxide dissolved in H_2O

In figure 4.1, the stationary absorption spectra of carbon dioxide in the gas phase (black) as well as dissolved in H_2O (red) with a concentration of 0.09 mol/L (see section 3.3) referenced against the solvent are shown in the spectral range from 2225 cm^{-1} to 2425 cm^{-1}, covering the region of the asymmetric stretching vibration.

It is obvious that the full-width at half-maximum of the whole band decreases when CO_2 is solvated. This pronounced effect can be ascribed to a restricted rotational motion around one of its three principle axes of inertia and that the motion is quenched on a vibrational time scale [110]. Furthermore, the wavenumber of the asymmetric

[4] In a molecule with center of inversion, a normal mode can solely be IR-active or Raman-active [12].

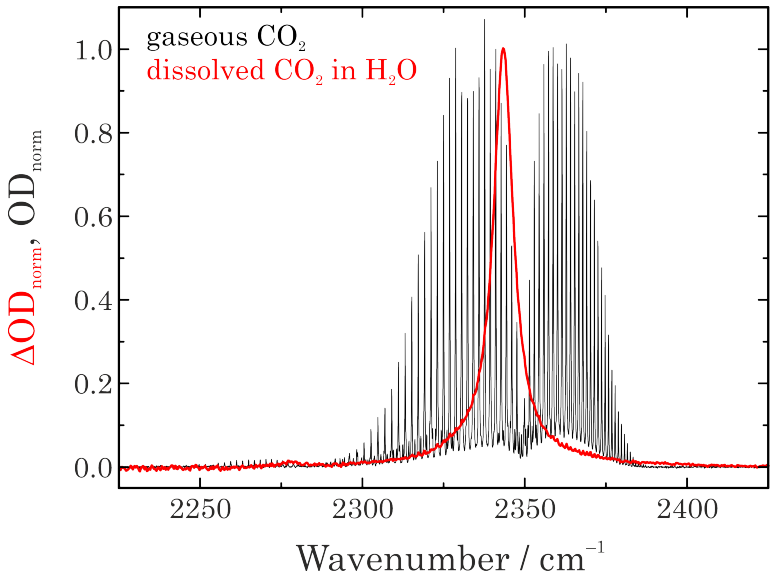

Figure 4.1: Stationary absorption spectra of gaseous carbon dioxide (black) and carbon dioxide dissolved in H_2O (red) relative to the solvent. Both spectra were recorded with a commercially available FTIR spectrometer under ambient conditions.

stretching vibration of solvated CO_2 ($\tilde{\nu}(\nu_{as}(CO_{2(aq)}))$= 2343 cm^{-1}) is almost equal to that of the isolated molecule ($\tilde{\nu_0}(\nu_{as}(CO_{2(g)}))$= 2349 cm^{-1} [110]). The lack of wavenumber shift from gaseous to carbon dioxide dissolved in H_2O indicates that its bonding to surrounding H_2O molecules is very weak [44, 110]. Zukowski et al. [111] reported about the hydration shell structure of CO_2 in H_2O and the temperature-dependent transformation of its hydration shell. Based on experimental and theoretical investigations, they predicted that the H-atoms of H_2O are primarily adjacent to an oxygen atom of CO_2 rather than to a carbon atom. Furthermore, the formation of an H-bond is endothermic (ΔH = (11 ± 2) kJ mol^{-1} [111]) and the hydration shell structure is entropically stabilized ($-T \cdot \Delta S$ = (6 ± 1) kJ mol^{-1} [111]), which implies that only about (20 ± 10) % of aqueous CO_2 molecules are H-bonded to H_2O [111].

The absorption spectrum of CO_2 dissolved in H_2O under ambient conditions is shown in figure 4.2 (a). Within the depicted spectral range, two absorption bands are observable. The narrow band can be attributed to the asymmetric stretching vibration ν_{as} of CO_2. It exhibits a pronounced spectral overlap with a broad absorption band, which corresponds to a combination tone of H_2O consisting of the bending mode ν_b and the libration mode ν_L, i.e. $(\nu_b + \nu_L)$. The narrow CO_2 absorption band is located on the high frequency side of the H_2O combination tone.

In figure 4.2 (b), the phase diagram of pure H_2O is depicted. The thermodynamic

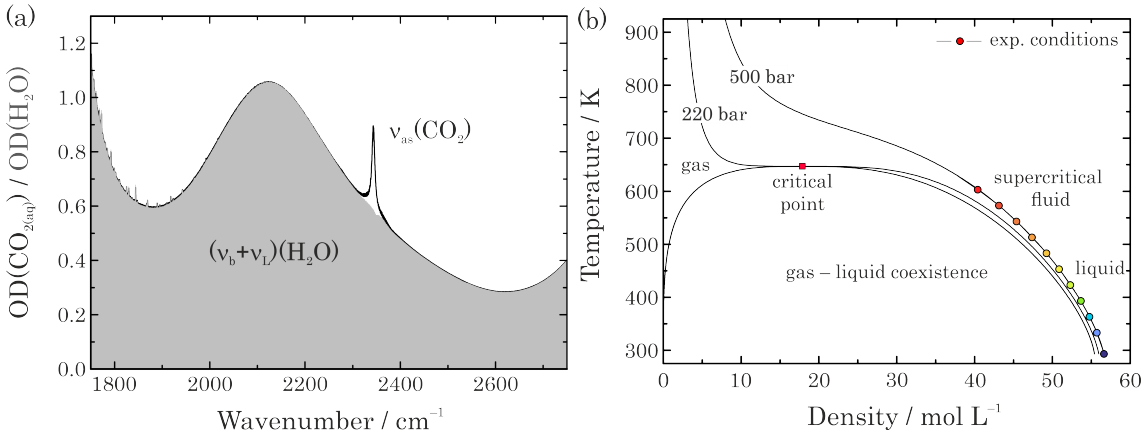

Figure 4.2: (a) Stationary absorption spectra of carbon dioxide in aqueous solution (black) and of pure H_2O (gray) under ambient conditions. The asymmetric stretching vibration of CO_2 exhibits a pronounced spectral overlap with the solvent's absorption band, which is attributed to the $(\nu_b + \nu_L)$ combination tone.
(b) Phase diagram of pure H_2O. Colored circles (blue (303 K) up to red (633 K) in intervals of 30 K) represent the investigated thermodynamic conditions. The critical point of H_2O (filled square) is described by a pressure of $p_{crit} = 221$ bar and a temperature of $T_{crit} = 647$ K [112].

conditions, at which the measurements were performed, are highlighted by filled circles. All spectra were measured at a pressure of 500 bar covering a temperature range from 303 K (dark blue filled circle) up to 633 K (dark red filled circle) and were recorded in intervals of 30 K.

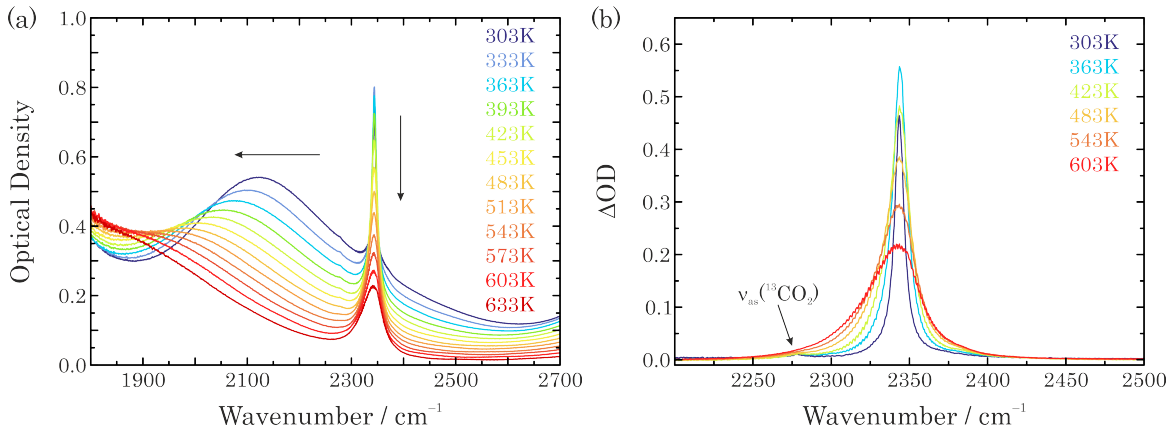

Figure 4.3: (a) Stationary absorption spectra of carbon dioxide dissolved in H_2O for the investigated temperature range. Pronounced temperature induced effects are observable and highlighted by arrows.
(b) Pure absorption spectra of carbon dioxide referenced against the solvent for different exemplaric temperatures to illustrate the temperature-dependent effects.

In the following, the temperature-dependent stationary absorption spectra of carbon dioxide in H_2O as shown in figure 4.3 (a) are discussed. Two effects can be noticed, which are indicated by arrows. Firstly, the combination tone of the solvent H_2O experiences a bathochromic shift with rising temperature, along with a change in line shape. This is due to the combined excitation of the bending mode, which is of intramolecular character, and the libration, a purely intermolecular motion of the solvent. Only the latter mode is bathochromically shifted with decreasing density of the liquid, while the spectral position of the ν_b mode remains almost constant. This results in a change of the combination tone's absorption band. Secondly, indicated by the vertical arrow, the asymmetric stretching band decreases in intensity with rising temperature. A weak absorption band centered at 2275 cm^{-1} (see figure 4.3 (b)), which is observable best at 303 K, can be attributed to the asymmetric stretching vibration ν_{as} of a small amount of dissolved $^{13}CO_2$ in solution. However, no pronounced spectral shift of the maximum of the $\nu_{as}(^{12}CO_2)$ absorption band can be observed. A temperature-dependent spectral shift of the $\nu_{as}(CO_2)$ in H_2O was calculated to be $\delta(CO_2) = (1.12 \pm 0.14) \cdot 10^{-2}$ $cm^{-1}K^{-1}$ (i. e. roughly 4 cm^{-1} within the investigated temperature interval), while the temperature-dependent shift of the combination tone of the solvent H_2O is $\delta(H_2O) = (48.1 \pm 0.2) \cdot 10^{-2}$ $cm^{-1}K^{-1}$, determined from data extracted from [113]. The latter experiences an about 40-fold stronger shift than the ν_{as} band of CO_2. Furthermore, the shape of the ν_{as} band changes as shown in figure 4.3 (b) from a Lorentzian-like shape at 303 K to an asymmetric one with an increase in line width starting at roughly 8 cm^{-1} at room temperature up to nearly 50 cm^{-1} at 633 K. An explanation for the increase in line width of the $\nu_{as}(CO_2)$ absorption band will now be given.

During isobaric heating, the density of the investigated solution decreases (see figure 4.2 (b)) resulting in a less hindered rotational motion of the CO_2 molecule around one of its three principle axes of inertia than at room temperature. This leads to an appearance of the rotational fine structure and thus, to an increase in line width. This behavior has also been reported by Kieke et al. [110]. In deed, at a temperature of 703 K the envelopes of the P- and R-branches could clearly be recognized. Nevertheless, it is questionable if this explanation is suitable to describe the observed temperature-dependent behavior satisfactorily. In the following, this explanation is supplemented by considering the vibrational manifold of carbon dioxide, which is therefore presented in figure 4.4.

In this figure, several vibrational modes and the corresponding transition wavenumbers in cm^{-1} are shown. The energies of the transitions $|000\rangle \rightarrow |00i\rangle$ with $i \in \mathbb{N}$ are

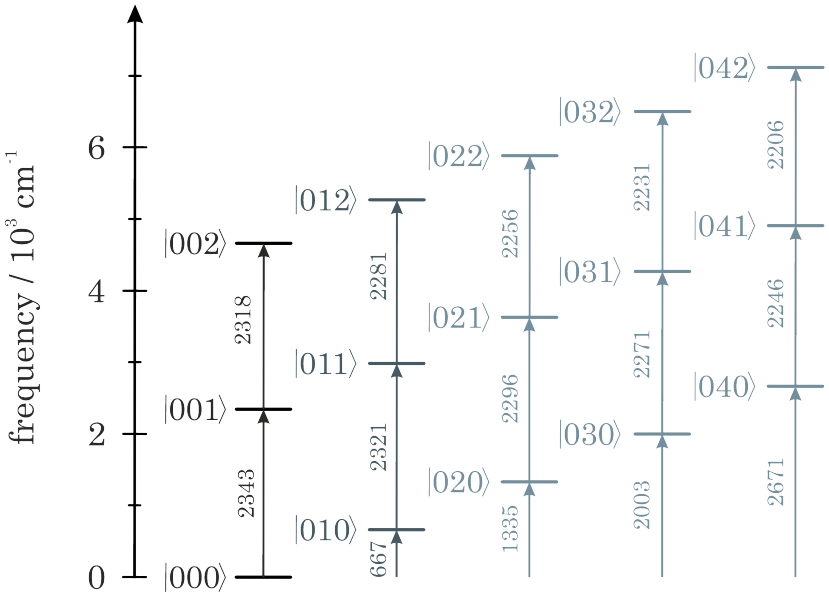

Figure 4.4: Vibrational energy level diagram of aqueous CO_2. Quantum numbers correspond to $|\nu_s\ \nu_b\ \nu_{as}\rangle$. Transitions are labeled with their respective wavenumbers in cm^{-1} and are extracted from experiment or were calculated [114, 115].

extracted from pump-probe spectra recorded within the scope of this work, those energies of transitions $|000\rangle \rightarrow |0j0\rangle$ with $j \in \mathbb{N}$ from literature [114], while the remaining transitions energies were calculated based on the Dunham expansion for anharmonic coupled vibrational modes [115,116]. The latter is used to calculate transition frequencies $\tilde{\nu}(n_s, n_b, n_{as} \rightarrow n_{as}+1)$ and implies that the transition wavenumber will decrease by the anharmonicities x_{33}, x_{13} and x_{23} for every quantum of energy in an anharmonically coupled mode. Within this expansion, n_s quanta of excitation energy are in the symmetric stretching, n_b quanta in the bending and n_{as} quanta of energy in the asymmetric stretching mode according to [115]

$$\tilde{\nu}(n_s, n_b, n_{as} \rightarrow n_{as}+1) = \tilde{\nu}_0 + 2\,x_{33}\ (n_{as}+1) + x_{13}\ \left(n_s + \frac{1}{2}\right) + x_{23}\ \left(n_b + \frac{1}{2}\right). \tag{4.2}$$

Here, $\tilde{\nu}_0$ denotes the harmonic frequency of the investigated vibrational mode, x_{ij} an off-diagonal anharmonic coupling of modes i, j and x_{ii} a diagonal anharmonicity of mode i. The harmonic frequency of the $\nu_{as}(CO_2)$ of $\tilde{\nu}_0 = 2383\ cm^{-1}$, diagonal anharmonicity of $x_{33} = $ -13.0 cm^{-1}, the off-diagonal anharmonicities of $x_{13} = $ -19.1 cm^{-1} and $x_{23} = $ -12.5 cm^{-1} are taken from Allen et al. [116]. With them, the $\nu_{as}(CO_2)$ fundamental frequency is calculated to be equal to $\tilde{\nu}_{as} = 2343\ cm^{-1}$ as observed experimentally.

Now, the vibrational manifold of CO_2, as shown in figure 4.4, is addressed more in

detail. The quantum numbers correspond to $|\nu_s\ \nu_b\ \nu_{as}\rangle$. Of particular interest are the ground-state $|000\rangle$, the first excited state of the asymmetric stretching vibration $|001\rangle$ and its second excited state $|002\rangle$, since these states are investigated within the pump-probe experiment and thus, within the scope of this work. Moreover, the degenerated bending mode $|010\rangle$ is of particular interest as well, although it absorbs at a wavenumber of around 667 cm^{-1} located in the crowded fingerprint region. At room temperature, $|010\rangle$ is still populated to around 4 % according to a Boltzmann distribution (see eq. (2.28)). Nevertheless, it can couple anharmonically with the asymmetric stretching vibration resulting in a combination tone, i. e. $|011\rangle$, which causes a shift in wavenumber of 22 cm^{-1}. The temperature-dependent line width and asymmetric shape of the observed absorption band in the stationary spectra is then achieved by the rising population of the combination tone $|011\rangle$ and more, such as $|021\rangle$, $|031\rangle$ and $|041\rangle$ (see figure 4.4).

To confirm this statement, simulations of the absorption spectra at the investigated thermodynamic conditions were performed on the basis of the Kubo-Anderson stochastic theory [80, 81] (see sections 2.3, 5). Therefore, it was assumed that the transition matrix elements are identical so that the line shape for all transitions depicted in figure 4.4 are equal and described by the fit parameters Δ and τ_c. The transition from the ground-state to the first excited state of the asymmetric stretching vibration of $^{13}CO_2$ was considered as well. For each vibrational mode i and the investigated thermodynamic conditions within the scope of this work, the population $p_i(T)$ was calculated according to a Boltzmann distribution

$$p_i(T) = \frac{g \cdot \exp\left(-(h\ c\ \tilde{\nu}_i\ n)/(k_B\ T)\right)}{\sum_i \exp\left(-(h\ c\ \tilde{\nu}_i\ n)/(k_B\ T)\right)}. \tag{4.3}$$

Here, g is the degeneracy factor of a mode, h the Planck's constant, c the speed of light, $\tilde{\nu}$ the transition frequency, n the number of quanta in a mode, k_B the Boltzmann constant and T the temperature. Following, the Fourier transform[5] of eq. (2.49) is calculated over a transform length of $N = 2^{11}$ integers and the complete spectrum $S_{sim}(t, T)$ at a given temperature T is then

$$S_{sim}(t,T) = \sum_i \mathrm{Re}\left(\int_0^N \exp\left[-\Delta^2(T)\tau_c(T)\left(t - \tau_c(T)\left(1 - e^{-t/\tau_c(T)}\right)\right)\right] e^{-\mathrm{i}\tilde{\nu}t}\mathrm{d}t\right) \cdot p_i(T), \tag{4.4}$$

based on equations (2.46) and (2.49). Each simulated spectrum is individually normal-

[5]Here, a discrete Fourier transform of $\phi(t)$ (eq. (2.49)) is calculated by using a fast Fourier transform algorithm implemented in MATLAB. The length is set to $N = 2^{11}$ integers.

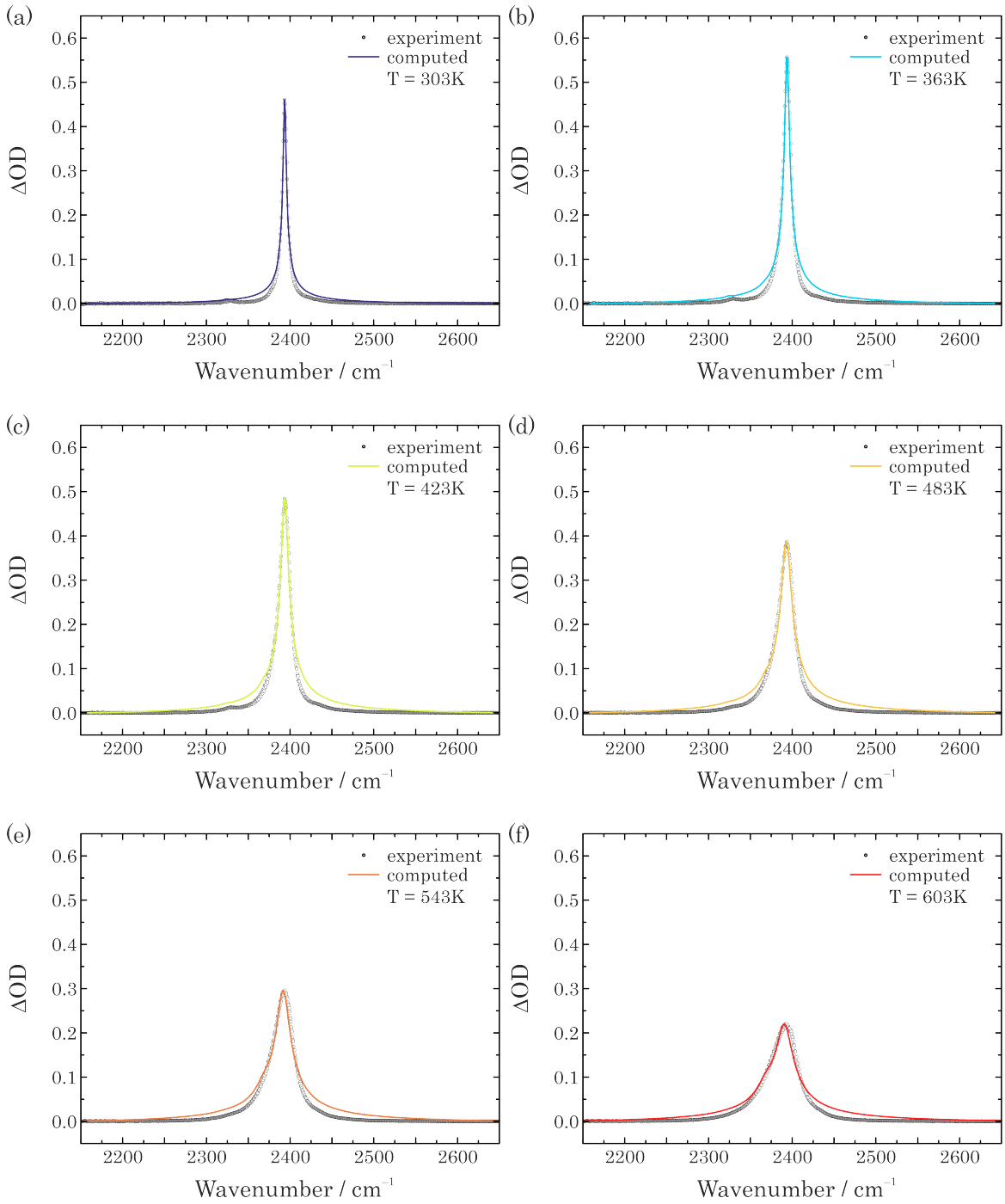

Figure 4.5: Computed (eq. (4.4)) as well as experimentally observed temperature-dependent absorption spectra of CO_2 at (a) 303 K, (b) 363 K, (c) 423 K, (d) 483 K, (e) 543 K and (f) 603 K. Experimental data are highlighted by circles, while computed spectra are shown by colored lines.

ized to the maximum of the experimentally observed absorption spectrum. Exemplary results of computed spectra are shown in figure 4.5 and are highlighted by colored solid lines. Based on the assumptions that were made for the simulation, the agreement is quite good. It can be concluded that the asymmetry is due to the anharmonic coupling of the asymmetric stretching with the degenerated bending vibration being still thermally populated at room temperature. Further information can be gained from the fit parameters Δ and τ_c and their arithmetic product α (see eq (2.50)) with the speed of light in vacuum c listed in table 4.1.

Table 4.1: Temperature-dependent fit parameters Δ and τ_c as well as the arithmetic product of α and the speed of light in vacuum c used in the computation of the temperature-dependent stationary absorption spectra of carbon dioxide dissolved in H_2O.

$\mathbf{T}$ / **K**	$\boldsymbol{\Delta}$ / $\mathbf{cm^{-1}}$	$\boldsymbol{\tau_c}$ / **ps**	$\boldsymbol{\alpha \cdot c}$
303	39.49	0.242	0.286
333	47.13	0.211	0.298
363	55.71	0.187	0.312
393	65.72	0.171	0.337
423	76.43	0.153	0.351
453	87.30	0.144	0.377
483	94.55	0.139	0.394
513	106.7	0.129	0.413
543	114.8	0.125	0.430
573	125.7	0.115	0.433
603	135.0	0.111	0.449

From that table, it is obvious that with rising temperature the amplitude of frequency fluctuations (Δ) increases along with a decrease of the correlation time (τ_c). The former rises more than threefold while the correlation time decreases twofold. As introduced in section 2.3, the arithmetic product of Δ and τ_c (α) with the speed of light in vacuum c has two limits, either $\alpha \to \infty$ and $\tau_c \to \infty$ resulting in a Gaussian line shape or $\alpha \to 0$, which leads to a Lorentzian line shape. Within the investigated temperature range, α is without exception less than unity, and increases with rising temperature, i. e. each transition line shape (Lorentzian like) is a superposition of the individual considered transitions shown in the vibrational energy level diagram in figure 4.4. In the following, these results are compared to those of the temperature- and time-dependent MIR pump-probe spectra.

4.1.2 Temperature-dependent time-resolved mid-infrared pump-probe spectra of carbon dioxide in H_2O

Time-resolved pump-probe spectra of carbon dioxide dissolved in H_2O were recorded under isobaric heating at 500 bar from 303 K up to 603 K using the high-temperature high-pressure cell presented in section 3.2. As mentioned before, the ν_{as} band of dissolved CO_2 absorbs in the same spectral range as that of gaseous carbon dioxide does. Therefore, in time-resolved pump-probe measurements, transitions belonging to the rotational fine structure of atmospheric carbon dioxide were absorbed from the pump pulses in the transmitted pump-pulse spectrum. The interaction generates a frequency comb. In the time domain, this frequency comb leads to a pulse train repeatedly interacting with the sample. The mean distance of two neighboring lines of the rotational fine structure is $\Delta\tilde{\nu} = 1.56$ cm^{-1}, which corresponds to a temporal delay of around 21.4 ps. Those reiterating interactions can be observed within the transient spectra and kinetic traces and are shown exemplarily for room temperature in a kinetic trace of the maximum of the transient absorption signal at 2317 cm^{-1} in figure 4.6.

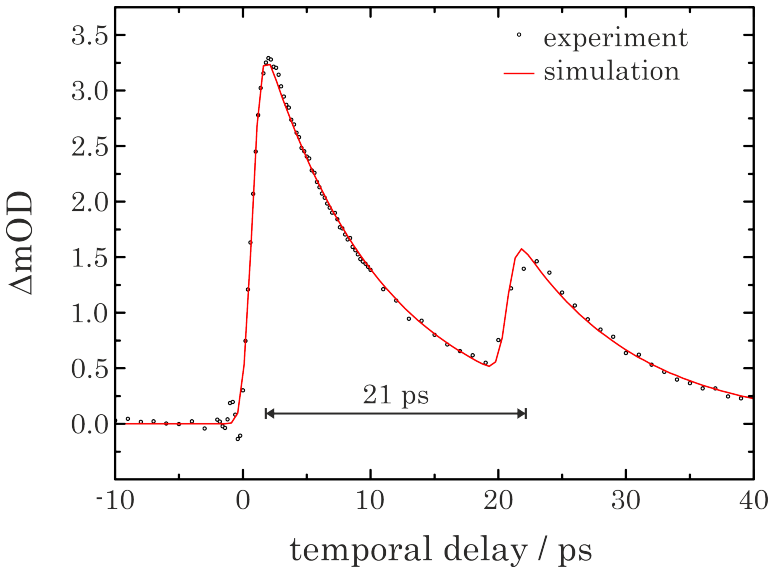

Figure 4.6: Kinetic trace at a frequency corresponding to the maximum of the transient absorption of carbon dioxide dissolved in H_2O at room temperature. Two interactions of the pump pulse with CO_2 are recognizable within the depicted temporal range. Experimental data points are highlighted by circles, a fit (see eq. (4.5)) considering both interactions with a solid red line.

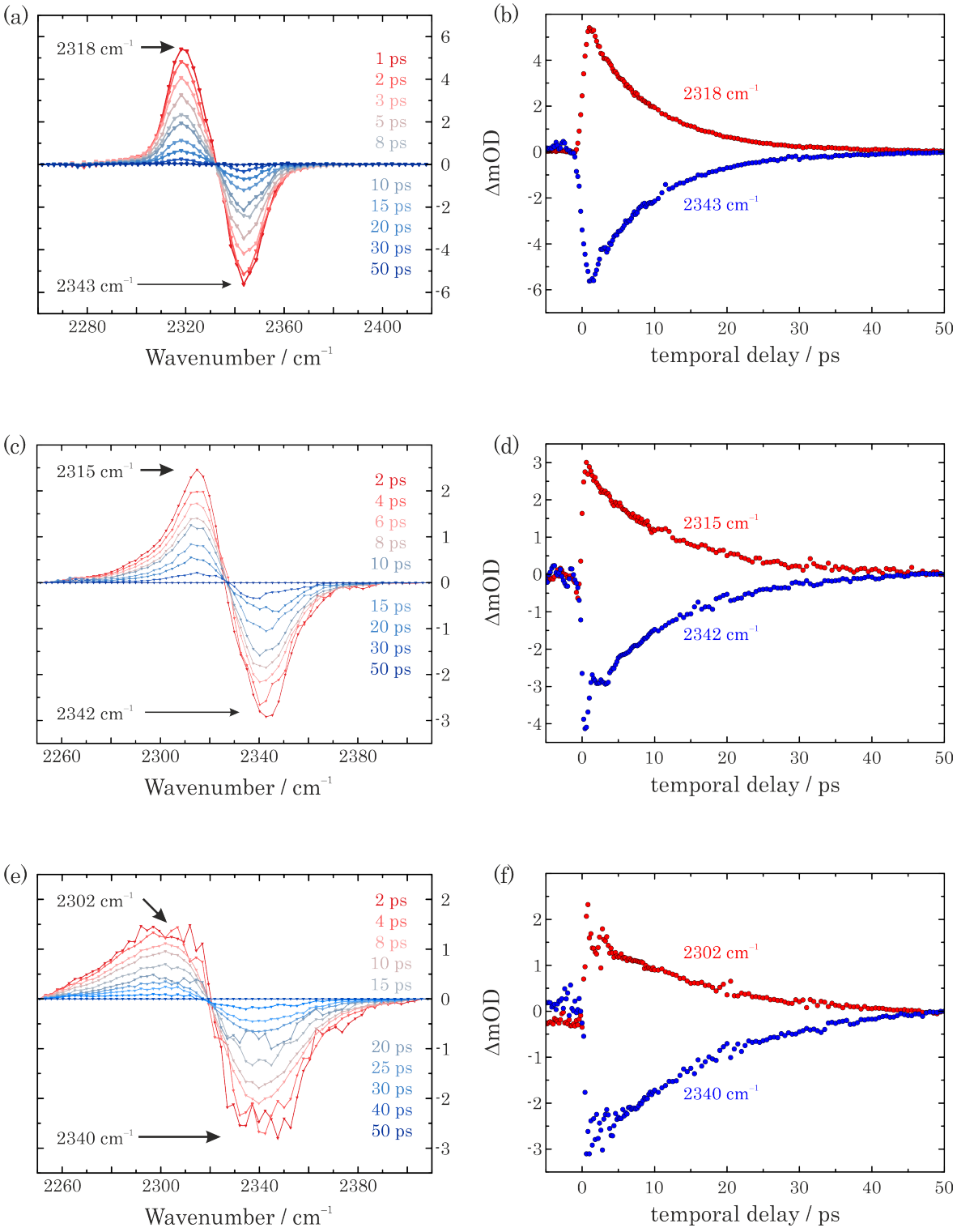

Figure 4.7: Transient spectra of carbon dioxide dissolved in H_2O at (a) 303 K, (c) 453 K and (e) 603 K and different delay times (delay increasing from red to blue). Kinetic traces of the TA (red) and the GB/SE (blue) (b, d, f) are displayed for the aforementioned temperatures.

A temporal distance between the maxima within the kinetic traces of around 21 ps is recognizable, which was determined by a fit of the experimental data considering multiple pulses interacting with the sample within 40 ps. As a fit function a convolution of a bi-exponential decay function with a Gaussian according to

$$f(t) = \sum_{i=1}^{2} A_i \exp\left(-\frac{t-t_0}{\Delta t}\right)\left[1 + \mathrm{erf}\left(\frac{2\sqrt{\ln(2)}(t-t_0)}{2\Delta t} - \frac{2\Delta t}{4\sqrt{\ln(2)}\tau_i}\right)\right] \tag{4.5}$$

was used, reflecting the convolution of the instrument response function of the pump-probe spectrometer with the response from the aqueous CO_2 solution. Here, A_i denotes an amplitude, t_0 time zero, t the temporal delay, $(2\Delta t)$ the full-width at half-maximum duration of the cross-correlation of the experiment and τ_i the decay time.

To avoid the multiple interactions of remaining atmospheric CO_2 with the pump pulse, a perfect purging with pure nitrogen of the entirely experimental setup is necessary. The data presented in the following were recorded under these conditions. In figure 4.7, transient spectra and kinetic traces at 303 K (a, b), 453 K (c, d) and 603 K (e, f) are shown. The second excitation after 21 ps is almost completely suppressed within the signal-to-noise ratio of the recorded transients.

All recorded transient spectra consist of two signal contributions, which experience an increasing asymmetric broadening with rising temperature. The widths of the signal contributions increase as well, which is in accordance with the stationary absorption spectra (section 4.1.1). As described in section 2.3, the response with negative ΔOD can be attributed to the ground-state bleach (GB) as well as the stimulated emission (SE). The red-shifted signal with positive ΔOD is ascribed to the transient absorption (TA) from the first to the second excited state of the asymmetric stretching mode in various combination tones. Within the recorded temporal delay of 50 ps, the TA and the GB/SE decayed to zero ΔOD considering the achieved signal-to-noise ratio. This holds for all investigated thermodynamic conditions and implies that no persistent bleach is observable. An isosbestic point[6] occurs, recognizable by the intersection of all transients within the spectrum, because the shape of the transient spectra does not evolve with rising temporal delay. The spectral positions of the TA, the GB/SE and the isosbestic point as well as the anharmonicity Δ_{11} , determined from the frequency difference between the maximum of the TA and the minimum of the GB/SE, are summarized in table 4.2 for all investigated temperatures.

[6] An isosbestic point occurs at a specific frequency, at which the absorption and hence, the extinction coefficient does not change at all delays [117].

Table 4.2: Spectral positions of transient absorption, ground-state bleach / stimulated emission as well as isosbestic point of the excited asymmetric stretching vibration ν_{as} of the aqueous carbon dioxide solution for each investigated thermodynamic point. Additionally, the anharmonicity Δ_{11} is given.

T / K	$\tilde{\nu}_{TA}$ / $\mathbf{cm^{-1}}$	$\tilde{\nu}_{GB}$ / $\mathbf{cm^{-1}}$	$\tilde{\nu}_{isos}$ / $\mathbf{cm^{-1}}$	Δ_{11} / $\mathbf{cm^{-1}}$
303	2318	2343	2332	25
333	2318	2343	2330	25
363	2317	2343	2330	26
393	2316	2342	2329	26
423	2315	2342	2328	27
453	2315	2342	2327	27
483	2313	2341	2325	28
513	2311	2341	2323	30
543	2308	2341	2323	33
573	2307	2340	2322	33
603	2302	2340	2319	38

From table 4.2, it can be observed that with rising temperature the anharmonicity Δ_{11} increases as well. The reason for this becomes clear when the temperature-induced spectral shift δ of the GB/SE and the TA is considered. For the former, it is $\delta = (1.12 \pm 0.14) \cdot 10^{-2}\ \mathrm{cm^{-1}K^{-1}}$, for the latter $\delta = (4.66 \pm 0.28) \cdot 10^{-2}\ \mathrm{cm^{-1}K^{-1}}$. The temperature-induced spectral shift of the TA is thus about four times higher than that of the GB/SE resulting in an increasing anharmonicity Δ_{11}.

In the following, the kinetic traces of the GB/SE and the TA signal contributions of the transient spectra are investigated in more detail to determine the lifetime τ_1 of the excited state as well as the ground-state recovery lifetime τ_0. Three exemplaric kinetic traces are shown in figures 4.7 (b, d, f). Here, it is noteworthy that the kinetic traces behave like mirror images for each investigated temperature. This indicates that τ_0 and τ_1 are of the same order of magnitude. Furthermore, the kinetic traces seem to evolve with mono-exponential decay functions. To verify this observation, the temporal-dependent ΔOD at the wavenumber of maximum transient absorption (see figure 4.8 (a)) or respectively ground-state bleach (see figure 4.8 (b)) are displayed in semi-logarithmic plots for exemplaric thermodynamic conditions. For visual clarity, the traces are shifted vertically.

By inspecting the traces carefully, it is observable that the signal contributions decay slower with rising temperature. A linear regression analysis is used to determine the lifetimes τ_1 and τ_0. The experimental data for each temperature were modeled starting

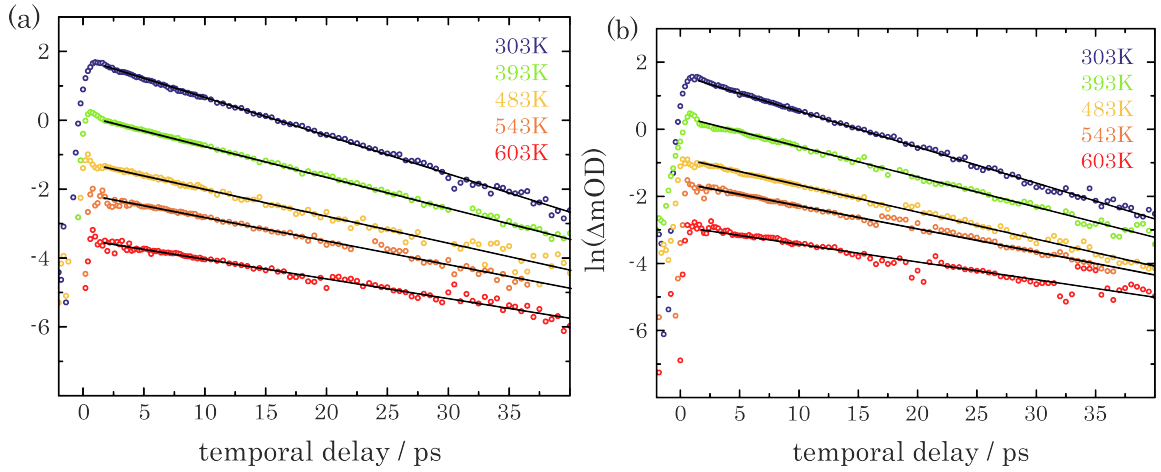

Figure 4.8: Temporal dependence of ΔOD at the wavenumber of maximum TA (a) as well as of maximum GB/SE (b) shown in semi-logarithmic plots for five temperatures at a pressure of 500 bar. The results of linear regression are displayed as solid lines starting at delay times at which contributions from the coherent artifact can be neglected. The traces are shifted vertically for visual clarity.

at delay times where the influence of the coherent artifact[7] can be neglected, i. e. above 500 fs, resulting in linear fits with slope $m_{\mathrm{fit}}(T)$ and intercept $b_{\mathrm{fit}}(T)$. Considering the semi-logarithmic way of presentation, the inverse of the slopes corresponds to the requested lifetimes being summarized in table 4.3.

Table 4.3: Lifetime τ_1 of the excited state as well as the ground-state recovery lifetime τ_0 for each investigated thermodynamic condition at 500 bar of carbon dioxide dissolved in H_2O.

T / K	$\boldsymbol{\tau_1}$ **/ ps**	$\boldsymbol{\tau_0}$ **/ ps**
303	9.0 ± 0.1	9.0 ± 0.1
333	9.3 ± 0.2	9.9 ± 0.2
363	9.9 ± 0.1	10.1 ± 0.1
393	11.0 ± 0.1	11.2 ± 0.2
423	11.2 ± 0.1	11.6 ± 0.2
453	11.6 ± 0.2	11.8 ± 0.2
483	12.5 ± 0.2	12.8 ± 0.2
513	14.0 ± 0.4	14.6 ± 0.4
543	14.9 ± 0.5	15.2 ± 0.4
573	16.5 ± 0.5	15.9 ± 0.5
603	17.1 ± 0.6	17.5 ± 0.6

[7] A coherent artifact is a coherent perturbed free induction decay (PFID) effect, which contributes solely at negative delay times as well as during the temporal overlap of pump and probe pulses [118].

The excited state lifetime τ_1 and the ground-state recovery lifetime τ_0 at 303 K and 500 bar are in accordance with those reported by Hamm et al. as *[...] somewhat slower than 10 ps* [49]. No further references were found.

Within the investigated thermodynamic range, the experimentally observed lifetimes τ_0 and τ_1 agree within 98.1 %, but are not equal. However, both increase by a factor of two over the entire temperature range at 500 bar.

To understand the increasing lifetimes with rising temperature, the underlying vibrational energy redistribution (VER) has to be considered. In the literature [23, 24, 86, 119], two competing VER mechanisms of polyatomic molecules in solutions are described, namely a direct intermolecular vibrational energy transfer (VET) from the solute to the solvent and a solvent-assisted sequential intramolecular vibrational redistribution (s-IVR). In the following, both competing mechanisms are discussed in the context of the investigated CO_2 dissolved in H_2O. On that account, relaxation rate constants are considered, which are $k_0 = 1/\tau_0$ and $k_1 = 1/\tau_1$.

If the underlying vibrational energy redistribution is a VET, the solvent is required to provide energy-accepting states that are fully resonant with the investigated asymmetric stretching vibration of carbon dioxide. Such acceptor states can originate from the combination tone of the bending mode and the libration of H_2O, i. e. $(\nu_b+\nu_L)$, since this mode appears in the stationary absorption spectra as a quasi-continuous base under the ν_{as} band of the CO_2 over the investigated thermodynamic range (see figure 4.3 (b)). In a pertubative treatment of the VET, the relaxation rate constant can be expressed by Fermi's golden rule. As introduced in section 2.4, Fermi's golden rule describes a transition rate of a perturbed discrete initial state to a final one, which is nestled into a continuum of bath states. According to eq. (2.71), the relaxation rate constant k is proportional to the matrix element $|\mathbf{H}'|^2$ and the spectral overlap *S(T)*. The latter is computed according to eq. (2.70) based on the recorded temperature-dependent stationary absorption spectra (fig 4.3 (a)) and decreases with rising temperature due to the diminishing overlap between the solute's and the solvent's mode. At the same time, the relaxation rate constants k_0 and k_1 decrease as well. Graphs of the relaxation rate constant k_0 and k_1 each as a function of the calculated spectral overlap are presented in figure 4.9 (a), (b).

Here, linear fits represent the data reasonably within the error limits. However, the lines of best fit intersect the ordinate with an offset of $k_0' = (0.047 \pm 0.003)\ \mathrm{ps}^{-1}$ or respectively $k_1' = (0.046 \pm 0.003)\ \mathrm{ps}^{-1}$. This means that the vibrational energy redistribution of the investigated molecular dissolved CO_2 in H_2O cannot be described with

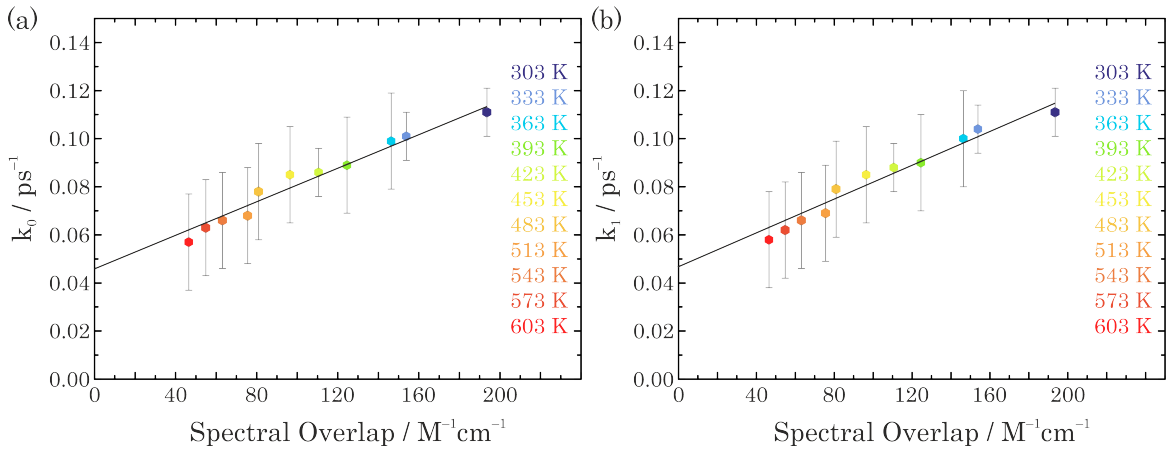

Figure 4.9: Plot of the relaxation rate constant of (a) the ground state k_0 and of (b) excited state k_1 as a function of the spectral overlap of the solute's ν_{as} with the solvent's $(\nu_b + \nu_L)$ absorption bands. Filled hexagons indicate temperatures from 303 K (blue) to 603 K (red).

Fermi's golden rule, because further vibrational modes are involved in the underlying relaxation mechanism. To investigate the offset of k_0 and k_1 for a spectral overlap of $S = 0$, it is assumed that there is a constant additive contribution to the VER mechanism. Hence, a solvent-assisted sequential IVR is postulated.

If so, the vibrational energy in the solute's ν_{as} mode is redistributed into anharmonically coupled lower frequency modes of the carbon dioxide and the solvent H_2O [24,86]. For that purpose, the bending mode ν_b of CO_2 is an eligible mode, which is in this context assigned as the intermediate state in a solvent-assisted sequential IVR. It is already known from the analysis of the absorption spectra (see section 4.1.1), that the transitions $|0i0\rangle \rightarrow |0i1\rangle$ $(i \in \mathbb{N})$ are present. Furthermore, the bending mode ($|010\rangle$, figure 4.10) is resonant to the solvent's libration ν_L at room temperature, which in turn can be assigned as the solvent mode acting as the energy accepting states. According to that, the solvent-assisted sequential IVR mechanism can be described as

$$|\nu_{as}, 0\rangle \xrightarrow{k^{\ddagger}} |\nu_b, 0\rangle + |0, \nu_b\rangle \xrightarrow{k} |0, \nu_L\rangle + |0, \nu_b\rangle \xrightarrow{1/\tau_{H_2O}} |0, 0\rangle + \Delta E. \tag{4.6}$$

Here, $|\nu, 0\rangle$ denotes the quanta of excitation energy in the solute's, $|0, \nu\rangle$ those in the solvent's mode and ΔE the heating of the solvent. This sequence, shown in figure 4.10, uses the time constant $k^{\ddagger}$ describing the relaxation from the initially excited ν_{as} mode ($|001\rangle$) to the intermediate mode ν_b ($|010\rangle$) of carbon dioxide. The energy difference can be overcome by the excitation of the bending mode of H_2O. The time constant k belongs to the relaxation from the intermediate mode $|010\rangle$ to the solvent's libration

ν_L, while the bending mode of H_2O is still excited. Subsequently, the excess energy is redistributed within the solvent within $1/\tau_{H_2O}$ [120]. As mentioned above, the bending mode of the solvent is involved in the s-IVR mechanism and shows no temperature-dependent spectral shift, since it is a pure intramolecular mode. The excitation of this mode can explain the offset of k_0 and k_1 for a spectral overlap of $S = 0$ observed in figures 4.9 (a), (b). The complete sequence is displayed in a scheme of the vibrational energy manifold of CO_2 (right) and H_2O (middle and left) for the limiting cases at about 300 K and 600 K as shown in figure 4.10. The modes of solute and solvent that are involved in the mechanism are highlighted in blue.

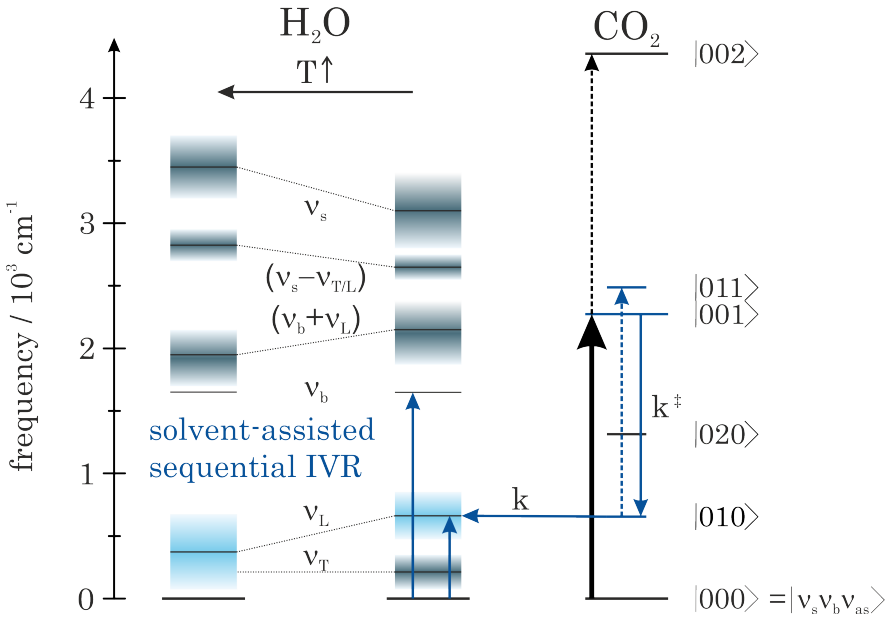

Figure 4.10: Energy level scheme of carbon dioxide (right side) and H_2O (middle, 300 K and left side, 600 K). The different modes are labeled as $|\nu_s\ \nu_b\ \nu_{as}\rangle$ for CO_2. Some modes of the solvent H_2O are shown as boxes to illustrate the widths of the corresponding absorption bands. A solvent-assisted sequential intramolecular vibrational relaxation mechanism is highlighted by blue arrows.

As mentioned before, the transient absorption and the ground-state bleach can be described by a mono-exponential decay function. To observe a single exponential relaxation in the postulated sequence, the relaxation rate of the transition from the initially excited state $|001\rangle$ into the bending mode $|010\rangle$ must be much longer than the relaxation rate of the intermolecular transition from the intermediate state $|010\rangle$ of carbon dioxide to the resonant libration of H_2O, i. e. $k^{\ddagger} >> k$. This means that a population of the initial state cannot evolve, i. e. its occurrence in the vibrational energy redistribution mechanism is not relevant for the kinetics. Indeed, it is reported in literature that an intramolecular vibrational redistribution is fast compared to the

VET time scale [121–123]. In addition, the redistribution of the vibrational energy in the libration of H_2O is much shorter than the time-resolution of the experimental setup. It is known that once the vibrational energy is dissipated from the solute to the solvent's mode, it is delocalized over many water molecules on a time scale of around $\tau_{H_2O} \approx 50$ fs [120]. Considering those, the solvent-assisted sequential IVR mechanism presented above can be reduced to a kinetic model, which is described by a mono-exponential decay of the TA and the GB/SE. This model results in the observed relaxation rate constants k_1 and k_0, which correspond to the inverse of the relaxation rate constant k in the presented sequence.

In the following, the temperature dependence of the correlation time τ_c received from the simulations of the absorption spectra based on the Kubo-Anderson general stochastic theory is discussed in the following. In contrast to the increasing lifetime with rising temperature ascertained from the pump probe spectra, the correlation time τ_c (see table 4.1) decreases within the investigated temperature range. Assuming that the inverse of the correlation time is a rate constant for a relaxation process within the solute, an Arrhenius analysis can be conducted as shown in figure 4.11.

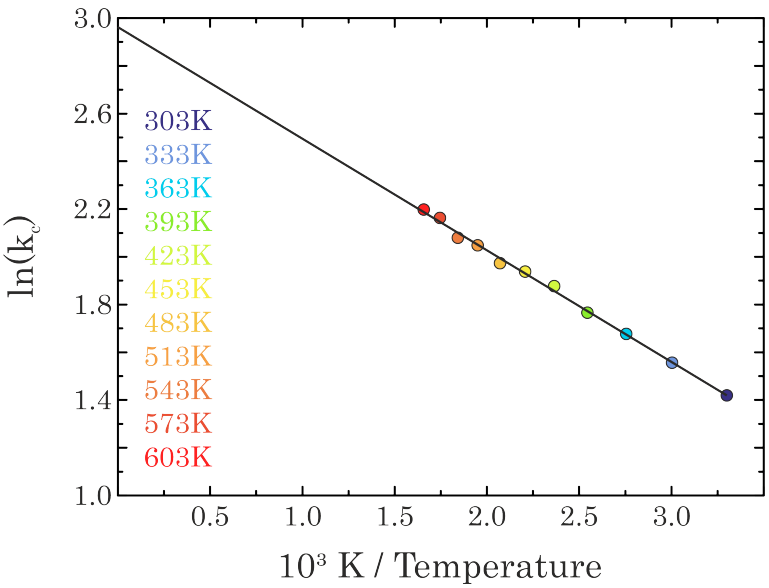

Figure 4.11: Arrhenius analysis of the inverse of the correlation time (k_c) determined from Kubo-Anderson general stochastic theory (see section 2.3) as a function of the inverse temperature.

For this purpose, the natural logarithm of the rate constant $k_c = 1/\tau_c$ is plotted as a function of the inverse temperature according to

$$\ln(k_c) = \ln(A) - \frac{E_A}{R}\frac{1}{T} \tag{4.7}$$

with an attempt frequency A, an activation energy E_A and the universal gas constant R. According to this, a linear correlation is expected as shown in figure 4.11. The slope is consistent with an activation energy of $E_A = 3.9\ \mathrm{kJmol^{-1}}$, the intercept corresponds to an attempt frequency of around $19.5\ \mathrm{ps^{-1}}$, which in turn is in accordance with a vibrational wavenumber of about $650\ \mathrm{cm^{-1}}$. The error margin is estimated to be about 25 %. The agreement between that wavenumber of $650\ \mathrm{cm^{-1}}$ and the degenerated bending motion of the CO_2 is quite good, which leads to the conclusion that the correlation time represents the lifetime of the intermediate state in the solvent-assisted sequential IVR mechanism.

4.1.3 Conclusion I

This chapter served as a presentation of the temperature-dependent stationary absorption as well as the pump-probe spectra of carbon dioxide dissolved in H_2O. Within the former, the increasing asymmetric shape of the ν_{as} absorption band of CO_2 was explained by overlapping Lorentzian shaped bands, which were attributed to transitions from the bending mode $|0i0\rangle$ to the combination tone $|0i1\rangle$ with i quanta of energy in the bending mode ν_b of carbon dioxide. Based on this, the absorption spectra were computed by means of the Kubo-Anderson general stochastic theory under the assumption that the transition matrix elements are identical. The agreement was quite good.

The pump probe spectra feature two signal contributions within the investigated temperature range at a pressure of 500 bar, which were attributed to the transient absorption, the ground-state bleach and the stimulated emission. With rising temperature, a broadening of the spectra was observed as well. The kinetic traces evolved with mono-exponential decay functions and no persistent bleach was observed. The lifetimes, obtained from an analysis of the kinetic traces of the maxima of the TA and the GB/SE, rise almost twofold from 9.0 ps at 303 K up to 17.1 ps at 603 K. The relaxation rate constants (the inverse of the lifetimes) were firstly attributed to an intermolecular energy transfer from the solute's asymmetric stretching mode to the resonant solvent' combination tone $(\nu_b + \nu_L)$. In a pertubative treatment of the VET, the relaxation rate constant can be expressed by Fermi's golden rule. This implies that there is a correlation between the relaxation rate constant and the spectral overlap

between the involved solute and solvent modes expressed by the interaction matrix element. Indeed, a plot of the k as a function of the spectral overlap S showed a linear correlation. However, the lines of best fit intersected the ordinate with an offset resulting in the assumption that a pure VET mechanism can be excluded. Secondly, a solvent-assisted sequential IVR (s-IVR) mechanism was considered. Within this mechanism, the vibrational excess energy in the solute's mode is redistributed into anharmonically coupled lower frequency modes of the CO_2 and the H_2O. It was assumed that the s-IVR is described by an intramolecular vibrational redistribution from the initially excited asymmetric stretching vibration of CO_2 into its bending mode with a relaxation rate constant $k^{\ddagger}$. Subsequently, a VET from the bending mode to the solvent's libration ν_L with a relaxation rate constant k followed. The energy mismatch can be overcome by the excitation of the solvent's bending mode, which is a purely intramolecular mode, and thus temperature-independent. The excitation of this mode can explain the observed offset of k_0 and k_1 for $S = 0$. The excess energy in the solvent is then internally redistributed within around 50 fs. Due to the fact that an IVR is fast compared to the VET time scale, only the relaxation rate constants of the VET were observed from the pump-probe spectra. However, under the assumption that the correlation time obtained from the simulations of the absorption spectra is a rate constant for a relaxation process, it was assigned to the relaxation rate constant of the initially excited asymmetric stretching vibration of CO_2.

4.2 Infrared spectroscopy of cyanate anions in H_2O

In this chapter, the cyanate anion, with its stretching vibration ν_3 is the vibrational probe of interest. Three different isotopologues of the OCN^- anion (OCN^-, $O^{13}CN^-$, $O^{13}C^{15}N^-$) in aqueous solution are investigated with stationary FTIR and pump-probe spectroscopy at various thermodynamic conditions. The results are discussed in the context of Fermi's golden rule and the isotope effect on the relaxation rate constants is studied.

4.2.1 Temperature-dependent stationary absorption spectra

The three isotopologues of the cyanate anion were studied under isobaric heating at 500 bar from 303 K up to 373 K in intervals of 10 K. The corresponding thermodynamic conditions are depicted by colored, filled circles in the phase diagram of pure water in figure 4.12.

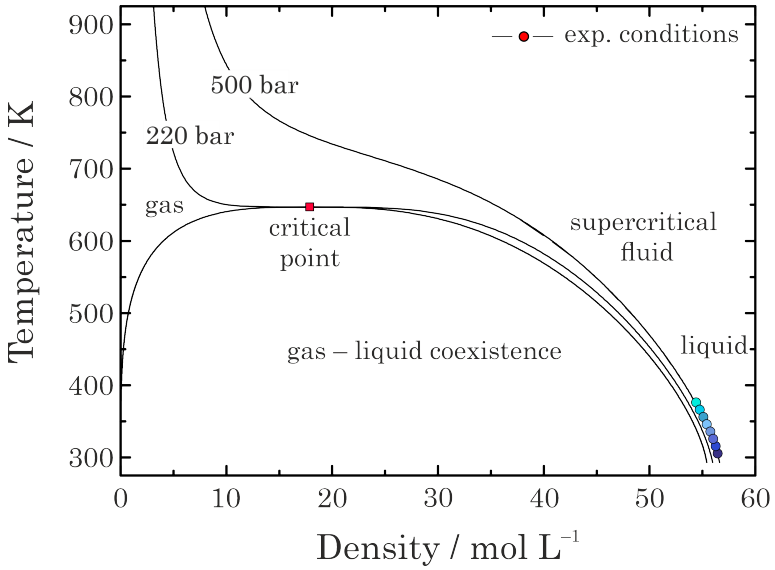

Figure 4.12: Phase diagram of pure water. Thermodynamic conditions studied for the different cyanate solutions are highlighted by filled circles (blue (303 K) to cyan (373 K) in intervals of 10 K). The critical point of water is highlighted by a filled square and described by a pressure of $p_{crit} = 221$ bar and a temperature of $T_{crit} = 647$ K.

In contrast to former investigations of other triatomic pseudohalide anions [28, 32], it was not possible to cover the supercritical phase, because the solution of cyanate anion in H_2O decomposes with rising temperature according to the following reaction

$$OCN^-_{(aq)} + 2\,H_2O \longrightarrow CO_{2(g)} + NH_{3(g)} + OH^-_{(aq)}. \tag{4.8}$$

Nevertheless, a change of the density in the range of 56.45 mol/l to 54.41 mol/l with increasing temperature is discernible.

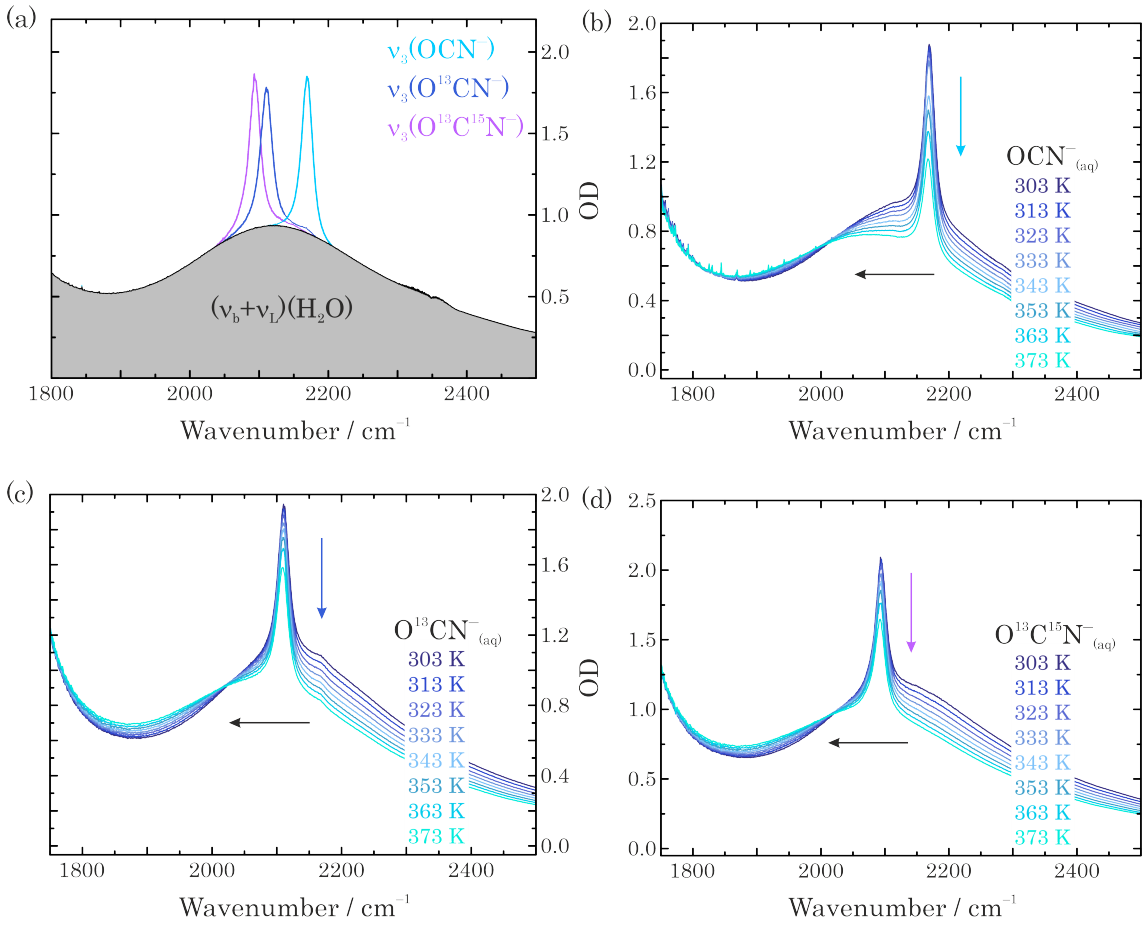

Figure 4.13: (a) Stationary absorption spectra of the investigated aqueous cyanate solutions at 303 K and 500 bar. In gray, the absorption band $(\nu_b + \nu_L)$ of the solvent H_2O is shown. The absorption bands of the ν_3 mode are colored cyan for the OCN^-, blue for the $O^{13}CN^-$ and purple for the $O^{13}C^{15}N^-$ anion.
(b)-(d) Temperature-dependent stationary absorption spectra of (b) OCN^-, (c) $O^{13}CN^-$ and (d) $O^{13}C^{15}N^-$ in H_2O under isobaric heating at 500 bar.

In figure 4.13 (a), absorption spectra of the studied aqueous cyanate solutions at a temperature of 303 K and a pressure of 500 bar are shown. Within a spectral range from 1800 cm^{-1} to 2500 cm^{-1} four absorption bands are observable. A broad absorption band (gray filled band) covers the complete depicted spectral range and can be assigned to the combined excitation of the bending mode and the librations of the solvent water, i. e. $(\nu_b + \nu_L)(H_2O)$. Within the same spectral range, three narrow absorption bands are located. They can be attributed to the stretching vibrations ν_3 of the different

isotopologues of the cyanate anion. The spectral position of the absorption bands are in consistence with literature [24, 124] and given in table 4.4.

Table 4.4: Molecular masses and center frequencies of three cyanate isotopologues in aqueous solution from the literature (columns two and three from left). The fourth column gives center frequencies obtained in this work at 303 K and 500 bar. The average of the full-width at half-maximum ($\langle \Delta\nu_{FWHM} \rangle$) between 303 K and 373 K is listed in column five. (^{a} measured in aqueous solution [24]; ^{b} measured in KCl matrix [124])

Isotopologue	**molar mass / g/mol**	$\boldsymbol{\nu_3}$**(lit.) / cm^{-1}**	$\boldsymbol{\nu_3}$**(exp.) / cm^{-1}**	$\langle \boldsymbol{\Delta\nu}^{exp.}_{\mathbf{FWHM}} \rangle$ **/ cm^{-1}**
OCN^-	42.02	2168 ^{a}, 2181.8 ^{b}	2169.2 ± 0.2	18.5 ± 0.3
$O^{13}CN^-$	43.01	2124.2 ^{b}	2109.7 ± 0.2	19.7 ± 0.3
$O^{13}C^{15}N^-$	44.01	2106.8 ^{b}	2094.2 ± 0.2	19.0 ± 0.3

The absorption bands of the cyanate anions in solution can be described with a Lorentzian line shape. Within the error range, the full-width at half-maximum is almost temperature-independent for the individual anions, but it varies around 6 % between the different isotopologues. The mean value for each isotopologue is presented in column five of table 4.4.

Figures 4.13 (b)-(d) depict stationary absorption spectra of cyanate isotopologues dissolved in H_2O covering the temperature range from 303 K to 373 K. Clear temperature-dependent changes of the solute and solvent absorption bands can be observed, which are indicated by arrows. Firstly, the frequency of the combination tone ($\nu_b + \nu_L$) of H_2O experiences a bathochromic spectral shift with rising temperature (black horizontal arrows in (b)-(d)), which can be attributed to that of the librations ν_L to the solvent's combination tone ($\nu_b + \nu_L$). In turn, the spectrum of the combination tone is sensitive to changes in the hydrogen bonded network and thus, to changes in thermodynamic conditions [28, 125, 126]. Secondly, a decrease in optical density OD of the solute's absorption band is indicated for each cyanate isotopic combination by a colored vertical arrow in figures 4.13 (b)-(d). The decrease is mainly caused by decomposition of the cyanate isotopologues with rising temperature, but also by the diminishing density and solubility. At the same time, the spectral position of the solute's absorption bands vary only slightly. To confirm this observation, the spectral shift of the absorption band is determined as a function of temperature within the studied range. The experimentally determined spectrothermal coefficients of the spectral shift per temperature interval δ for all isotopologues are given in table 4.5. For comparison, the corresponding coefficient for a thiocyanate anion in aqueous solution is given as well [106].

Table 4.5: Spectrothermal coefficients δ for the investigated aqueous cyanate isotopologues and for an aqueous thiocyanate solution [106].

$\delta(\mathbf{OCN^-})$ / $\mathbf{cm^{-1}K^{-1}}$	$\delta(\mathbf{O^{13}CN^-})$ / $\mathbf{cm^{-1}K^{-1}}$	$\delta(\mathbf{O^{13}C^{15}N^-})$ / $\mathbf{cm^{-1}K^{-1}}$	$\delta(\mathbf{SCN^-})$ / $\mathbf{cm^{-1}K^{-1}}$
$(2.7 \pm 0.1) \cdot 10^{-2}$	$(1.4 \pm 0.1) \cdot 10^{-2}$	$(2.0 \pm 0.1) \cdot 10^{-2}$	$(1.5 \pm 0.1) \cdot 10^{-2}$

As can be seen, the coefficients of the temperature-dependent spectral shift of the stretching vibration ν_3 of the cyanate isotopologues and the thiocyanate (SCN^-) absorption bands are rather similar. For comparison, the corresponding coefficient of the solvent's combination tone ($\nu_b + \nu_L$) was calculated with data from the literature [113]. Inspecting a comparable temperature range, the coefficient $\delta((\nu_b + \nu_L)(H_2O))$ is obtained to be $\delta((\nu_b + \nu_L)(H_2O)) = (48.1 \pm 0.2) \cdot 10^{-2}\ cm^{-1}K^{-1}$, which is more than one order of magnitude larger than that for the anions.

4.2.2 Temperature-dependent time-resolved pump-probe spectra

Time-resolved pump-probe spectra were recorded in the same thermodynamic range as the absorption spectra in order to investigate the kinetics of vibrational energy relaxation. In figures 4.14 (a), (c), (e), transient spectra of the three cyanate isotopologues are depicted for a temperature of 333 K. Herein, a temporal interval is shown covering the earliest one without influence from the coherent artifact[8] up to delay times from that, for which all signal contributions have decayed to zero ΔOD within the achieved signal-to-noise ratio. All spectra show a ground-state bleach (GB)/stimulated emission (SE) at the frequency of the stretching vibration ν_3 and a corresponding red-shifted absorption (see section 2.3). Based on the red-shift of the transient absorption (TA) compared to the GB/SE signal, the vibrational anharmonicity Δ_{11} was determined. In case of the OCN^-, the GB/SE peaks at 2169 cm^{-1}, the TA at 2144 cm^{-1} resulting in an anharmonicity of Δ_{11} =25 cm^{-1} (see table 4.6 and figures 4.14 (a)+(b)). Those data are in accordance with those reported in the literature [26] for OCN^- in MeOH. In table 4.6, an overview about the spectral positions of the ground-state bleaches and of the transient absorption signals as well as vibrational anharmonicities for the investigated isotopologues at a temperature of 333 K and a pressure of 500 bar is given. Within the investigated temporal range of the transient spectra, isosbestic points were

[8] A coherent artifact is a coherent perturbed free induction decay (PFID) effect, which contributes at negative delay times, during the temporal overlap of pump and probe pulses as well as at earliest positive delay times [118].

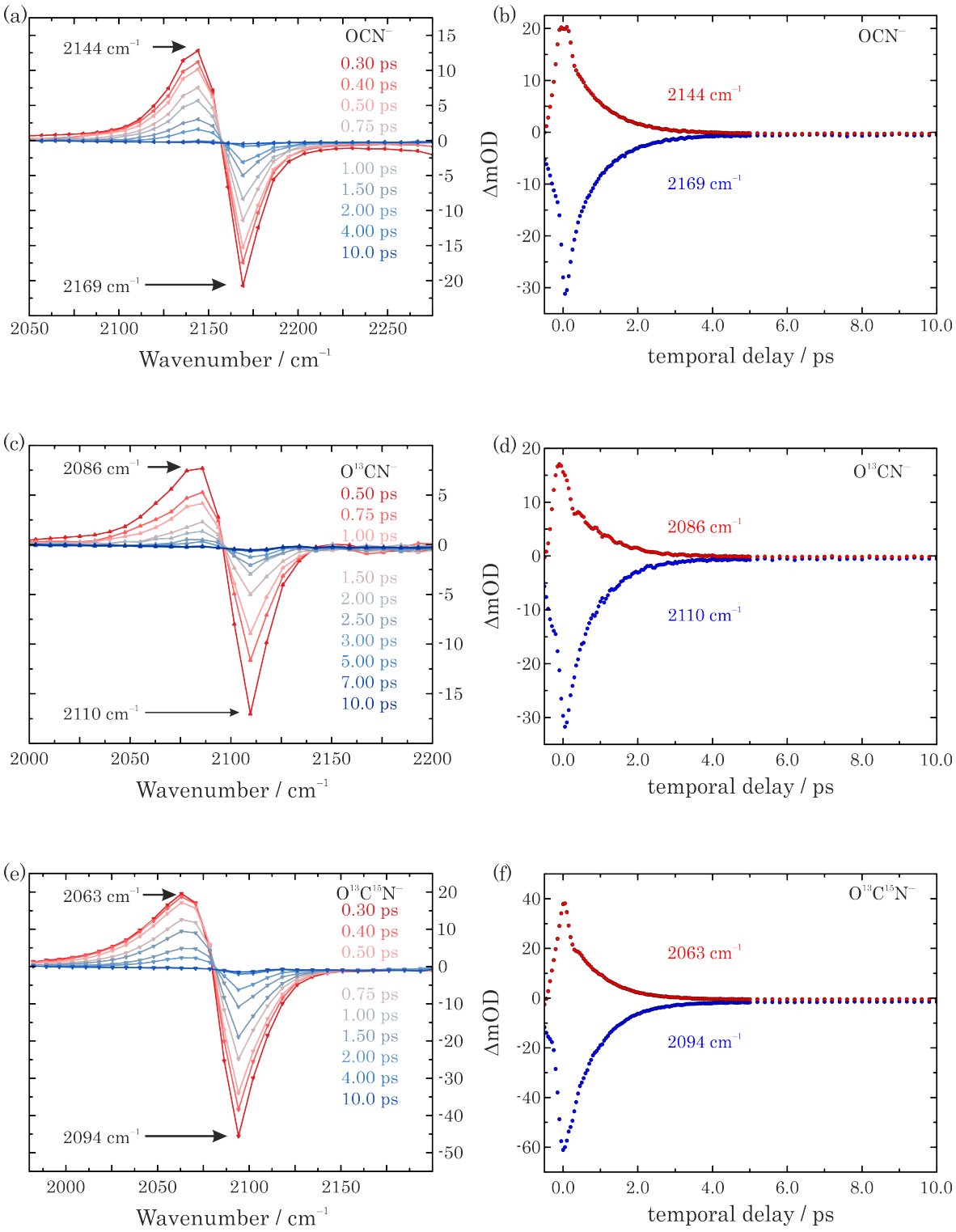

Figure 4.14: Transient pump-probe spectra of (a) OCN^-, (c) $O^{13}CN^-$ and (e) $O^{13}C^{15}N^-$ for different delay times at 333 K and 500 bar. Kinetic traces at the frequency of the maxima of the TA (red circles) and the GB/SE (blue circles) are shown in (b), (d), (f).

Table 4.6: Spectral positions of the GB/SE and the TA signals, vibrational anharmonicities Δ_{11} and wavenumbers of the isosbestic points $\tilde{\nu}_{isos}$ for the investigated aqueous cyanate isotopologues at a temperature of 333 K and a pressure of 500 bar.

Isotopologues	$\mathbf{OCN^-}$	$\mathbf{O^{13}CN^-}$	$\mathbf{O^{13}C^{15}N^-}$
$\tilde{\boldsymbol{\nu}}$**(GB) / cm^{-1}**	2169	2110	2094
$\tilde{\boldsymbol{\nu}}$**(TA) / cm^{-1}**	2144	2086	2063
$\boldsymbol{\Delta}_{11}$ **/ cm^{-1}**	25	24	31
$\tilde{\boldsymbol{\nu}}_{isos}$ **/ cm^{-1}**	2157	2096	2081

observed, whose values are given in table 4.6 too. Neither the spectral positions of the TA and the GB/SE signals nor those of the isosbestic points and values of the anharmonicities depend significantly on the temperature.

As can be seen from figure 4.14, for all isotopologues the relaxation of vibrational energy is well completed within 10 ps considering the achieved signal-to-noise ratio. For a profound investigation of the vibrational energy relaxation, the temporal evolution at the frequency of the maxima of the TA and the GB/SE signals is depicted as kinetic traces in figures 4.14 (b), (d), (f) for the three isotopologues. It is conspicuous that the kinetic traces of the transient absorption and the ground-state bleach behave like mirror-images. As the figure shows, this holds for the different isotopologues. It is a first evidence that the relaxation time of the vibrational energy of the excited state as well as the ground-state recovery time are almost equal.

The kinetic traces can be satisfactorily described by mono-exponential decay functions. This can be seen in semi-logarithmic plots for exemplaric thermodynamic conditions in figures 4.15 (a)-(c). For clarity, the kinetic traces are shifted vertically.

Each kinetic trace displayed in a semi-logarithmic fashion is analyzed with a linear regression. The time constants of the corresponding mono-exponential decay functions can be obtained from the inverse of the slopes of the linear regressions and represent the lifetime τ_1 of the excited state when taken from the transient absorption signal or the ground-state recovery τ_0 in the case of the ground-state bleach. Lifetimes τ_0 and τ_1 are summarized for the investigated temperatures and isotopologues in tables 4.7 and 4.8. As can be seen from both tables, only minor changes in lifetime with temperature are observed, corresponding to only small density variations of the solution. In addition, τ_1 and τ_0 are almost identical for each combination of isotopologue and temperature.

This is in accordance to the observation that the kinetic traces of the TA and the GB/SE behave like mirror images. Furthermore, the lifetimes of the isotopologues

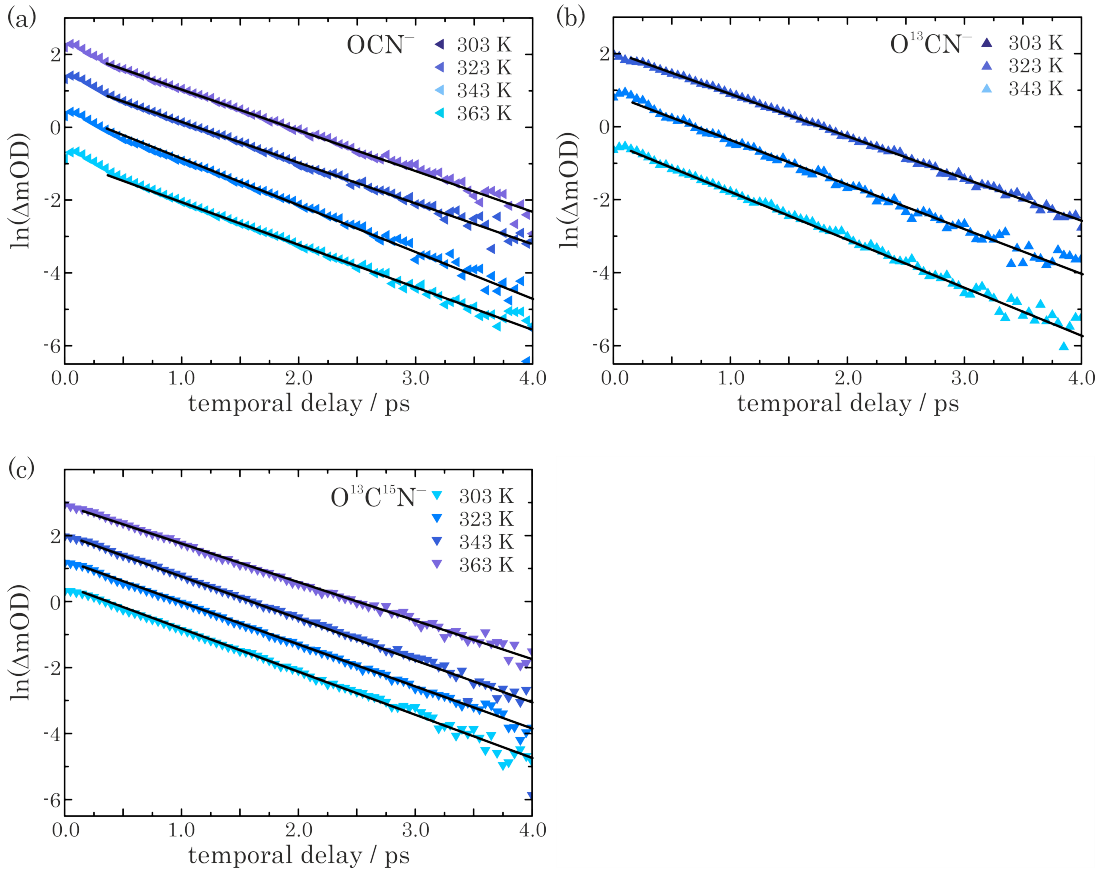

Figure 4.15: Semi-logarithmic plots of kinetic traces at the frequency of the maxima of the transient absorptions for exemplaric temperatures of the investigated aqueous cyanate solutions. For clarity, the kinetic traces are shifted vertically. Linear regressions are represented by black solid lines.

Table 4.7: Excited state lifetimes τ_1 for the aqueous solutions of the isotopologues OCN^-, $O^{13}CN^-$ and $O^{13}C^{15}N^-$ for temperatures between 303 K and 373 K at a pressure of 500 bar.

T / K	τ_1 **(OCN^-) / ps**	τ_1 **($O^{13}CN^-$) / ps**	τ_1 **($O^{13}C^{15}N^-$) / ps**
303	0.790 ± 0.070	0.788 ± 0.014	0.778 ± 0.090
313	0.804 ± 0.062	0.798 ± 0.014	0.797 ± 0.011
323	0.817 ± 0.059	0.818 ± 0.016	0.810 ± 0.041
333	0.821 ± 0.063	0.821 ± 0.011	0.825 ± 0.059
343	0.834 ± 0.064	0.842 ± 0.060	0.837 ± 0.064
353	0.847 ± 0.081	-	0.845 ± 0.070
363	0.865 ± 0.069	-	0.863 ± 0.090
373	0.874 ± 0.062	-	0.874 ± 0.090

agree within the error bars, which means that no distinct isotope effect on the lifetimes

Table 4.8: Ground-state recovery lifetimes τ_0 for the aqueous solutions of the isotopologues OCN^-, $O^{13}CN^-$ and $O^{13}C^{15}N^-$ for temperatures between 303 K and 373 K at a pressure of 500 bar.

T / K	τ_0 **(OCN^-) / ps**	τ_0 **($O^{13}CN^-$) / ps**	τ_0 **($O^{13}C^{15}N^-$) / ps**
303	0.778 ± 0.069	0.783 ± 0.014	0.782 ± 0.090
313	0.792 ± 0.061	0.793 ± 0.014	0.791 ± 0.011
323	0.817 ± 0.060	0.812 ± 0.016	0.808 ± 0.040
333	0.828 ± 0.062	0.824 ± 0.017	0.827 ± 0.061
343	0.842 ± 0.061	0.832 ± 0.060	0.837 ± 0.059
353	0.855 ± 0.079	-	0.841 ± 0.069
363	0.871 ± 0.074	-	0.862 ± 0.089
373	0.886 ± 0.062	-	0.885 ± 0.091

can be observed. Besides, the data show a clear increase of the excited state lifetime as well as of the ground-state recovery lifetime with rising temperature. To analyze the temperature dependence as well as the underlying vibrational energy relaxation, the mechanisms of an intramolecular vibrational redistribution (IVR), a vibrational energy transfer (VET) and a solvent-assisted sequential intramolecular vibrational redistribution (s-IVR) will be discussed in the following.

One possible relaxation mechanism is an intramolecular vibrational redistribution (IVR) from the initially excited ν_3 to other modes in the solute. A scheme of the vibrational manifold of OCN^- [24] is shown in figure 4.16 on the right side, and the vibrational modes are labeled as $|\nu_1\nu_2\nu_3\rangle$. As it can be seen, there are only a few energetically well separated, energy accepting vibrational modes ($|110\rangle$, $|100\rangle$, $|020\rangle$, $|010\rangle$), which are suitable to be involved in the IVR mechanism. Furthermore, the energetic gaps between ν_1 ($|100\rangle$), ν_2 ($|010\rangle$) and ν_3 ($|001\rangle$) modes are quite large. As a consequence, the probability of an IVR is strongly reduced compared to other molecules, in which a high density of accepting modes with matching frequencies exists [23, 127]. Furthermore, the temperature dependence of the lifetimes τ_1 and τ_0 cannot be explained by an IVR. An increase of the temperature leads to accelerated vibrational motions of the molecule so that the loose of vibrational energy will be faster than at room temperature. This results in decreasing lifetimes τ_1 and τ_0 in contradiction to the observed slight increase.

Another possible route is through an external vibrational relaxation, i. e. a vibrational energy transfer (VET) from the solute to the solvent. This is possible if the solvent supplies a suitable acceptor mode to store the vibrational excess energy. Suitable modes

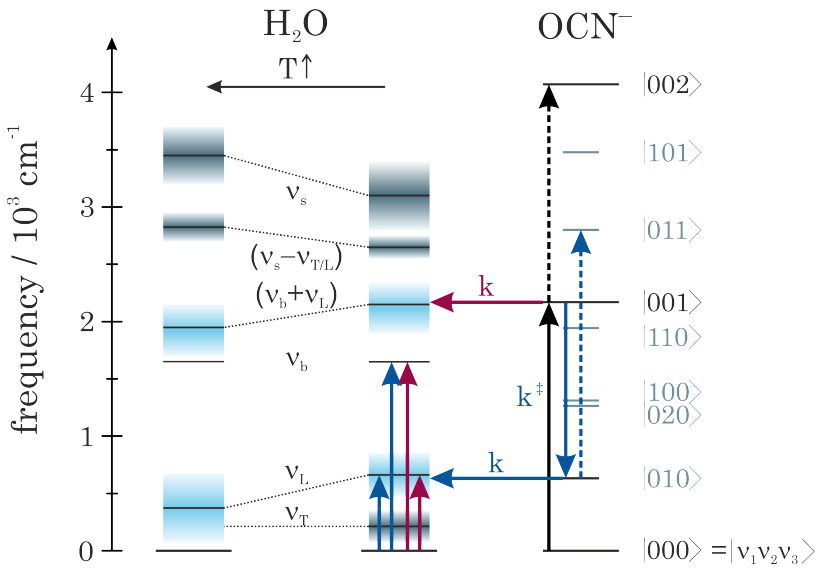

Figure 4.16: Vibrational manifolds of OCN^- (right) [24] and H_2O (middle for 300 K, left for 600 K). The modes of the cyanate anion are labeled as $|\nu_1\nu_2\nu_3\rangle$. Those modes involved in the relaxation process are highlighted in black for OCN^- and in blue for H_2O. As visualized on the left, the solvent levels exhibit a pronounced temperature-dependent energetic shift. Red arrows indicate a VET mechanism involving the $(\nu_b{+}\nu_L)$ combination tone of H_2O, while blue arrows illustrate a solvent-assisted sequential IVR mechanism, in which the intramolecular bending mode as well as the libration of H_2O are involved.

of the solvent H_2O are illustrated in figure 4.16 in the middle for a temperature of around 300 K. The vibrational modes of interest are the libration of H_2O, the bending mode as well as the combination tone $(\nu_b{+}\nu_L)$ of both, because the latter is resonant to the solute's stretching mode ν_3 ($|001\rangle$) (see figure 4.13 (a), figure 4.16). On the left side of the scheme, the temperature-dependent energetic shifts of the solvent modes within the vibrational manifold are depicted with energy level diagrams for the limiting cases at about 600 K. If the vibrational energy transfer is favored, the energy is dissipated from the stretching vibration ν_3 of the solute directly to the resonant combination tone $(\nu_b + \nu_L)$ of H_2O. Once, the vibrational excess energy is dissipated from the solute's ν_3 mode to the solvent, it is delocalized over many H_2O molecules on a time scale of around $\tau_{H_2O} \approx 50$ fs [120] because of the intermolecular couplings between the solvent molecules. The vibrational energy redistribution can also be interpreted by a direct vibration-to-vibration/rotation (V-VR) relaxation process, because the vibrational ν_3 mode of the solute as well as the vibrational bending mode ν_b, which is anharmonically coupled to the rotational libration mode ν_L of water, are involved. The whole process is described with

$$|\nu_3, 0\rangle \xrightarrow{k} |0, (\nu_b + \nu_L)\rangle + |0, \nu_b\rangle + |0, \nu_L\rangle \xrightarrow{1/\tau_{H_2O}} |0, 0\rangle + \Delta E, \tag{4.9}$$

where the first entry in the bracket denotes the mode of the solute and the second that of the solvent. The corresponding energy transfer and excitations in the H_2O are highlighted with red arrows in figure 4.16. Now, the temperature-dependent increase of the lifetime τ can be explained as follows. With rising temperature, the density of the solvent H_2O decreases, and thus, the intermolecular distance between solute and solvent molecules increases. This results in a weakening of the hydrogen bonds. As a consequence, the vibrational energy transfer is more and more hindered with rising temperature resulting in a decelerated VET rate constant from the solute to the solvent. Another point is that the relaxation of vibrational excess energy occurs directly in this mechanism, which is described as the energy transfer from the solute to the solvent following first order kinetics with relaxation rate constant $k = 1/\tau$ (single exponential decay). The energy redistribution within the solvent, by contrast, occurs instantaneously as described above and is not observed in this experiment.

A third possible mechanism is a solvent-assisted sequential intramolecular vibrational redistribution (s-IVR), which involves an intramolecular solute mode and a resonant solvent mode. For that, the bending mode ν_2 of the cyanate anion and the libration ν_L of H_2O are suitable. Energy transfer and excitations for this mechanism are highlighted with blue arrows in figure 4.16 and can be described with

$$|\nu_3, 0\rangle \xrightarrow{k^{\ddagger}} |\nu_2, 0\rangle + |0, \nu_b\rangle \xrightarrow{k} |0, \nu_L\rangle + |0, \nu_b\rangle \xrightarrow{1/\tau_{H_2O}} |0, 0\rangle + \Delta E. \tag{4.10}$$

Here, again, the first entry in the bracket denotes the mode of the solute and the second that of the solvent. To overcome the energy differences within the intra- and intermolecular vibrational energy redistribution, it is assumed that the temperature-independent bending mode of the solvent H_2O is involved. The mechanism can be correctly described by a multi-exponential decay function of the excitation energy with the relaxation rate constants k, the lifetime $k^{\ddagger}$ of the intermediate state ν_2 of the solute and the time constant τ_{H_2O}, which describes the energy relaxation within the solvent. As discussed above, the vibrational energy is delocalized over many water molecules within $\tau_{H_2O} \approx 50$ fs [120]. It is an order of magnitude faster than the observed lifetimes τ_1 and τ_0 and cannot be observed within the temporal resolution of the experiment. Assuming that the rate constant of the initially excited ν_3 mode, i. e. $k^{\ddagger}$, is much longer than the that of the vibrational energy transfer from the solute's ν_2 mode to the solvent's ν_L libration, then the latter energy redistribution describes the rate determining step (rds). Under the assumption that the quasi-stationary approximation [61] holds, then the rate equation can be solved with a mono-exponential decay function.

At this point, it is not possible to distinguish between the VET and the solvent-assisted IVR mechanism. To decide between both cases, Fermi's golden rule is used to validate whether the vibrational energy transfer describes the underlying kinetics of the vibrational energy relaxation of aqueous cyanate solutions correctly.

4.2.3 Discussion in the context of Fermi's golden rule

As outlined in section 2.4, Fermi's golden rule describes the transition rate from a perturbed discrete initial $|i\rangle$ to a final state $|f\rangle$, which is nestled into a continuum of bath states. In the context of the aqueous cyanates, the initial state corresponds to the stretching vibration ν_3, which is perturbed by the excitation pulse. The final state is the $(\nu_b + \nu_L)$ combination mode of H_2O. According to equation (2.71), the transition rate is proportional to the matrix element $|\mathbf{H}'|^2$ and the temperature-dependent spectral overlap integral $S(T)$. In the following, Fermi's golden rule will be applied to distinguish between a VET and a s-IVR as the underlying relaxation process. The result is then discussed in the context of investigations of further triatomic pseudohalide [28, 29, 32, 106] and CO_2 in aqueous solutions.

Temperature-dependent relaxation rate constants $k(T) = 1/\tau(T)$ were determined from time-resolved pump-probe spectroscopy (see section 4.2.2). Assuming that the spectral overlap specifies the temperature dependence entirely, the matrix element $|\mathbf{H}'|^2$ must be temperature-independent. As equation (2.71) indicates, a plot of the relaxation rate constants $k(T)$ against the spectral overlap integral $S(T)$ results in a linear function with a slope m_{fit} proportional to the square of the matrix element and an intercept b_{fit} with the origin. This plot is shown for the investigated isotopologues of cyanate in figure 4.17.

As predicted, a linear dependence of the relaxation rate constant with the spectral overlap is observable for all the isotopologues. However, a fit through the data points of for instance OCN^- results in an intercept of $b_{fit} = (0.54 \pm 0.03)\ \mathrm{ps}^{-1}$. Both, the slopes as well as the intercepts of the linear regression analysis are given in table 4.9.

Table 4.9 shows, that the slopes of the individual fits agree within (94.3 ± 0.3) %, the intercepts within (93.1 ± 0.9) %, considering the standard deviations. However, the non-vanishing intercept in figure 4.17 leads to the conclusion that the assumed VET mechanism from the solute's ν_3 to the solvents $(\nu_b + \nu_L)$ mode cannot be fully described with Fermi's golden rule. This leaves the solvent-assisted sequential IVR as the prime candidate for all investigated cyanate isotopologues.

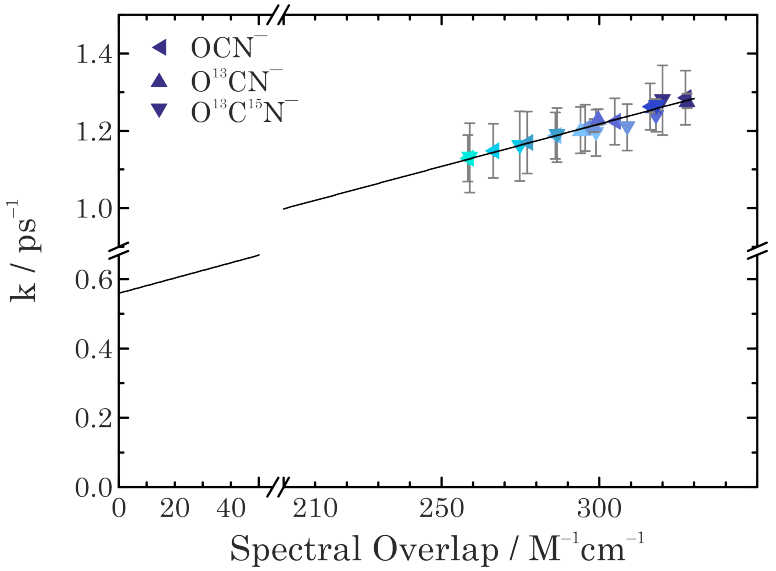

Figure 4.17: Plot of the relaxation rate constant k as a function of the spectral overlap integral of the investigated isotopologues of cyanate with error bars. The colored symbols indicate the investigated temperature range (dark blue (303 K) up to light blue (373 K) in 10 K intervals).

Table 4.9: Fit parameters, i. e. slope m_{fit} and intercept b_{fit}, of the plot of the relaxation rate constant as a function of the spectral overlap of the investigated cyanate isotopologues' absorption band with that of the solvent H_2O.

Isotopologues	$\boldsymbol{m_{fit}}$ **/ ps^{-1} · M · cm**	$\boldsymbol{b_{fit}}$ **/ ps^{-1}**
OCN^-	$(2.26 \pm 0.03) \cdot 10^{-3}$	0.54 ± 0.03
$O^{13}CN^-$	$(2.14 \pm 0.03) \cdot 10^{-3}$	0.58 ± 0.03
$O^{13}C^{15}N^-$	$(2.13 \pm 0.03) \cdot 10^{-3}$	0.57 ± 0.03

In former studies, other triatomic pseudohalide anions, i. e. azide N_3^-, thiocyanate SCN^- and its isotopologue $SC^{15}N^-$ as well as selenocyanate $SeCN^-$, were investigated [27, 28, 32]. Their stretching vibrations ν_3 absorb in the same spectral range as the cyanate does (see table 4.10). Stationary FTIR spectra of their aqueous solutions are shown at ambient temperature and a pressure of 500 bar in figure 4.18.

Table 4.10: Spectral positions of the stretching absorption band of azide, thiocyanate and selenocyanate.

Isotopologue	**N_3^-**	**SCN^-**	**$SC^{15}N^-$**	**$SeCN^-$**
$\boldsymbol{\nu_3}$ **/ cm^{-1}**	2050	2038	2063	2073

The analysis of their temperature-dependent pump-probe measurements yield the life-

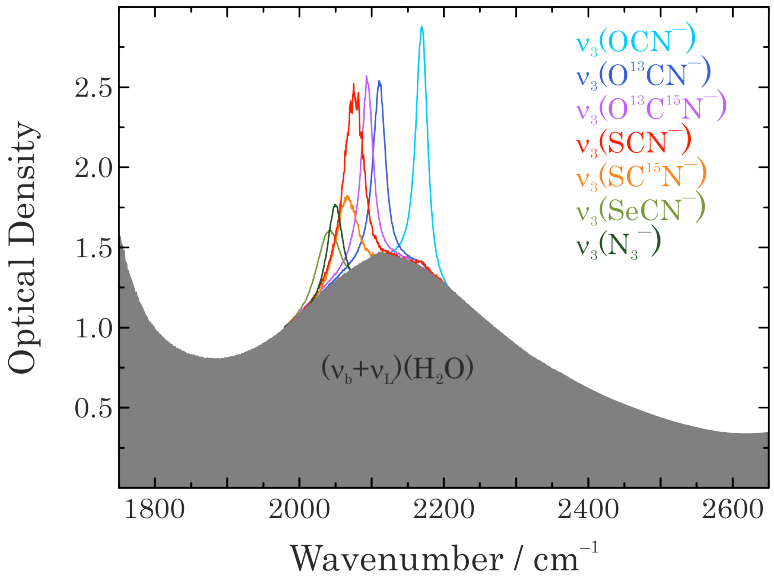

Figure 4.18: Stationary FTIR spectra of aqueous azide, cyanate, thiocyanate and selenocyanate solutions at ambient temperature and 500 bar [32].

times τ_1. Those are given for three exemplaric thermodynamic conditions in table 4.11. Furthermore, the isoelectronic CO_2 and its lifetimes in H_2O are shown for comparison. It is noteworthy that, according to the investigated isotopologues of the cyanate anion, the lifetimes of the SCN^- and its isotopologue $SC^{15}N^-$ are equal within the error limits [32].

Table 4.11: Excited state lifetime τ_1 for the aqueous N_3^-, OCN^-, SCN^- and $SeCN^-$ solutions as well as of CO_2 in H_2O for three exemplaric temperatures and at 500 bar. Lifetimes of aqueous azide, thiocyanate and selenocyanate solutions are extracted from literature [32].

Anion	**T / K**		
τ_1 / ps	**303**	**363**	**453**
N_3^-	0.70 ± 0.02	0.73 ± 0.03	0.74 ± 0.03
OCN^-	0.79 ± 0.07	0.87 ± 0.07	-
$O^{13}CN^-$	0.79 ± 0.01	-	-
$O^{13}C^{15}N^-$	0.78 ± 0.09	0.86 ± 0.09	-
SCN^-	2.33 ± 0.03	2.61 ± 0.06	2.92 ± 0.07
$SC^{15}N^-$	2.23 ± 0.03	2.70 ± 0.08	2.95 ± 0.09
$SeCN^-$	3.99 ± 0.01	4.35 ± 0.02	4.70 ± 0.05
CO_2	9.0 ± 0.1	9.9 ± 0.2	11.6 ± 0.2

The comparison of the excited state lifetimes of the pseudohalide anions shows that the relaxation is fastest for the N_3^-, and slowest for the $SeCN^-$ in H_2O. However,

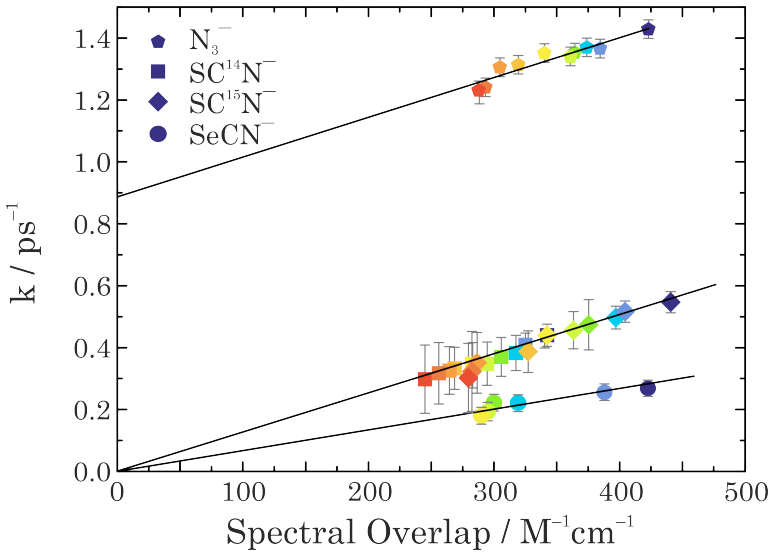

Figure 4.19: Plot of the relaxation rate constant $k_1 = 1/\tau_1$ as a function of the spectral overlap integral for N_3^- (pentagons), SCN^- (squares) and $SeCN^-$ (circles). The colored symbols indicate the investigated temperature range (from 303 K (dark blue) to 603 K (red)). Error bars of the relaxation rate constants are added. (Extracted from [32].)

the relaxation of isoelectronic CO_2 in H_2O at room temperature is more than a factor of two slower than that of the $SeCN^-$ anion in H_2O. However, for all investigated triatomic molecules, the lifetimes increase with rising temperature. In figure 4.19, the relaxation rate constants as a function of the spectral overlap integrals are shown for the N_3^-, the SCN^- and its isotopologue $SC^{15}N^-$ as well as for the $SeCN^-$ anions. The data were extracted from [32] and the spectral overlap integral for each pseudohalide anion was determined as explained in chapter 2.4.

As discussed before, the vibrational energy relaxation of the cyanate anion and its isotopologues in H_2O as well as of the CO_2 in H_2O follow a solvent-assisted sequential IVR. The offset of k observed for a spectral overlap of $S = 0$ can be understood if the bending mode of the solvent is considered. This mode matches the lack of energy in the IVR with $k^{\ddagger}$ and the VET with k. Furthermore, the bending mode of H_2O is temperature-independent and its excitation leads to a constant additive contribution to the relaxation rate constants. In the literature [27, 30, 128, 129], the vibrational energy redistribution of an aqueous N_3^- solution can be described by two mechanisms, a pure intermolecular energy transfer from the solute's ν_3 to the solvent's combination tone $(\nu_b + \nu_L)$ or a solvent assisted sequential IVR involving the symmetric stretching vibration ν_1 of the azide anion and the libration of water [27,30]. From figure 4.19, it is obvious that the relaxation rate constant of N_3^- plotted as a function of the spectral overlap $S(T)$ results in a non-vanishing intercept (see table 4.12), i.e. in an offset of

k, and thus, the underlying mechanism cannot be fully described with Fermi's golden rule. This means that besides a VET a solvent assisted sequential IVR is contributing to the overall relaxation mechanism.

However, the relation between the relaxation rate constants and the spectral overlaps for SCN^-, $SC^{15}N^-$ and $SeCN^-$ in aqueous solution show a clear linear dependence with vanishing intercept. In accordance with the shorter lifetime of SCN^- in H_2O compared to the that of the aqueous $SeCN^-$ solution, the slopes m_{fit} vary, i. e. the slope of the investigated SCN^- solution is steeper than that of the $SeCN^-$ solution. The data obtained from the linear regression analysis are summarized in table 4.12.

Table 4.12: Slopes m_{fit} and intercepts b_{fit} extracted from the linear regression analysis of the relaxation rate constant as a function of the spectral overlap integral $S(T)$ for various triatomic molecules. The data are extracted from figures 4.9, 4.17 and 4.19.

Anion	$\boldsymbol{m_{fit}}$ **/ ps^{-1} · M · cm**	$\boldsymbol{b_{fit}}$ **/ ps^{-1}**
$\mathbf{N_3^-}$	$(1.29 \pm 0.01) \cdot 10^{-3}$	0.88 ± 0.05
$\mathbf{OCN^-}$	$(2.26 \pm 0.03) \cdot 10^{-3}$	0.54 ± 0.03
$\mathbf{O^{13}CN^-}$	$(2.14 \pm 0.03) \cdot 10^{-3}$	0.58 ± 0.03
$\mathbf{O^{13}C^{15}N^-}$	$(2.13 \pm 0.03) \cdot 10^{-3}$	0.57 ± 0.03
$\mathbf{SCN^-}$	$(1.24 \pm 0.01) \cdot 10^{-3}$	0
$\mathbf{SC^{15}N^-}$	$(1.26 \pm 0.01) \cdot 10^{-3}$	0
$\mathbf{SeCN^-}$	$(0.67 \pm 0.02) \cdot 10^{-3}$	0
$\mathbf{CO_2}$	$(0.35 \pm 0.02) \cdot 10^{-3}$	0.047 ± 0.003

At this point, the competing vibrational energy redistribution mechanisms of the investigated molecules solved in H_2O are considered more in detail. The vibrational energy relaxation of the azide and the cyanate aqueous solutions as well as of the CO_2 in H_2O follow a solvent assisted sequential IVR involving the bending vibration ν_2 of OCN^- or CO_2 or respectively the symmetric stretching vibration ν_1 of N_3^- and the libration of H_2O. In contrast, the VER of the SCN^- and $SeCN^-$ solutions result in a direct vibrational energy transfer from the excited ν_3 mode to the resonant $(\nu_b + \nu_L)$ of the solvent H_2O. Interestingly, the change of the VER mechanism within the series of investigated triatomic molecules shows a striking correlation with the nature of the ν_3 vibration. For the azide and cyanate anions, the charge distribution is delocalized over the molecule, while for the thiocyanate and selenocyanate, the charge distribution is asymmetric, and thus localized on the C and N atoms [24, 26]. For the latter anions, the ν_3 vibration can be described as a ν_{CN} stretching mode.

From the investigations of the VET of the SCN^- and $SeCN^-$ solutions, the coupling matrix element can be assessed, which in turn gives an evidence to the coupling strength between the solute and the solvent. A comparison of the slopes of both anions shows that they differ by a factor of around 1.8, indicating that the coupling strength of the SCN^- anion with H_2O is stronger than for the $SeCN^-$ with H_2O. This tendency can be also deduced from the lifetimes τ of the individually molecules in aqueous solutions to be (see table 4.11)

$$\tau(N_3{}^-) \approx \tau(OCN^-) > \tau(SCN^-) > \tau(SeCN^-) > \tau(CO_2). \tag{4.11}$$

As described in chapter 4.1.1, Zukowski et al. [111] reported about a weak hydration shell of CO_2 in H_2O caused by an endothermic formation of hydrogen bonds. Considering the pseudohalide anions, Lenchenkov et al. [24] assumed that the trend, as shown in eq. (4.11), is due to the larger partial charges on the individual atoms within the anion and a smaller energy mismatch in the pathway. Assuming that the partial charges on the individual atoms increase from SCN^- to $SeCN^-$ then the polarizability of the anions rises with increasing size of the molecule as it is stated in the Pearson acid-base concept.

For further investigations, theoretical calculations of the SCN^- and $SeCN^-$ anions based on density functional theory (DFT) were done with the program ORCA [130]. A hybrid functional B3-LYP [131] was applied as well as the triple ζ-TZVP basis set [132,133]. The RICOSX approximation additionally to the auxiliary basis set TZVP/J [134] was used. Solvation effects of H_2O were studied with the help of a conductor-like screening model (COSMO). The isotropic polarizability was then extracted from these calculations. Comparing the ratio of the slopes of SCN^- and $SeCN^-$ with that of the isotropic polarizabilities α_{iso} results in the following:

$$\frac{m(SCN^-)}{m(SeCN^-)} = 1.8 \longleftrightarrow \frac{\alpha_{iso}(SeCN^-)}{\alpha_{iso}(SCN^-)} \cdot \sqrt{(2)} = 1.8 \tag{4.12}$$

A striking correlation between the matrix element $|\mathbf{H'}|^2$ and the inverse of the isotropic polarizability with a proportionality factor of $\sqrt{2}$ can be observed. To verify this correlation, further investigations of the bending vibration of OCN^- and CO_2 as well as of the symmetric stretching vibration of $N_3{}^-$ have to be preformed.

4.2.4 Conclusion II

The absorption spectra of aqueous cyanate and its investigated isotopologues feature a resonance of the stretching mode ν_3 of the solute with the solvent's $(\nu_b + \nu_L)$ mode. The spectral overlap between both bands decreases with rising temperature due to the temperature-dependent spectral shift of the combination tone. The relaxation dynamics extracted from the time-resolved pump-probe spectra recorded under isobaric conditions and temperatures between 303 K and 373 K indicate that a solvent-assisted sequential IVR predominates, in which an intramolecular energy relaxation from the ν_3 to the bending mode ν_2 occurs. It is followed by an intermolecular energy transfer to the librational modes of H_2O and a subsequent redistribution of vibrational energy within the solvent. In order to explain the relaxation described by a mono-exponential decay function, the time constant of the intramolecular energy redistribution must be shorter than that of the intermolecular energy transfer. Furthermore, no distinct isotope effect on the time constants of the three cyanate isotopologues was observed

Comparing different pseudohalide anions, i. e. azide, cyanate, thiocyanate and selenocyanate, the lifetime of the azide is the shortest, followed by that of the cyanate, the thiocyanate and the selenocyanate, which is the longest one. As a result of the solvent-assisted sequential IVR of the aqueous cyanate, azide and carbon dioxide solutions, only the relaxation dynamics of the thiocyanate and selenocyanate could be discussed in the context of Fermi's golden rule. By means of the relaxation rate constants and the spectral overlap integrals, the coupling strength between solute and solvent was estimated. The coupling strength between SCN^- and H_2O is stronger than that between $SeCN^-$ and H_2O. This tendency can be validated by the polarizability, i. e. the more polarizable a molecule is the weaker the coupling between solute and solvent is.

The underlying mechanism of the relaxation dynamics of cyanate and its isotopologues in H_2O are similar to that of the isovalent azide anion as well as to that of the isoelectronic carbon dioxide dissolved in H_2O. Nevertheless, the lifetimes of the azide and cyanate differ more than ninefold compared to the that of the CO_2, which may indicate that the coupling strength between cyanate and H_2O or respectively N_3^- and H_2O is stronger than between CO_2 and H_2O.

4.3 Two-dimensional infrared spectroscopy of MBO in tetrachloroethylene

In this chapter, the investigations of conformational dynamics of a *trans*-4-methoxybut-3-en-2-one solution by means of the 2D-IR spectroscopy are presented. The experimental setup of the pump-probe spectrometer used the pulse shaper as described in section 2.3 and 3 to record 2D-IR spectra in the time-frequency domain.

The *trans*-4-methoxybut-3-en-2-one is abbreviated in the following as MBO. It an be assigned to the substance class of β-alkoxy-α,β-unsaturated ketones. The chemical structure of MBO is shown in figure 4.20.

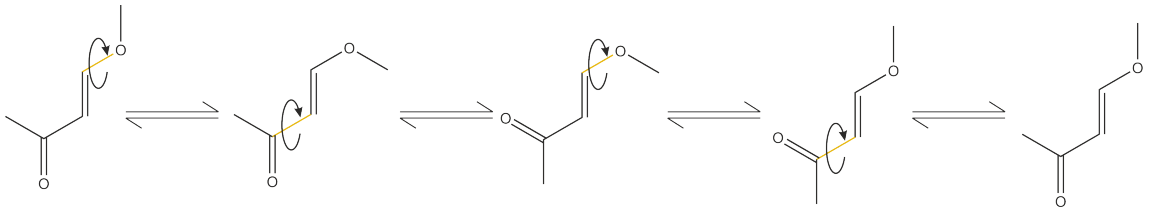

Figure 4.20: Chemical structure of *trans*-4-methoxybut-3-en-2-one in tetrachloroethylene. Four different rotamers are possible due to restricted rotations, which are indicated by arrows, regarding the C_{sp^2}-C_{sp^2} or the C_{sp^2}-O single bonds (highlighted in yellow). The outermost depicted rotamers are identical.

Restricted rotations, indicated by curved lines with arrows in figure 4.20, regarding the C_{sp^2}-C_{sp^2} or C_{sp^2}-O single bonds (highlighted in yellow) occur and result in four different stereo-isomers of the MBO. Their notations according to the IUPAC nomenclature are given on the bottom of figure 4.20. The rotamers have in common that the residues are in *trans* configuration relative to the C=C double bond. Each can be differentiated into two subclasses, i. e. in *trans/s-trans* and *trans/s-cis*.

Within this work, the investigation of the vibrations of the conjugated C=C double bond as well as that of the carbonyl group are of particular interest. They give rise to eight different vibrational bands, which absorb in a spectral range from 1500 cm^{-1} to 1700 cm^{-1} [135]. A normalized stationary absorption spectrum of MBO in C_2Cl_4 within this spectral range is shown in figure 4.21. Here, seven out of eight expected absorption bands with different FWHM and optical densities can be observed with a reasonable signal-to-noise ratio. The eighth absorption band cannot be monitored with the achieved signal-to-noise ratio in a solution with a concentration of 0.072 mol/l,

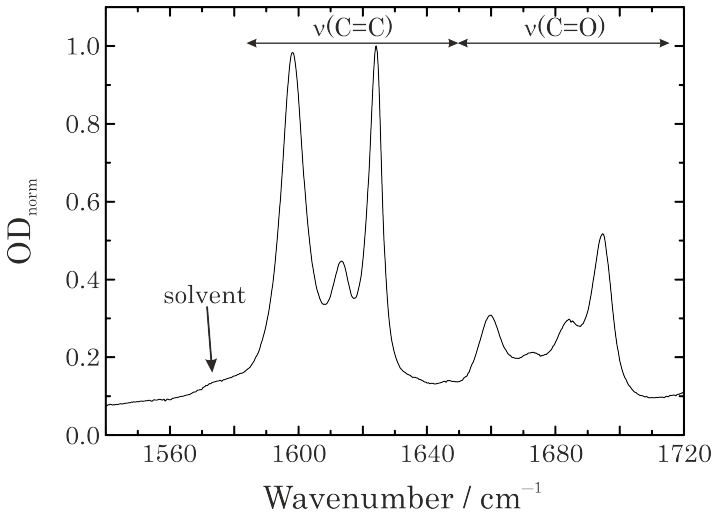

Figure 4.21: Normalized stationary absorption spectrum of MBO in C_2Cl_4. Seven absorption bands with different FWHM and optical densities of the rotamers as well as a solvent's absorption band with low intensity (highlighted with an arrow) are recognizable.

because its optical density is very low. To determine the full-widths at half-maximum, a Lorentzian profile, i. e.

$$f^{Lo}(\gamma, \tilde{\nu}) = \frac{\mathrm{OD}(\tilde{\nu}_c)\ \gamma^2}{(\tilde{\nu} - \tilde{\nu}_c)^2 + \gamma^2} \qquad (4.13)$$

$$2\ \gamma = \mathrm{FWHM}$$

with the 2 γ as the full-width at half-maximum (FWHM), the optical density (OD) and the center frequency $\tilde{\nu}_c$, was fitted to the individual absorption bands. The experimentally observed center frequencies $\tilde{\nu}_c$ and corresponding optical densities OD_{norm} are summarized in table 4.13. They were used to reduce the adapting parameters within the Lorentzian fit to at least γ.

The solvent tetrachloroethylene possesses only a very weak absorption band within the depicted spectral range, which is centered at around 1577 cm^{-1} (highlighted by an arrow in figure 4.21). It can be attributed to a combination tone ($\nu_2 + \nu_6 + \nu_{11}$) of CCl stretching vibrations [137].

An assignment of the absorption bands to the vibrations of the corresponding rotamers cannot be made with only the absorption spectrum. Nevertheless, a classification in two spectral regions can be done. The spectral range from around 1540 cm^{-1} up to approximately 1650 cm^{-1} can be assigned to the ν(C=C) stretching vibrations, while that from around 1650 cm^{-1} up to 1720 cm^{-1} can be attributed to the stretching

Table 4.13: Center frequencies $\tilde{\nu}_c$, FWHM and normalized optical density of the observable absorption bands of MBO in C_2Cl_4 within the absorption spectrum. The center frequencies found in literature [136] are also given.

$\tilde{\nu}_{Lit}$ / cm^{-1}	$\tilde{\nu}_c$ / cm^{-1}	FWHM / cm^{-1}	OD_{norm}
1601	1598.0 ± 0.5	9.3 ± 0.2	0.98 ± 0.02
1615	1613.0 ± 0.5	5.6 ± 0.2	0.45 ± 0.02
1626	1624.0 ± 0.5	5.6 ± 0.2	1.00 ± 0.02
1662	1660.0 ± 0.5	10.3 ± 0.2	0.31 ± 0.02
1675	1673.0 ± 0.5	9.1 ± 0.2	0.21 ± 0.02
1686	1684.0 ± 0.5	7.6 ± 0.2	0.30 ± 0.02
1697	1694.0 ± 0.5	9.1 ± 0.2	0.52 ± 0.02

vibrations of the carbonyl group (ν(C=O)) [135]. Although the vibrations of the C=C and C=O groups are strongly coupled, the bands will be called ν(C=C) and ν(C=O) for simplicity.

Dabrowski et al. [136] reported on an assignment of the ν(C=C) and ν(C=O) absorption bands to the four rotamers using FTIR spectroscopy. They varied the substituents centered at the carbonyl group, the unsaturated C=C bond and the ether group with the result that the spectral positions of the absorption bands changed. Thereof, they assigned the bands to the corresponding oscillators of the rotamers. However, this method is not exact and time consuming. An assignment using the 2D-IR spectroscopy is more accurate, straightforward and thus, faster. It becomes apparent that the assignment found in the literature is not exact and a coupling of different rotamers will be found.

In figure 4.22, a contour plot of the 2D-IR spectrum at a delay time of $t_1 = 0.6$ ps, the earliest one without coherent artifact, is presented. A complex pattern of diagonal and off-diagonal peaks is observable. A pump-induced reduction of the detected intensity is marked with blue contours, an increase of it with red ones (see section 2.3). For guidance, the normalized stationary absorption spectrum is plotted on top of each 2D-IR spectrum. The occurrence of cross peak pattern at earliest delay times points to a coupling of two oscillators rather than to a chemical exchange. For detailed information, it is referred to section 2.3, and figures 2.8 (c, d). In the following, the peak pattern is analyzed more in detail. Therefore, in figures 4.23 (a)-(b) different patterns are highlighted for a detailed discussion.

Within figure 4.23, four contour plots at the temporal delay of $t_1 = 0.6$ ps are shown. Each sub-figure highlights a different pair of diagonal and off-diagonal cross peaks. For

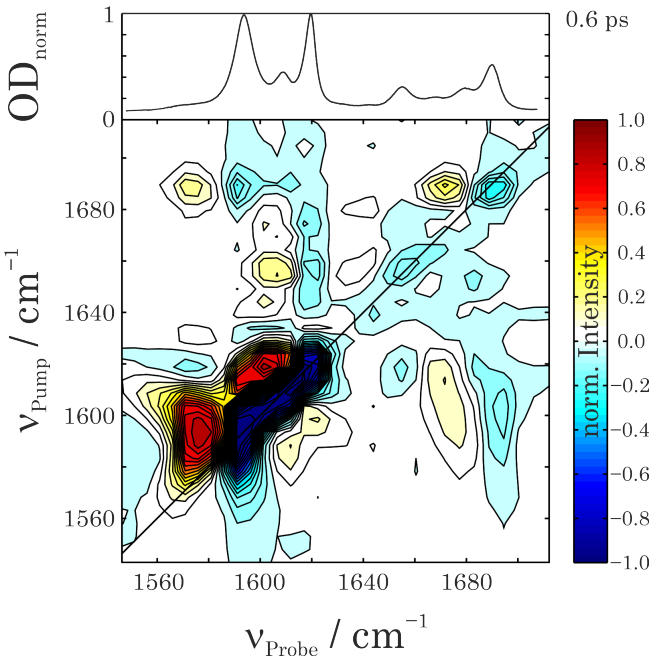

Figure 4.22: 2D-IR spectrum of MBO in C_2Cl_4 at a delay time of $t_1 = 0.6$ ps. For guidance, the normalized stationary absorption spectrum is shown on top of the contour plot.

instance in figure 4.23 (a), the diagonal peaks centered at 1598 cm^{-1} and 1694 cm^{-1} are emphasized as well as the corresponding off-diagonal peaks. The latter absorption band is located in the ν(C=O) spectral range, while the former in the ν(C=C) range. These can be assigned to a rotamer numbered with 1 in table 4.14. Similar is the assignment for the cross peak pattern in sub-figure (b) and (c). In the former, the peaks centered at 1613 cm^{-1} and 1684 cm^{-1} feature a coupling pattern (rotamer 2 in table 4.14), while in the latter, the peaks are centered at 1624 cm^{-1} and 1660 cm^{-1} and are assigned to rotamer 3 in table 4.14. To accentuate more cross peak patterns, the range of signal intensities around zero is elongated, normalized and shown in sub-figure (d). The high-frequency peak can be attributed to an absorption band centered at 1673 cm^{-1}, which is located in the spectral range of the ν(C=O) vibration. The low-frequency peak is centered at 1647 cm^{-1} and thus, in the spectral region of the ν(C=C) stretching vibration. These pattern is assigned to rotamer 4 in table 4.14. For the latter mentioned frequency a band with very low intensity was observed in the stationary absorption spectrum, meaning that only low amounts of this rotamer are present in solution. At this point, it is noteworthy, that the peak intensity of a 2D-IR spectrum scales with $|\mu|^4$ (μ is a transition dipole moment), while that of a stationary absorption spectrum with $|\mu|^2$ [56]. The above described first assignment is concluded in table 4.14.

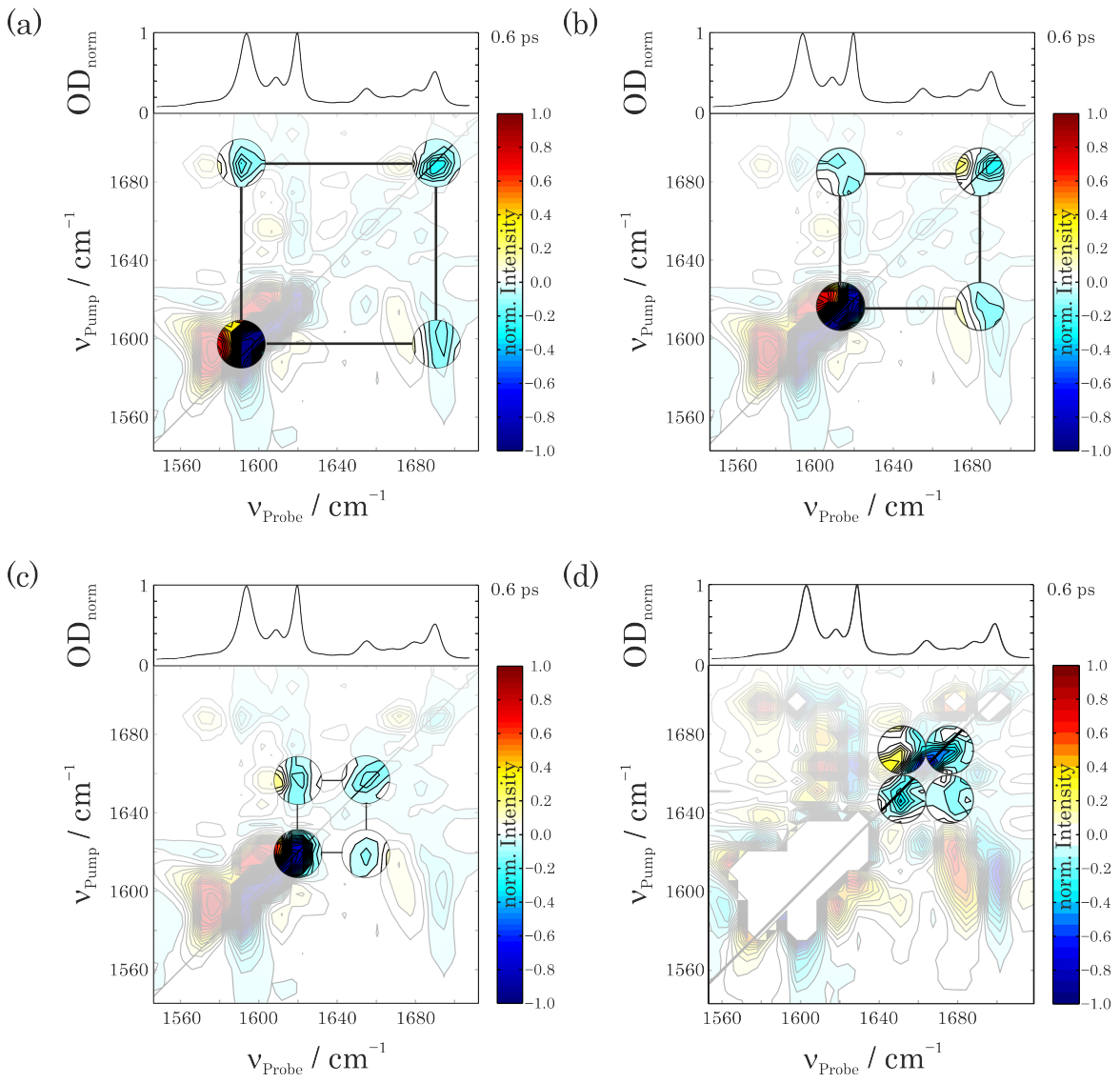

Figure 4.23: 2D-IR spectra of MBO in C_2Cl_4 at a delay time of $t_1 = 0.6$ ps. For guidance, the normalized stationary absorption spectrum is shown on top of the contour plot. Highlighted are different pattern of diagonal and off-diagonal peaks of two absorption bands centered at (a) 1598 cm^{-1} and 1694 cm^{-1} and (b) at 1613 cm^{-1} and 1684 cm^{-1}. (c) highlights a pattern of diagonal and off-diagonal peaks of two absorption bands centered at 1624 cm^{-1} and 1660 cm^{-1} and (d) at 1647 cm^{-1} and 1673 cm^{-1}.

Table 4.14: Assignment of ν(C=C) and ν(C=O) absorption bands due to cross peaks in the 2D-IR spectrum at t_1=0.60 ps.

$\tilde{\nu}$(C=C) / cm^{-1}	$\tilde{\nu}$(C=O) / cm^{-1}	rotamer
1598 ± 0.5	1694 ± 0.5	rotamer 1
1613 ± 0.5	1684 ± 0.5	rotamer 2
1624 ± 0.5	1660 ± 0.5	rotamer 3
1647 ± 0.5	1673 ± 0.5	rotamer 4
-	(1660, 1684)	rotamer 2+3

However, another cross peak pattern is recognizable, and highlighted in 4.24. Here, a pattern of two vibrational modes, which absorb in the ν(C=O) range, is observable indicating a coupling of both modes (see table 4.14, bottom) and thus, a coupling of two rotamers. The reason for this as well as the final assignment of the different patterns to the rotamers are presented in the following.

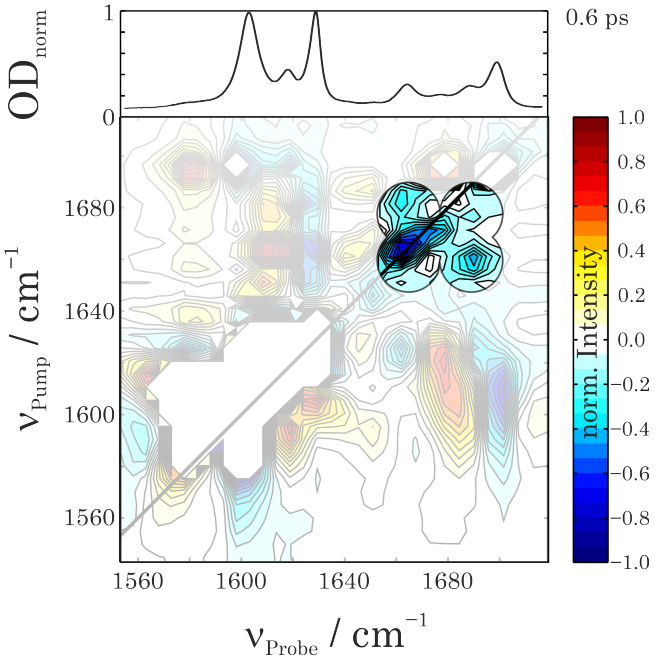

Figure 4.24: 2D-IR spectrum of MBO in C_2Cl_4 at a delay time of $t_1 = 0.6$ ps to emphasize a pattern of vibrational modes, which are assigned to two rotamers. For guidance, the normalized stationary absorption spectrum is shown on top of the contour plot.

For a final assignment of the pattern to the rotamers, it is made use of the Förster theory, which was described in section 2.5. It deals with an intra- or resonant intermolecular energy transfer from an energy donor (D) to an energy acceptor (A) [87]. In the following, eq. (2.81) will be used to describe the relation between the interaction matrix element $\mathbf{H}_{DA}^{el}$, the dipole strength of a functional group and an orientation fac-

tor. To estimate the magnitude of the dipole strength of each functional group within the different rotamers, quantum mechanical calculations were performed by Prof. Dr. P. Vöhringer using the Gaussian [138] program. For this, the B97D3 dispersion functional [139] and an Ahlrichs def2-TZVP basis set [140] were used. Additionally, the conductor-like polarizable continuum model (CPCM) was applied in Gaussian [141]. The dipole strengths of each vibrational mode are then obtained by the product of the partial charges e_i of functional group i with typical[9] bond lengths r given in table 4.15 [142] according to

$$D_i = \sum_i \frac{r}{2} \cdot e_i. \tag{4.14}$$

Table 4.15: Typical bond lengths used for the calculation of distances and angles [142].

r(C=O)	**r(C=C)**	**r(C−C)**
122 pm	134 pm	154 pm

The angles α, β and θ as well as the distance vector between the C=C and C=O functional groups were calculated by means of drafts, which consider the spatial arrangement of the rotamers after geometry optimization. They are shown in figure 4.25, and highlight the structures of both subclasses *trans/s-trans* ((a), (c), (e)) and *trans/s-cis* ((b), (d), (f)).

Based on eq. (2.81), the orientation factors κ as well as the interaction matrix elements H_{DA}^{el} of each individual functional groups are obtained, and presented in table 4.16.

Table 4.16: Calculated distance vectors $\mathbf{R}_{DA}$, angles α, β and θ as well as orientation factors κ to determine the interaction matrix element $\mathbf{H}_{DA}^{el}$ for the subclasses *trans/s-trans* and *trans/s-cis* of the MBO rotamers.

	trans/s-trans	***trans/s-cis***
$\mathbf{R}_{DA}$	272 pm	206 pm
$\boldsymbol{\alpha}$	33°	295°
$\boldsymbol{\beta}$	20°	60°
$\boldsymbol{\theta}$	0°	120°
$\boldsymbol{\kappa}$	-1.36	-1.13
$\mathbf{H}_{DA}^{el}$	$1.22 \cdot 10^{18}$ C/m^2	$2.63 \cdot 10^{18}$ C/m^2

[9]Typical bond lengths are the median of all values for that bond length found in an sample.

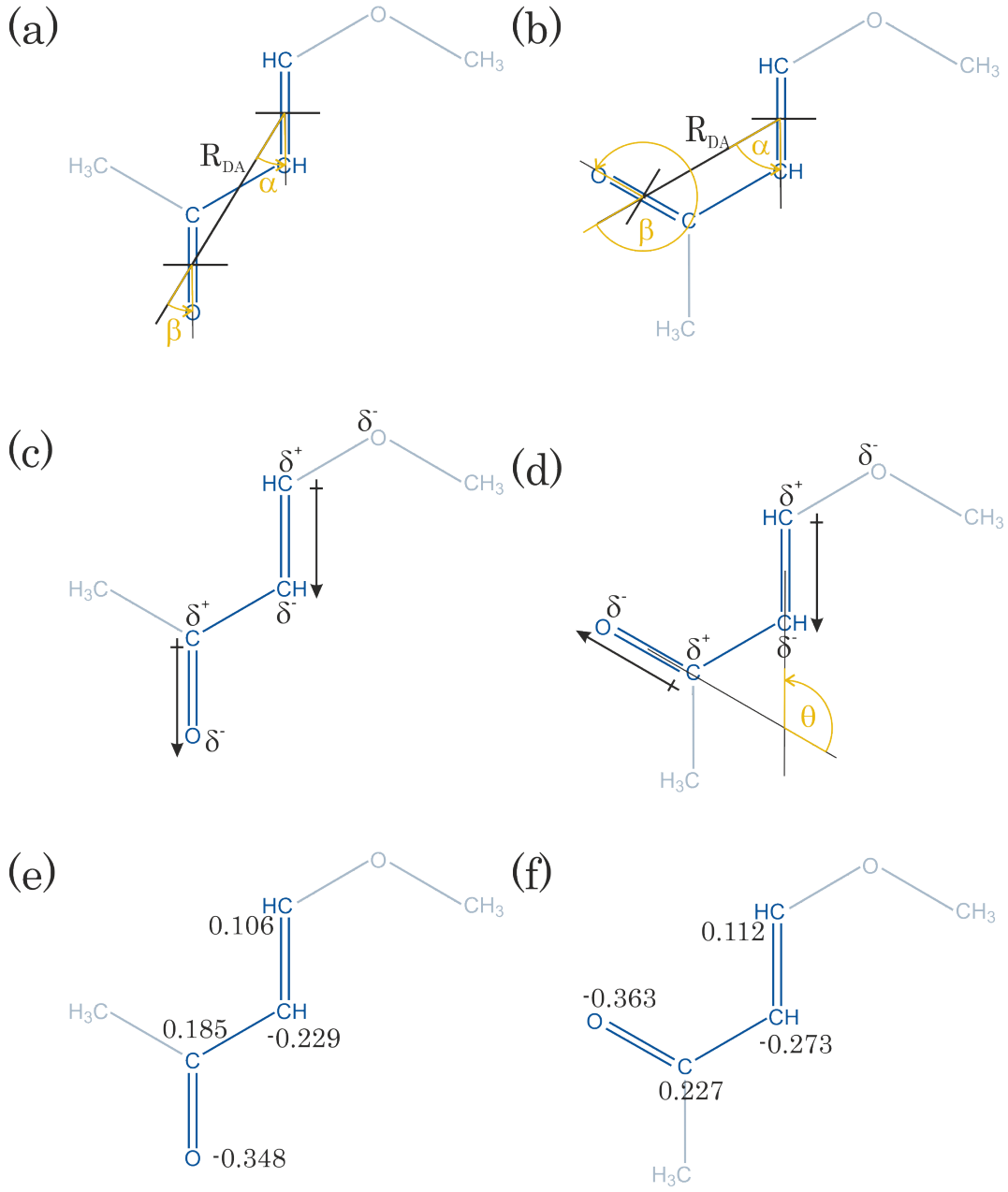

Figure 4.25: Schematic structure of MBO after geometry optimization. In (a) and (b) the subclasses *trans/s-trans* and *trans/s-cis* are shown, and the distance $\mathbf{R}_{DA}$ as well as the angles are displayed. In (c) and (d), the dipole moments are highlighted, and the computed partial charges for each subclass are given in (e) and (f).

As can be seen from table 4.16, the matrix element H_{DA}^{el} of a *trans/s-cis* rotamer is doubled compared to that of a *trans/s-trans* rotamer. This means, that the energy split of the absorption bands of the ν(C=C) and ν(C=O) stretching modes of a *trans/s-cis* rotamer is higher that of a *trans/s-trans* rotamer. At the same time, the energy split of a *trans/s-cis/O-s-cis* is as well higher than of a *trans/s-cis/O-s-trans* rotamer. In table 4.17, these energy differences between both oscillators within a molecule are listed together with the final assignment of the absorption bands to the rotamers.

Table 4.17: Final assignment of ν(C=C) and ν(C=O) vibrational modes to the four rotamers of MBO.

$\tilde{\nu}$(C=C) / cm^{-1}	$\tilde{\nu}$(C=O) / cm^{-1}	$\Delta\tilde{\nu}$ / cm^{-1}	rotamer
1598 ± 0.5	1694 ± 0.5	96 ± 0.5	*trans/s-cis/O-s-cis*
1613 ± 0.5	1684 ± 0.5	71 ± 0.5	*trans/s-cis/O-s-trans*
1624 ± 0.5	1660 ± 0.5	36 ± 0.5	*trans/s-trans/O-s-cis*
1647 ± 0.5	1673 ± 0.5	26 ± 0.5	*trans/s-trans/O-s-trans*

The rotamer, whose absorption bands possesses the highest energy splitting, is the *trans/s-cis/O-s-cis*, as presented in table 4.17. The assignment is highlighted in figure 4.26 (in purple) based on the parameters given in table 4.13. The absorption bands of the ν(C=C) and ν(C=O) stretching vibrations, centered at 1613 cm^{-1} and 1684 cm^{-1}, are assigned to the *trans/s-cis/O-s-trans* rotamer (colored in green in figure 4.26), while those centered at 1624 cm^{-1} and 1660 cm^{-1} to the *trans/s-trans/O-s-cis* rotamer (blue colored absorption bands in figure 4.26). The rotamer, whose stretching bands show the lowest energy split, is the *trans/s-trans/O-s-trans*, which is highlighted in red in figure 4.26.

In the next paragraph, the occurrence of the cross peak pattern, which was presented in figure 4.24, is explained. Herein, two oscillators, which are associated to the *trans/s-trans/O-s-cis* and *trans/s-cis/O-s-trans* rotamers, are coupled at a delay time of 0.6 ps. In the following, two possible approaches regarding the occurrence of the coupling are discussed.

Firstly, according to figure 4.26 (b), two restricted rotations regarding the C_{sp^2}-C_{sp^2} and C_{sp^2}-O single bonds are essential to convert rotamer *trans/s-cis/O-s-trans* (highlighted in green) into rotamer *trans/s-trans/O-s-cis* (highlighted in blue). If these rotations occur on the femto- to picosecond timescale, spectral diffusion[10] should occur. In figure

[10]Spectral diffusion can be described as an effect of the inhomogeneous broadened vibrational bands.

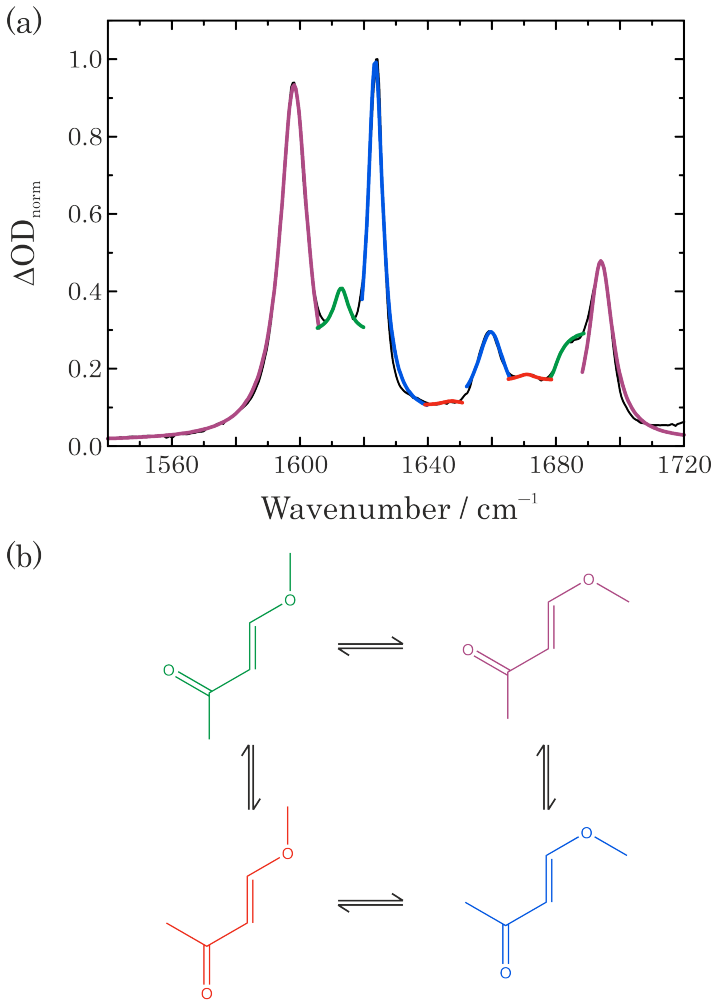

Figure 4.26: Visualization of assignment of vibrations to four rotamers of MBO.
(a) Stationary absorption spectrum of MBO in C_2Cl_4. Pairs of coupled oscillators are highlighted in purple (*trans/s-cis/O-s-cis*), green (*trans/s-cis/O-s-trans*), blue (*trans/s-trans/O-s-cis*), and orange (*trans/s-trans/O-s-trans*).
(b) Corresponding colored chemical structures of the four different rotamers.

4.27, contour plots at delay times of (a) 1.0 ps, (b) 3.0 ps, (c) 7.5 ps, and (d) 10.0 ps are shown.

As it can be observed, all apparent peaks exhibit a clear rounded shape, indicating that no spectral diffusion is present within the temporal resolution of the experimental setup. This invalidates the argument that chemical exchange in form of two consecutive restricted rotations occurs.

Herein, the overlap of different individual vibrational bands of each oscillator leads to an elongation of the peaks along the diagonal in the corresponding 2D-IR spectrum. A change of the oscillators surrounding results in slightly different vibrational transition frequencies and thus, in a loss of the diagonal shape of the signal contributions [56].

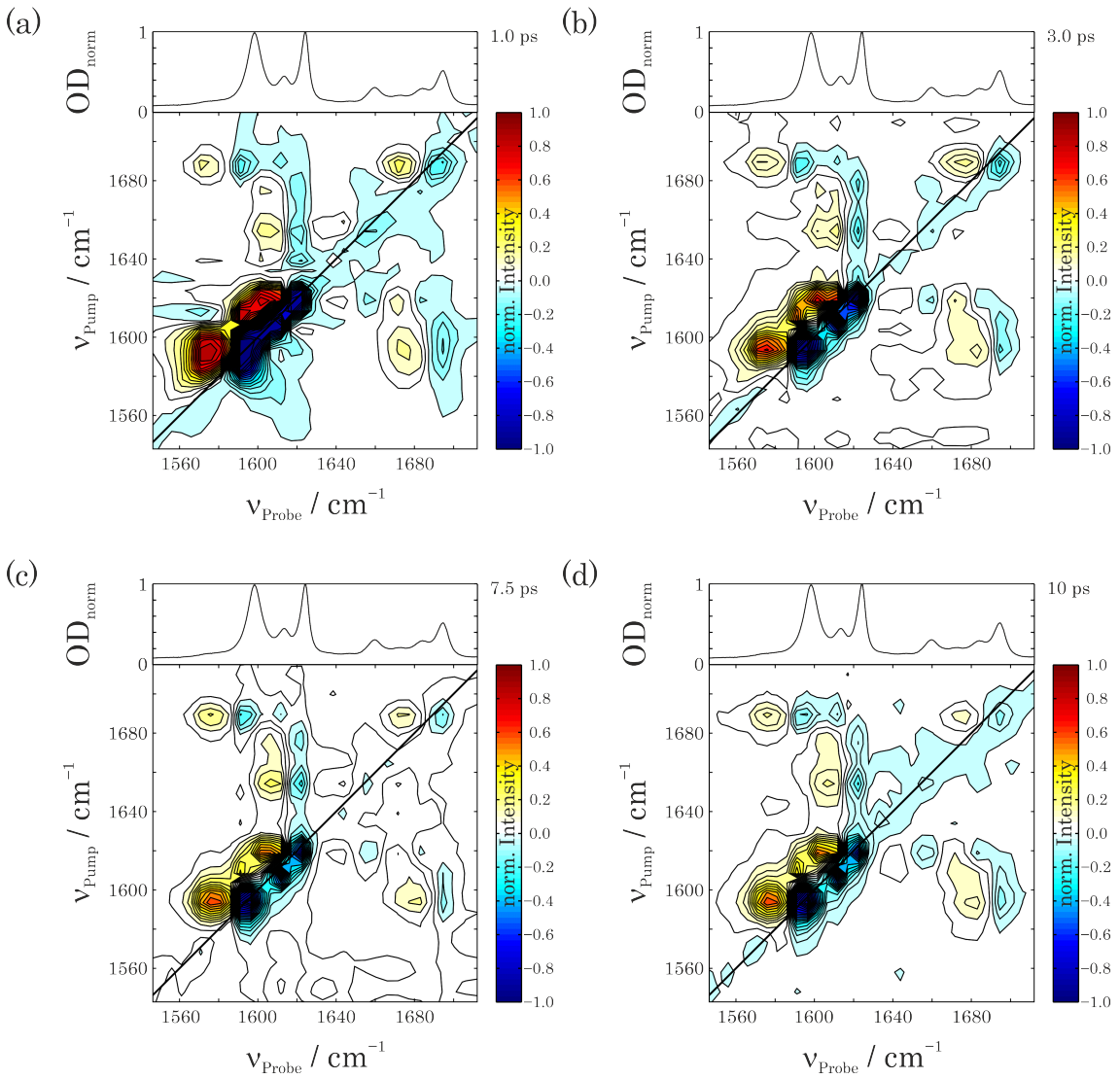

Figure 4.27: Normalized 2D-IR spectra of MBO in C_2Cl_4 for delay times of (a) 1.0 ps, (b) 3.0 ps, (c) 7.5 ps, and (d) 10 ps.

However, another assignable cause considers an intermolecular interaction, such as a dimerization, between the rotamers *trans/s-trans/O-s-cis* and *trans/s-cis/O-s-trans*. In order to develop strong attractive forces between both, the rotamers are aligned on top of one another. Due to the same partial charge distribution, which is shown in figure 4.25 (e), (f), the dimerization angle is about 180° and the dipole moments are orientated in parallel planes. This is shown in figure 4.28.

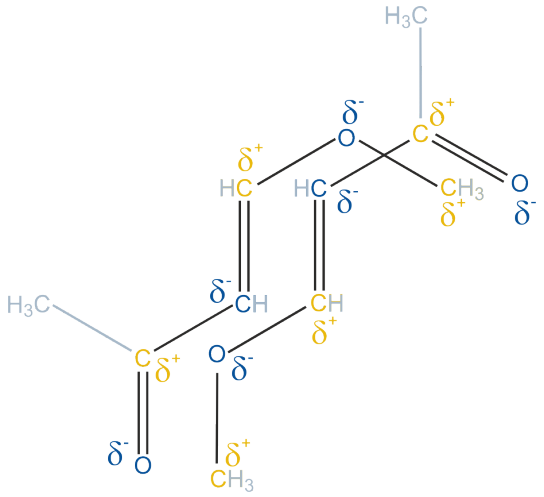

Figure 4.28: Interaction scheme of the rotamers *trans/s-trans/O-s-cis* and *trans/s-cis/O-s-trans* resulting in a dimerization. Positive partial charges are highlighted in yellow, negative ones in dark blue.

Here, negative partial charges are highlighted in blue, positive ones in yellow. It is recognizable that there is an alternating pattern of positive and negative partial charges between both rotamers resulting in an attractive interaction. Due to the fact that these interactions are formed instantaneously, the corresponding cross peak pattern is observable already at earliest delay times.

4.3.1 Conclusion III

Within this chapter, the investigation of *trans*-4-methoxy-but-3-en-2-one in C_2Cl_4 using two-dimensional infrared spectroscopy leads to the following results: The occurrence of four different rotamers due to restricted rotations around the C_{sp^2}-C_{sp^2} or C_{sp^2}-O single bonds resulted in eight different absorption bands within a spectral window of 1500 cm^{-1} to 1700 cm^{-1} indicating the ν(C=C) as well as ν(C=O) oscillator range. The linear absorption spectroscopy was only able to resolve seven out of eight absorption bands with different optical densities with a reasonable signal-to-noise ratio. Contrary to this, peak pattern for all suggested vibrations were observable within the

2D-IR spectra. Additionally, the Förster theory as well as theoretical calculations performed by Prof. Dr. P. Vöhringer were used to support the assignment of the cross peak pattern within the 2D-IR spectra to the rotamers. Finally, the emergence of another cross peak pattern involving two distinct ν(C=O) oscillators, namely those of the rotamers *trans/s-cis/O-s-trans* and *trans/s-trans/O-s-cis* was explained by an intermolecular interaction based on an alternating pattern of partial charges. Therefore, both rotamers are aligned on top of one other and are orientated in parallel planes, while one of the rotamers is rotated through 180°. Furthermore, the existence of spectral diffusion within the investigate temporal delay was not approved.

Chapter 5

Summary and Outlook

Within this work, the experimental setup of the pump-probe along with that of the 2D-IR spectrometer was presented and discussed. The reconstruction was highlighted and the implemented Pulse Shaper shortly explained.

Using the time-resolved pump probe spectroscopy, the ν_3 stretching vibration of the triatomic OCN^-, $O^{13}CN^-$ and $O^{13}C^{15}N^-$ as well as the CO_2 dissolved in H_2O were investigated for various thermodynamic conditions.

The broadening of the carbon dioxide's asymmetric stretching vibration was observed and explained by overlapping Lorentzian shaped bands. They were attributed to transitions from the bending mode $|0i0\rangle$ to the combination tone $|0i1\rangle$ with i quanta of energy in the bending mode ν_b of CO_2. The absorption spectra were computed based on the Kubo-Anderson stochastic theory under the assumption that the transition matrix elements are identical. The agreement between experimental observed and computed stationary IR spectra was quite good. The pump probe spectra featured two signal contributions within the investigated temperature range. They were attributed to the transient absorption, to the ground-state bleach and the stimulated emission. The analysis of the kinetic traces of the maxima of the TA and the GB/SE resulted in the lifetimes τ_1 and τ_0. They increased with rising temperature starting at around 9.0 ps at 303 K up to 17.1 ps at 603 K. In a pertubative treatment of the relaxation rate constants, i. e. the inverse of the lifetimes, Fermi's golden rule can be applied. With that, the underlying relaxation mechanism was identified to be rather a solvent-assisted sequential IVR than an intermolecular VET. Therefore, initially excited ν_{as} mode of CO_2 relaxed intramolecular into the ν_b mode with a time constant, which was extracted from the temperature-dependent stationary spectra. The lifetimes τ_0 and τ_1 were attributed to the intermolecular vibrational energy transfer from the bending mode of the carbon dioxide to the resonant vibrational mode of the solvent H_2O. Subsequently, the excess energy in the solvent was internally redistributed within 50 fs. The described relaxation mechanism is suitable to describe the observed temperature

dependence of the time constants.

The vibrational energy relaxation mechanism of the investigated aqueous cyanate solutions was assumed to follow a solvent-assisted sequential IVR, too. Here, the vibrational excess energy is redistributed intramolecular form the excited ν_3 stretching vibration into the bending mode ν_2 followed by an energy transfer to the librational modes of the solvent H_2O. The VER mechanisms of the OCN^- and its isotopologues in aqueous solution are identical and possess same time constants. This means that no isotope effect can be observed.

Comparing the different pseudohalide anions, the N_3^-, the OCN^-, the SCN^- and the $SeCN^-$, the lifetimes decrease in this order. In a pertubative treatment of the relaxation dynamics, the relaxation rate constants can be expressed by Fermi's golden rule. Herein, the interaction matrix element, which is proportional to the coupling strength between the solute and the solvent, can be determined for the thio- and selenocyanate solutions, since their VER mechanism follow a pure vibrational energy transfer from the excited stretching vibration to the solvent's resonant combination tone. The analysis resulted in a stronger coupling strength between the SCN^- anion and H_2O compared to the $SeCN^-$ anion in H_2O. This behavior was validated by the polarizability of the anions.

The underlying mechanism of the relaxation dynamics of OCN^- and its isotopologues in H_2O are similar to those of aqueous N_3^- and CO_2 solutions. Nevertheless, the lifetime of the azide and that of the cyanate are almost similar, while the lifetime of the carbon dioxide differs more than ninefold. This might indicate that the coupling strength between cyanate and H_2O or N_3^- and H_2O are stronger than between carbon dioxide and H_2O. This has to be investigated in future.

Finally, the powerful 2D-IR spectroscopy was applied to study the conformational dynamics of *trans*-4-methoxybut-3-en-2-one (MBO) in C_2Cl_4, a β-alkoxy-α,β-unsaturated ketone. A fast and efficient method was demonstrated to assign many overlapping cross peaks to their corresponding oscillators of different isomers, i .e. rotamers, of MBO. The Förster theory was therefore supportingly used. It was observed that two rotamers underwent a dimerization. The dimer was described as a stacking of the rotamers *trans/s-cis/O-s-trans* and *trans/s-trans/O-s-cis*, while one of them is rotated by through 180° to obtain an alternating pattern of partial charges.

Within the investigated temporal range, no pump-induced conformational dynamics, which are expressed in the absence of spectral diffusion, were observed. This means

that the conformers were in equilibrium to each another. In future, the time constants of the pump-induced changes of the absorption as well as the vibrational energy relaxation mechanism are investigated. Furthermore, an investigation of the dynamics depending on the concentration of MBO in C_2Cl_2 is of interest to investigate concentration-dependent effects on the dynamics.

Appendix

MATLAB Code

This appendix contains further information about the used MATLAB script for computing temperature-dependent absorption spectra of CO_2.

```
close all; clear all;

% Define Integers:
ny03 = 2383;     %cm-1
ny02 = 672.9;    %cm-1
ny01 = 1353.8;   %cm-1
x13 = -19.1;     %cm-1
x23 = -12.542;   %cm-1
x33 = -13.0;     %cm-1
x12 = -5.726;    %cm-1
x22 = 1.580;     %cm-1
x11 = -2.993;    %cm-1

T = (303:30:603);        % in K
h = 6.626*10^(-34);      % in J*s
clight = 2.998*10^8;     % in m/s
kB = 1.38065*10^(-23);   % in J/K
N = 12;

% Define variance Delta and coherence tauc:
Delta=[39.49,47.13,55.71,65.72,76.43,87.30,94.55,105.68,
   114.84,125.71,134.99]; % cm-1
tauc = [2.42*10^(-13),2.15*10^(-13),0.187*10^(-12)
   ,0.171*10^(-12),0.153*10^(-12),0.144*10^(-12)
   ,0.139*10^(-12),0.129*10^(-12),0.125*10^(-12)
   ,0.117*10^(-12),0.111*10^(-12)]; % s
```

```
23
24 Deltau = Delta.*10^2.*clight.*tauc;
25
26 % Calculation of nya:
27 nya001 = ny03+2*x33+x13*0.5+x23*0.5+2.4;
28 nya011 = nya001+2*x23+2.4;
29 nya021 = nya001+4*x23+2.4;
30 nya031 = nya001+6*x23+2.4;
31 nya041 = nya001+8*x23+2.4;
32 nya13C = 2277;
33
34 nya = vertcat(nya001',nya13C',nya011',nya021',nya031',
      nya041');
35
36 % Calculation of population according to Boltzmann
      distribution:
37 % First: Calculation of the partition function Q
38  q = zeros(size(nya,1),size(T,2));
39  n = [1 1 2 3 4 5];
40  for tt = 1:size(T,2)
41     for ti = 1:size(nya,1)
42       q(ti,tt)=exp(-(h*clight*nya(ti)*10^2*n(ti))/(kB*T(tt)
            ));
43     end
44  end
45  Q = sum(q,1);
46
47  % Second: Degeneracy factor g
48  g = [1 1 2 2 2 2];
49  % Third: Calculation of the population:
50  p = zeros(size(nya,1),size(T,2));
51  for to = 1:size(T,2)
52    for tz = 1:size(nya,1)
53      p(tz,to)=(exp(-(h*clight*nya(tz)*10^2*n(tz))/(kB*T(to)
           ))*g(tz))./(Q(to));
54    end
```

```
 end

% Define time function:
t = zeros(1,2^N-1);
for ii = 1:2^N-1
    t(ii) = (ii)/100*10^(-12);
end
Deltat = t(2)-t(1);

% Temeprature-dependent spectral shift of center wavenumber
   :
dn = [0 0.02 0.22 -0.14 -0.02 -0.43 -0.63 -1.23 -1.99 -2.70
    -3.0];
% Calculate phi function:
phi001 = zeros(1,size(t,2));
for ia = 1:size(t,2)
  for aa = 1:size(T,2)
   phi001(aa,ia) = exp(-(Delta(aa)*tauc(aa)*10^2*clight)
      ^2*(exp(-t(ia)/tauc(aa))+t(ia)/tauc(aa)-1))*cos(2*pi
      *(nya(1)+dn(aa))*10^2*clight*t(ia));
  end
end

phi13C = zeros(1,size(t,2));
for ib = 1:size(t,2)
  for ab = 1:size(T,2)
   phi13C(ab,ib) = exp(-(Delta(ab)*tauc(ab)*10^2*clight)
      ^2*(exp(-t(ib)/tauc(ab))+t(ib)/tauc(ab)-1))*cos(2*pi
      *(nya(2)+dn(aa))*10^2*clight*t(ib));
  end
end

phi011 = zeros(1,size(t,2));
for ic = 1:size(t,2)
  for ac = 1:size(T,2)
   phi011(ac,ic) = exp(-(Delta(ac)*tauc(ac)*10^2*clight)
```

```
      ^2*(exp(-t(ic)/tauc(ac))+t(ic)/tauc(ac)-1))*cos(2*pi
      *(nya(3)+dn(aa))*10^2*clight*t(ic));
  end
end

phi021 = zeros(1,size(t,2));
for id = 1:size(t,2)
  for ad = 1:size(T,2)
   phi021(ad,id) = exp(-(Delta(ad)*tauc(ad)*10^2*clight)
      ^2*(exp(-t(id)/tauc(ad))+t(id)/tauc(ad)-1))*cos(2*pi
      *(nya(4)+dn(aa))*10^2*clight*t(id));
  end
end

phi031 = zeros(1,size(t,2));
for ie = 1:size(t,2)
  for ae = 1:size(T,2)
   phi031(ae,ie) = exp(-(Delta(ae)*tauc(ae)*10^2*clight)
      ^2*(exp(-t(ie)/tauc(ae))+t(ie)/tauc(ae)-1))*cos(2*pi
      *(nya(5)+dn(aa))*10^2*clight*t(ie));
  end
end

phi041 = zeros(1,size(t,2));
for ig = 1:size(t,2)
  for ag = 1:size(T,2)
   phi041(ag,ig) = exp(-(Delta(ag)*tauc(ag)*10^2*clight)
      ^2*(exp(-t(ig)/tauc(ag))+t(ig)/tauc(ag)-1))*cos(2*pi
      *(nya(6)+dn(aa))*10^2*clight*t(ig));
  end
end

% Fourier transformation of phi for each temperature
S001 = zeros(size(T,2),size(t,2));
for ik = 1:size(T,2)
    S001(ik,:) = fft(phi001(ik,:));
```

```
113 end
114
115 S13C = zeros(size(T,2),size(t,2));
116 for ika = 1:size(T,2)
117     S13C(ika,:) = fft(phi13C(ika,:));
118 end
119
120 S011 = zeros(size(T,2),size(t,2));
121 for ikb = 1:size(T,2)
122     S011(ikb,:) = fft(phi011(ikb,:));
123 end
124
125 S021 = zeros(size(T,2),size(t,2));
126 for ikc = 1:size(T,2)
127     S021(ikc,:) = fft(phi021(ikc,:));
128 end
129
130 S031 = zeros(size(T,2),size(t,2));
131 for ikd = 1:size(T,2)
132     S031(ikd,:) = fft(phi031(ikd,:));
133 end
134
135 S041 = zeros(size(T,2),size(t,2));
136 for ike = 1:size(T,2)
137     S041(ik,:) = fft(phi041(ike,:));
138 end
139
140
141 % Use only the real part of the Fourier transformation
142 res001 = zeros(size(T,2),size(t,2));
143 for ij = 1:size(T,2)
144     res001(ij,:) = abs(S001(ij,:));
145 end
146
147 res13C = zeros(size(T,2),size(t,2));
148 for ija = 1:size(T,2)
```

```
149     res13C(ija,:) = abs(S13C(ija,:));
150 end
151
152 res011 = zeros(size(T,2),size(t,2));
153 for ijb = 1:size(T,2)
154     res011(ijb,:) = abs(S011(ijb,:));
155 end
156
157 res021 = zeros(size(T,2),size(t,2));
158 for ijc = 1:size(T,2)
159     res021(ijc,:) = abs(S021(ijc,:));
160 end
161
162 res031 = zeros(size(T,2),size(t,2));
163 for ijd = 1:size(T,2)
164     res031(ijd,:) = abs(S031(ijd,:));
165 end
166
167 res041 = zeros(size(T,2),size(t,2));
168 for ije = 1:size(T,2)
169     res041(ije,:) = abs(S041(ije,:));
170 end
171
172 % Calculate frequency axis:
173 nyaxis = zeros(1,size(t,2));
174 u = size(t,2);
175 for j = 1:u
176     nyaxis(j) = (1/clight*((j-1))/max(t))/100;
177 end
178
179 % Calculate spectra with population weighted fft Kubo
      function
180 Spectra = zeros(size(T,2),size(nyaxis,2));
181 for ab = 1:size(T,2)
182     Spectra(ab,:)=-0.5+res001(ab,:)*p(1,ab)+res13C(ab,:)*p
        (2,ab)*0.004+res011(ab,:)*p(3,ab)*20+res021(ab,:)*p
```

```
        (4,ab)+res031(ab,:)*p(5,ab)+res041(ab,:)*p(6,ab);
end

% Load experimental data:
M = load('DOD_alleT_original_baselinecorrection.txt');

% Plot calculated and orignial data
f = zeros(1,size(T,2));
for jj = 1:size(T,2)
    f(jj) = figure;
end

% Define scaling factor for calculated spectra
norm_orig = zeros(1,size(T,2));
norm_fit = zeros(1,size(T,2));
m = zeros(1,size(T,2));
for ji = 1:size(T,2)
    norm_orig(ji)=max(M(:,ji+1));
    norm_fit(ji) =max(Spectra(ji,:));
    m(ji)=norm_fit(ji)./norm_orig(ji);
end

% Plot scaled spectra and original data
Spectra_scal = zeros(size(T,2),size(nyaxis,2));
for j = 1:size(T,2)
    figure(f(j))
    Spectra_scal(j,:)=Spectra(j,:)/m(j);
    plot(nyaxis(2457:3378),Spectra_scal(j,2457:3378),'r');
    xlabel('Wavenumber');
    title(['Temperature is ',num2str(T(j)),'K']);
    ylabel('DOD');
    hold on;
    plot(M(:,1),M(:,j+1),'k');
end
hold off;

```

```
218 % Save data
219 Spektren=horzcat(nyaxis(2457:3378)',Spectra_scal
       (:,2457:3378)');
220 Simulationsparameter = horzcat(T',Delta',tauc',dn');
221
222 dlmwrite('simulierte_Spektren_alleT_pseudoVoigt_20200708.
       txt',Spektren);
223 dlmwrite('Simulationsparameter_pseudoVoigt_20200708.txt',
       Simulationsparameter);
```

List of Abbreviations

2D-IR	two-dimensional infrared
ΔOD	differential optical density
$\boldsymbol{\mu}$	transition dipole moment
AOM	acousto-optic modulator
DFG	difference frequency generation
DFT	density functional theory
fs	femtosecond
FWHM	full-width at half-maximum
GB	ground-state bleach
He:Ne	Helium-Neon laser
HO	harmonic oscillator
HR_p	high reflective for p-polarized light
HR_s	high reflective for s-polarized light
HTHP	high-temperature high-pressure
HT_p	high transmittant for p-polarized light
IR	infrared
IVR	intramolecular vibrational redistribution
LP	long-pass filter
MCT	mercury cadmium telluride
mid-IR	mid-infrared
NDIR	neutral density filters for IR light
OAP	off-axis parabolic
OPA	optical parametric amplifier
PD	photo diode

PFID	perturbed free induction decay
ps	picosecond
rds	rate determining step
RFL	reflected focal length
ROC	radius of curvature
SE	stimulated emission
TA	transient absorption
$\boldsymbol{t}_1$	temporal delay
Ti:Sa	Titan-Sapphire
TS	translation stage
VER	vibrational energy redistribution
VET	vibrational energy transfer

List of Figures

List of Tables

Bibliography

[1] The Nobel Price in Chemistry 1999. Nobel Media AB.

[2] D. Reiser and A. Laubereau. Picosecond Polarization Spectroscopy of Dye Molecules. *Berichte der Bunsengesellschaft für physikalische Chemie*, 86(12):1106–1114, 1982.

[3] J. Lindner and P. Vöhringer. Femtosecond Vibrational Spectroscopies and Applications to Hydrogen-Bond Dynamics in Condensed Phases. *Methods in Physical Chemistry*, pages 643–686, 2012.

[4] H. J. Foth, J. C. Polanyi, and H. H. Telle. Emission from Molecules and Reaction Intermediates in the Process of Falling Apart. *The Journal of Physical Chemistry*, 86(26):5027–5041, 1982.

[5] D. Imre, J. L. Kinsey, A. Sinha, and J. Krenos. Chemical Dynamics Studied by Emission Spectroscopy of Dissociating Molecules. *The Journal of Physical Chemistry*, 88(18):3956–3964, 1984.

[6] R. B. Metz, T. Kitsopoulos, A. Weaver, and D. M. Neumark. Study of the Transition State Region in the Cl+ HCl Reaction by Photoelectron Spectroscopy of $ClHCl^-$. *The Journal of Chemical Physics*, 88(2):1463–1465, 1988.

[7] L. R. Khundkar, J. L. Knee, and A. H. Zewail. Picosecond Photofragment Spectroscopy. I. Microcanonical State-to-State Rrates of the Reaction NCNO $\rightarrow$ CN+ NO. *The Journal of Chemical Physics*, 87(1):77–96, 1987.

[8] P. D. Kleiber, A. M. Lyyra, K. M. Sando, V. Zafiropulos, and W. C. Stwalley. Reactive Collision Dynamics by Far Wing Laser Scattering: Mg+ H_2. *The Journal of Chemical Physics*, 85(10):5493–5504, 1986.

[9] F. Siebert and P. Hildebrandt. *Vibrational Spectroscopy in Life Science*. John Wiley & Sons, 2008.

[10] S. J. Grabowski. *Hydrogen Bonding: New Insights*, volume 3. Springer, 2006.

[11] C. N. Banwell. *Fundamentals of Molecular Spectroscopy*. McGraw-Hill Book Company, London, third edition, 1983.

[12] P. Atkins and R. Friedman. *Molecular Quantum Mechanics*. Oxford University Press, New York, fourth edition, 2005.

[13] A. H. Zewail. Laser Femtochemistry. *Science*, 242(4886):1645–1653, 1988.

[14] K. Dahl, G. M. Sando, D. M. Fox, T. E. Sutto, and J. C. Owrutsky. Vibrational Spectroscopy and Dynamics of Small Anions in Ionic Liquid Solutions. *The Journal of Chemical Physics*, 123(8):084504, 2005.

[15] M. Olschewski, S. Knop, J. Lindner, and P. Vöhringer. From Single Hydrogen Bonds to Extended Hydrogen-Bond Wires: Low-Dimensional Model Systems for Vibrational Spectroscopy of Associated Liquids. *Angewandte Chemie International Edition*, 52(37):9634–9654, 2013.

[16] P. Hamm, M. Lim, and R. M. Hochstrasser. Structure of the Amide I Band of Peptides Measured by Femtosecond Nonlinear-Infrared Spectroscopy. *The Journal of Physical Chemistry B*, 102(31):6123–6138, 1998.

[17] A. Lauberau and W. Kaiser. Vibrational Dynamics of Liquids and Solids Investigated by Picosecond Light Pulses. *Reviews of Modern Physics*, 50(3):607–665, 1978.

[18] D. W. Oxtoby. Vibrational Relaxation in Liquids. *Annual Review of Physical Chemistry*, 32(1):77–101, 1981.

[19] T. Elsaesser and W. Kaiser. Vibrational and Vibronic Relaxation of Large Polyatomic Molecules in Liquids. *Annual Review of Physical Chemistry*, 42(1):83–107, 1991.

[20] G. A. Jeffrey. *An Introduction to Hydrogen Bonding*. Topics in Physical Chemistry. Oxford University Press, 1997.

[21] F. Franks. *The Physics and Physical Chemistry of Water*, volume 1. Springer Science & Business Media, 2012.

[22] D. Eisenberg and W. Kauzmann. *The Structure and Properties of Water*. Oxford University Press, 2005.

[23] J. C. Owrutsky, D. Raftery, and R. M. Hochstrasser. Vibrational Relaxation Dynamics in Solutions. *Annual Review of Physical Chemistry*, 45(1):519–555, 1994.

[24] V. Lenchenkov, C. She, and T. Lian. Vibrational Relaxation of CN Stretch of Pseudo-Halide Anions (OCN^-, SCN^-, and $SeCN^-$) in Polar Solvents. *The Journal of Physical Chemistry B*, 110(40):19990–19997, 2006.

[25] H. Lee, J.-H. Choi, and M. Cho. Vibrational Solvatochromism and Electrochromism of Cyanide, Thiocyanate, and Azide Anions in Water. *Physical Chemistry Chemical Physics*, 12(39):12658–12669, 2010.

[26] M. Li, J. Owrutsky, M. Sarisky, J. P. Culver, A. Yodh, and R. M. Hochstrasser. Vibrational and Rotational Relaxation Times of Solvated Molecular Ions. *Journal of Chemical Physics*, 98(7), 1992.

[27] M. Olschewski, S. Knop, J. Lindner, and P. Vöhringer. Vibrational Relaxation of Azide Ions in Liquid-to-Supercritical Water. *The Journal of Chemical Physics*, 134(21):214504, 2011.

[28] D. Czurlok, J. Gleim, J. Lindner, and P. Vöhringer. Vibrational Energy Relaxation of Thiocyanate Ions in Liquid-to-Supercritical Light and Heavy Water. A Fermi's Golden Rule Analysis. *The Journal of Physical Chemistry Letters*, 5(19):3373–3379, 2014.

[29] M. Olschewski. *Stationäre und zeitaufgelöste Infrarotspektroskopie von Azid-Anionen in flüssigem und überkritischen Wasser*. Diploma thesis, Mathematisch-Naturwissenschaftliche Fakultät der Rheinischen Friedrich-Wilhelms Universität Bonn, 2009.

[30] D. Czurlok. *Raman-Spektroskopie vonAzid-Ionen in flüssigem bis überkritischen Wasser*. Diploma thesis, Mathematisch-Naturwissenschaftliche Fakultät der Rheinischen Friedrich-Wilhelms Universität Bonn, 2011.

[31] D. Czurlok, M. von Domaros, M. Thomas, J. Gleim, J. Lindner, B. Kirchner, and P. Vöhringer. Femtosecond 2DIR Spectroscopy of the Nitrile Stretching Vibration of Thiocyanate Anions in Liquid-to-Supercritical Heavy Water. Spectral Diffusion and Libration-Induced Hydrogen-Bond Dynamics. *Physical Chemistry Chemical Physics*, 17(44):29776–29785, 2015.

[32] J. Gleim. *Time and Frequency Resolved Infrared Spectroscopy of Selenocyanate, ^{15}N-labelled Thiocyanate and Azide Anions in Liquid-to-Supercritical Water*. Masters thesis, Mathematisch-Naturwissenschaftliche Fakultät der Rheinischen Friedrich-Wilhelms Universität Bonn, 2015.

[33] Umweltbundesamt. Carbon Capture and Storage, January 2021. downloaded on 24.05.2021.

[34] B. Metz, O. Davidson, H. de Conick, M. Loos, and L. Meyer, editors. *IPCC Special Report on Carbon Dioxide Capture and Storage*, 2005.

[35] V. Alizadeh, L. Esser, and B. Kirchner. How is CO_2 Absorbed Into a Deep Eutectic Solvent? *The Journal of Chemical Physics*, 154(9):094503, 2021.

[36] R. S. Haszeldine. Carbon Capture and Storage: How Green can Black be? *Science*, 325(5948):1647–1652, 2009.

[37] M. E. Boot-Handford, J. C. Abanades, E. J. Anthony, M. J. Blunt, S. Brandani, N. Mac Dowell, J. R. Fernández, M.-C. Ferrari, R. Gross, J. P. Hallett, et al. Carbon Capture and Storage Update. *Energy & Environmental Science*, 7(1):130–189, 2014.

[38] C. Azar, K. Lindgren, M. Obersteiner, K. Riahi, D. P. van Vuuren, K. M. G. J. den Elzen, K. Möllersten, and E. D. Larson. The Feasibility of low CO_2 Concentration Targets and the Role of Bio-Energy with Carbon Capture and Storage (BECCS). *Climatic Change*, 100(1):195–202, 2010.

[39] S. M. Benson and T. Surles. Carbon Capture and Storage: An Overview with Emphasis on Capture and Storage in Deep Geological Formations. *Proceedings of the IEEE*, 94(10):1795–1805, 2006.

[40] M. L. Szulczewski, C. W. MacMinn, H. J. Herzog, and R. Juanes. Lifetime of Carbon Capture and Storage as a Climate-Change Mitigation Technology. *National Acad Sciences*, 109(14):5185–5189, 2012.

[41] K. Z. House, D. P. Schrag, C. F. Harvey, and K. S. Lackner. Permanent Carbon Dioxide Storage in Deep-Sea Sediments. *National Acad Sciences*, 103(33):12291–12295, 2006.

[42] B. Kirchner and B. Intemann. Catch the Carbon Dioxide. *Nature Chemistry*, 8(5):401–402, 2016.

[43] S. Zahn, M. Brehm, M. Bruessel, O. Holloczki, M. Kohagen, S. Lehmann, F. Malberg, A. S. Pensado, M. Schoeppke, H. Weber, et al. Understanding Ionic Liquids from Theoretical Methods. *Journal of Molecular Liquids*, 192:71–76, 2014.

[44] T. Brinzer, E. J. Berquist, S. Dutta, C. A. Johnson, C. S. Krisher, D. S. Lambrecht, and S. Garrett Roe. Ultrafast Vibrational Spectroscopy (2D-IR) of CO_2 in Ionic Liquids: Carbon Capture from Carbon Dioxide's Point of View. *The Journal of Chemical Physics*, 142(21):212425, 2015.

[45] C. H. Giammanco, P. L. Kramer, S. A. Yamada, J. Nishida, A. Tamimi, and M. D. Fayer. Carbon Dioxide in an Ionic Liquid: Structural and Rotational Dynamics. *The Journal of Chemical Physics*, 144(10):104506, 2016.

[46] C. H. Giammanco, S. A. Yamada, P. L. Kramer, A. Tamimi, and M. D. Fayer. Structural and Rotational Dynamics of Carbon Dioxide in 1-Alkyl-3-methylimidazolium Bis(trifluoromethylsulfonyl)imide Ionic Liquids: The Effect of Chain Length. *The Journal of Physical Chemistry B*, 120(27), 2016.

[47] T. Brinzer, C. A. Daly Jr, C. Allison, S. Garrett Roe, and S. A. Corcelli. Modeling Carbon Dioxide Vibrational Frequencies in Ionic Liquids: III. Dynamics and Spectroscopy. *The Journal of Physical Chemistry B*, 122(38):8931–8942, 2018.

[48] C. A. Daly Jr, C Allison, and S. A. Corcelli. Modeling Carbon Dioxide Vibrational Frequencies in Ionic Liquids: V. Temperature Dependence. *The Journal of Physical Chemistry B*, 123(17):3797–3803, 2019.

[49] P. Hamm, M. Lim, and R. M. Hochstrasser. Vibrational Relaxation and Dephasing of Small Molecules Strongly Interacting with Water. In *Ultrafast Phenomena XI*, pages 514–516. Springer Berlin Heidelberg, 1998.

[50] Y. Liu, K. Bakshi, P. Zavalij, and M. P. Doyle. Pericyclic Reaction of a Zwitterionic Salt of an Enedione-diazoester. A Novel Strategy for the Synthesis of Highly Functionalized Resorcinols. *Organic Letters*, 12(19):4304–4307, 2010.

[51] J. I. Seeman. Effect of Conformational Change on Reactivity in Organic Chemistry. Evaluations, Applications, and Extensions of Curtin-Hammett Winstein-Holness Kinetics. *Chemical Reviews*, 83(2):83–134, 1983.

[52] S. Zhang, H. Neumann, and M. Beller. Synthesis of α, β-Unsaturated Carbonyl Compounds by Carbonylation Reactions. *Chemical Society Reviews*, 49(10):3187–3210, 2020.

[53] Z. Shi, C. Grohmann, and F. Glorius. Mild Rhodium (III)-Catalyzed Cyclization of Amides with α, β-Unsaturated Aldehydes and Ketones to Azepinones: Application to the Synthesis of the Homoprotoberberine Framework. *Angewandte Chemie International Edition*, 52(20):5393–5397, 2013.

[54] A. Jacobi von Wangelin, H. Neumann, D. Gördes, S. Klaus, and D. Strübing. Multicomponent Coupling Reactions for Organic Synthesis: Chemoselective Reactions with Amide–Aldehyde Mixtures. *Chemistry – A European Journal*, 9(18):4286–4294, 2003.

[55] M. Breuer, K. Ditrich, T. Habicher, B. Hauer, M. Keßeler, R. Stürmer, and T. Zelinski. Industrial Methods for the Production of Optically Active Intermediates. *Angewandte Chemie International Edition*, 43(7):788–824, 2004.

[56] P. Hamm and M. Zanni. *Concepts and Methods of 2D-Infrared Spectroscopy*. Cambridge University Press, Cambridge, 2011.

[57] J. Bredenbeck, J. Helbing, C. Kolano, and P. Hamm. Ultrafast 2D–IR Spectroscopy of Transient Species. *Chem Phys Chem*, 8(12):1747–1756, 2007.

[58] S. Knop, M. Olschewski, and P. Vöhringer. Femtosecond Two-Dimensional Infrared Spectroscopy of Synthetic Hydrogen-Bonded Wires: From Homogeneous to Inhomogeneous Dynamics. In *EPJ Web of Conferences*, volume 41, page 06001. EDP Sciences, 2013.

[59] R. M. Hochstrasser. Two-Dimensional Spectroscopy at Infrared and Optical Frequencies. *Proceedings of the National Academy of Sciences*, 104(36):14190–14196, 2007.

[60] J. J. Loparo, S. T. Roberts, and A. Tokmakoff. Multidimensional Infrared Spectroscopy of Water. I. Vibrational Dynamics in Two-Dimensional IR Line Shapes. *The Journal of Chemical Physics*, 125(19):194521, 2006.

[61] G. Wedler. *Lehrbuch der Physikalischen Chemie*. WILEY-VCH, fifth edition, 2004.

[62] J. M. Hollas. *Modern Spectroscopy*. John Wiley & Sons, fourth edition, 2004.

[63] P. M. Morse. Diatomic Molecules According to the Wave Mechanics. II. Vibrational Levels. *Physical Review*, 34(1):57, 1929.

[64] R. Schröder and E. R. Lippincott. Potential Function Model of Hydrogen Bonds. II. *The Journal of Physical Chemistry*, 61(7):921–928, 1957.

[65] E. R. Lippincott and R. Schröder. One-Dimensional Model of the Hydrogen Bond. *The Journal of Chemical Physics*, 23(6):1099–1106, 1955.

[66] J. Seehusen. *Schwingungsdynamik von intra- und intermolekularen Wasserstoffbrückenbindungen*. PhD thesis, Mathematisch-Naturwissenschaftliche Fakultät der Rheinischen Friedrich-Wilhelms Universität Bonn, 2010.

[67] M. Weissbluth. *Atoms and Molecules*. Academic Press New York, 1978.

[68] V. Cervetto, J. Helbing, J. Bredenbeck, and P. Hamm. Double-Resonance versus Pulsed Fourier Transform Two-Dimensional Infrared Spectroscopy: An Experimental and Theoretical Comparison. *The Journal of Chemical Physics*, 121(12):5935–5942, 2004.

[69] C. Rulliere. *Femtosecond Laser Pulses - Principles and Experiments*. Springer, second edition, 2005.

[70] P. Hamm, R. A. Kaindl, and J. Stenger. Noise Suppression in Femtosecond Mid-Infrared Light Sources. *Optics Letters*, 25(24):1798–1800, 2000.

[71] R. A. Kaindl, M. Wurm, K. Reimann, P. Hamm, A. M. Weiner, and M. Woerner. Generation, Shaping, and Characterization of Intense Femtosecond Pulses Tunable from 3 to 20 μm. *Journal of the Optical Society of America B*, 17(12):2086–2094, 2000.

[72] L. P. DeFlores, R. A. Nicodemus, and A. Tokmakoff. Two-Dimensional Fourier Transform Spectroscopy in the Pump-Probe Geometry. *Optics Letters*, 32(20):2966–2968, 2007.

[73] S.-H. Shim, D. B. Strasfeld, Y. L. Ling, and M. T. Zanni. Automated 2D IR Spectroscopy using a Mid-IR Pulse Shaper and Application of this Technology to the Human Islet Amyloid Polypeptide. *Proceedings of the National Academy of Sciences*, 104(36):14197–14202, 2007.

[74] D. Ehmer. *Ultraschnelle zweidimensionale Infrarotspektroskopie und ab initio Berechnungen an OH- und NH-Streckschwingungen*. PhD thesis, Mathematisch-Naturwissenschaftliche Fakultät der Rheinischen Friedrich-Wilhelms Universität Bonn, 2013.

[75] W. T. Rock. *2D-IR done Cheaper, Easier, and Faster: Design and Applications*. PhD thesis, University of Iowa, 2012.

[76] J. Helbing and P. Hamm. Compact Implementation of Fourier Transform Two-Dimensional IR Spectroscopy without Phase Ambiguity. *Journal of the Optical Society of America B*, 28(1):171–178, 2011.

[77] S.-H. Shim and M. T. Zanni. How to Turn your Pump−Probe Instrument into a Multidimensional Spectrometer: 2D-IR and Vis Spectroscopies via Pulse Shaping. *Physical Chemistry Chemical Physics*, 11(5):748–761, 2009.

[78] M. Olschewski. *Von einzelnen H-Brücken zum chemischen Rezeptor: 2D-IR-Spektroskopie wasserstoffverbrückter Systeme*. PhD thesis, Mathematisch-Naturwissenschaftliche Fakultät der Rheinischen Friedrich-Wilhelms Universität Bonn, 2013.

[79] W. Demtröder. *Laserspektroskopie 1 - Grundlagen*. Springer-Verlag Berlin Heidelberg, 6th edition, 2011.

[80] R. Kubo. A Stochastic Theory of Line Shape. *Stochastic Processes in Chemical Physics*, 15:101–127, 1969.

[81] P. W. Anderson. A Mathematical Model for the Narrowing of Spectral Lines by Exchange or Motion. *Journal of the Physical Society of Japan*, 9(3):316–339, 1954.

[82] A. Nitzan. *Chemical Dynamics in Condensed Phases - Relaxation, Transfer and Reactions in Condensed Molecular Systems*. Oxford University Press, 2006.

[83] R. Kubo, M. Toda, and N. Hashitsume. *Statistical Physics II – Nonequilibrium Statistical Mechanics*. Springer, 1998.

[84] A. Wachter and H. Hoeber. *Repetitorium Theoretische Physik*. Springer Verlag Heidelberg, second edition, 2005.

[85] P. A. M. Dirac. The Quantum Theory of the Emission and Absorption of Radiation. *Proceedings of the Royal Society of London. Series A, Containing Papers of a Mathematical and Physical Character*, 114(767):243–265, 1927.

[86] V. M. Kenkre, A. Tokmakoff, and M. D. Fayer. Theory of Vibrational Relaxation of Polyatomic Molecules in Liquids. *The Journal of Chemical Physics*, 101(12):10618–10629, 1994.

[87] W. W. Parson. *Modern Optical Spectroscopy*. Springer Verlag GmbH, second edition, 2015.

[88] C. Froehly, B. Colombeau, and M. Vampouille. II. Shaping and Analysis of Picosecond Light Pulses. In *Progress in Optics*, volume 20, pages 63–153. Elsevier, 1983.

[89] M. M. Wefers and K. A. Nelson. Analysis of Programmable Ultrashort Waveform Generation using Liquid-Crystal Spatial Light Modulators. *Journal of Optcial Society America B*, 12(7):1343–1362, 1995.

[90] C. W. Hillegas, J. X. Tull, D. Goswami, D. Strickland, and W. S. Warren. Femtosecond Laser Pulse Shaping by use of Microsecond Radio-Frequency Pulses. *Optics Letters*, 19(10):737–739, 1994.

[91] A. Ghosh, A. L. Serrano, T. A. Oudenhoven, J. S. Ostrander, E. C. Eklund, A. F. Blair, and M. T. Zanni. Experimental Implementations of 2D IR Spectroscopy through a Horizontal Pulse Shaper Design and a Focal Plane Array Detector. *Optics Letters*, 41(3):524–527, 2016.

[92] A. Korpel. Acousto-Optics – A Review of Fundamentals. *Proceedings of the IEEE*, 69(1):48–53, 1981.

[93] IOSMET CORP., 5623 Port Royal Rd, Springfield, VA 22151, USA. *Application Note AN0510 Acousto-Optic Modulation*.

[94] S.-H. Shim, D. B. Strasfeld, E. C. Fulmer, and M. T. Zanni. Femtosecond Pulse Shaping Directly in the Mid-IR Using Acousto-Optic Modulation. *Optics Letters*, 31(6):838–840, 2006.

[95] M. C. Gupta and J. Ballato, editors. *The Handbook of Photonics*, chapter Optical Modulators, pages 520–561. CRC Press, 2007.

[96] S.-H. Shim, D. B. Strasfeld, and M. T. Zanni. Generation and Characterization of Phase and Amplitude Shaped Femtosecond Mid-IR Pulses. *Optics Express*, 14(26):13120–13130, 2006.

[97] P. Vöhringer. "private communication".

[98] J. Lindner. "private communication".

[99] PhaseTech Spectroscopy, Inc., 2810 Crossroads Dr., Suite 4000, Madison, WI, USA. *PhaseTech QuickShape IR*.

[100] IOSMET CORP., 5623 Port Royal Rd, Springfield, VA 22151, USA. *Large Apperture GE Deflector*.

[101] H.-J. Bartsch. *Taschenbuch mathematischer Formeln*. 7. – 10. Verlag Harry Deutsch Thun, 1987.

[102] S. Kratz. *Geminale Rekombinationsdynamik solvatisierter Elektronen in flüssigem bis überkritischem Wasser*. PhD thesis, Mathematisch-Naturwissenschaftliche Fakultät der Rheinischen Friedrich-Wilhelms Universität Bonn, 2013.

[103] J. Urbanek. *Multiphoton Ionization and Recombination Dynamics in Liquid-to-Supercritical Ammonia*. PhD thesis, Mathematisch-Naturwissenschaftliche Fakultät der Rheinischen Friedrich-Wilhelms Universität Bonn, 2014.

[104] Y. E. Gorbaty, E. Venardou, E. Garcia Verdugo, and M. Poliakoff. High-Temperature and High-Pressure Cell for Kinetic Measurements of Supercritical Fluids Reactions with the Use of Ultraviolet-Visible Spectroscopy. *Review of Scientific Instruments*, 74(6):3073–3076, 2003.

[105] D. R. Vij, editor. *Handbook of Applied Solid State Spectroscopy*, chapter Fourier Transform Infrared Spectroscopy, pages 411–450. Springer US, 2006.

[106] D. Czurlok. *Femtosekunden-Infrarot-Spektroskopie von dreiatomigen Pseudohalogenid-Ionen sowie organischen und anorganischen Pseudohalogenid-Verbindungen*. PhD thesis, Mathematisch-Naturwissenschaftliche Fakultät der Rheinischen Friedrich-Wilhelms Universität Bonn, 2015.

[107] D. Langmuir. Aqueous environmental. *Geochemistry Prentice Hall, NJ*, 1997.

[108] A. H. England, A. M. Duffin, C. P. Schwartz, J. S. Uejio, D. Prendergast, and R. J. Saykally. On the Hydration and Hydrolysis of Carbon Dioxide. *Chemical Physics Letters*, 514(4-6):187–195, 2011.

[109] D. Berg and A. Patterson Jr. The High Field Conductance of Aqueous Solutions of Carbon Dioxide at 25°C. The True Ionization Constant of Carbonic Acid. *Journal of the American Chemical Society*, 75(21):5197–5200, 1953.

[110] M. L. Kieke, J. W. Schoppelrei, and T. B. Brill. Spectroscopy of Hydrothermal Reactions. 1. The CO_2 - H_2O System and Kinetics of Urea Decomposition in an FTIR Spectroscopy Flow Reactor Cell Operable to 725 K and 335 bar. *The Journal of Physical Chemistry*, 100(18):7455–7462, 1996.

[111] S. R. Zukowski, P. D. Mitev, K. Hermansson, and D. Ben Amotz. CO_2 Hydration Shell Structure and Transformation. *The Journal of Physical Chemistry Letters*, 8(13):2971–2975, 2017.

[112] A. K. Wyczalkowska, Kh. S. Abdulkadirova, M. A. Anisimov, and J. V. Sengers. Thermodynamic Properties of H_2O and D_2O in the Critical Region. *The Journal of Chemical Physics*, 113(12):4985, 2000.

[113] R. A. Nicodemus, S. A. Corcelli, J. L. Skinner, and A. Tokmakoff. Collective Hydrogen Bond Reorganization in Water Studied with Temperature-Dependent Ultrafast Infrared Spectroscopy. *The Journal of Physical Chemistry B*, 115(18):5604–5616, 2011.

[114] A. Chedin. The Carbon Dioxide Molecule: Potential, Spectroscopic, and Molecular Constants from its Infrared Spectrum. *Journal of Molecular Spectroscopy*, 76(1-3):430–491, 1979.

[115] P. Hamm, S. M. Ohline, and W. Zinth. Vibrational Cooling after Ultrafast Photoisomerization of Azobenzene Measured by Femtosecond Infrared Spectroscopy. *The Journal of Chemical Physics*, 106(2):519–529, 1997.

[116] W. D. Allen, Y. Yamaguchi, A. G. Császár, D. A. Clabo Jr, R. B. Remington, and H. F. Schaefer III. A Systematic Study of Molecular Vibrational Anharmonicity and Vibration-Rotation Interaction by Self-Consistent-Field Higher-Derivative Methods. Linear Polyatomic Molecules. *Chemical Physics*, 145(3):427–466, 1990.

[117] H. L. Schläfer and O. Kling. Bedeutung isosbestischer Punkte für die spektrophotometrische Untersuchung chemischer Zeitreaktionen und Gleichgewichte. *Angewandte Chemie*, 68(21):667–670, 1956.

[118] P. Hamm. Coherent Effects in Femtosecond Infrared Spectroscopy. *Chemical Physics*, 200(3):415–429, 1995.

[119] A. Nitzan, S. Mukamel, and J. Jortner. Energy Gap Law for Vibrational Relaxation of a Molecule in a Dense Medium. *The Journal of Chemical Physics*, 63(1):200–207, 1975.

[120] M. L. Cowan, B. D. Bruner, N. Huse, J. R. Dwyer, B. Chugh, E. T. J. Nibbering, T. Elsaesser, and R. J. D. Miller. Ultrafast Memory Loss and Energy Redistribution in the Hydrogen Bond Network of Liquid H_2O. *Nature*, 434:199–202, 2005.

[121] E. Fermi. Über den Ramaneffekt des Kohlendioxyds. *Zeitschrift für Physik*, 71(3):250–259, 1931.

[122] D. M. Dennison. The Infra-Red Spectra of Polyatomic Molecules. Part II. *Reviews of Modern Physics*, 12(3):175, 1940.

[123] A. Kandratsenka, J. Schroeder, D. Schwarzer, and V. S. Vikhrenko. Molecular Dynamics Modeling of Cooling of Vibrationally Highly Excited Carbon Dioxide Produced in the Photodissociation of Organic Peroxides in Solution. *Physical Chemistry Chemical Physics*, 7(6):1205–1213, 2005.

[124] V. Schettino and I. C. Hisatsune. Infrared Spectrum of Matrix-Isolated Cyanate Ion. I. Vibrational Analysis, Bandwidths, and Absolute Intensities in Potassium Halides. *The Journal of Chemical Physics*, 52(1):9–27, 1970.

[125] T. Tassaing, Y. Danten, and M. Besnard. Infrared Spectroscopic Study of Hydrogen-Bonding in Water at High Temperature and Pressure. *Journal of Molecular Liquids*, 101(1):149–158, 2002.

[126] G. E. Walrafen, M. R. Fisher, M. S. Hokmabadi, and W.-H. Yang. Temperature Dependence of the Low-and High-Frequency Raman Scattering from Liquid Water. *The Journal of Chemical Physics*, 85(12):6970–6982, 1986.

[127] K. Ohta and K. Tominaga. Vibrational Population Relaxation of Thiocyanate Ion in Polar Solvents Studied by Ultrafast Infrared Spectroscopy. *Chemical Physics Letters*, 429(1-3):136–140, 2006.

[128] A. Morita and S. Kato. Vibrational Relaxation of Azide Ion in Water: The Role of Intramolecular Charge Fluctuaions and Solvent-Induced Vibrational Coupling. *The Journal of Chemical Physics*, 109(13):5511–5523, 1998.

[129] H. Maekawa, K. Ohta, and K. Tominaga. Spectral Diffusion of the Anti-Symmetric Stretching Mode of Azide Ion in Reverse Micelle Studied by Infrared Three-Pulse Photon Echo Method. *Physical Chemistry Chemical Physics*, 6(16):4074–4077, 2004.

[130] F. Neese. Prediction of Molecular Properties and Molecular Spectroscopy with Density Functional Theory: From Fundamental Theory to Exchange-Coupling. *Coordination Chemistry Reviews*, 253(5-6):526–563, 2009.

[131] A. D. Becke. Density-Functional Thermochemistry. III. The Role of Exact Exchange. *Journal of Chemical Physics*, 98(7):5648–5652, 1993.

[132] A. Schäfer, H. Horn, and R. Ahlrichs. Fully Optimized Contracted Gaussian Basis Sets for Atoms Li to Kr. *The Journal of Chemical Physics*, 97(4):2571–2577, 1992.

[133] A. Schäfer, C. Huber, and R. Ahlrichs. Fully Optimized Contracted Gaussian Basis Sets of Triple Zeta Valence Quality for Atoms Li to Kr. *The Journal of Chemical Physics*, 100(8):5829–5835, 1994.

[134] K. Eichkorn, O. Treutler, H. Öhm, M. Häser, and R. Ahlrichs. Auxiliary Basis Sets to Approximate Coulomb Potentials. *Chemical Physics Letters*, 240(4):283–290, 1995.

[135] W. P. Hayes and C. J. Timmons. The C=O and C=C Fundamental and Overtone Stretching Bands and the Electronic Absorption Bands of some α,β-Unsaturated Ketones. *Spectrochimica Acta Part A: Molecular Spectroscopy*, 24(4):323–334, 1968.

[136] J. Dabrowski and M. Tencer. Infrared Spectra and Structure of Substituted Unsaturated Carbonyl Compounds. XIX. Four Component Conformational Equilibria in β-Ketoaldehyde Trans Enol Ethers. *Bulletin of the Chemical Society of Japan*, 48(4):1310–1314, 1975.

[137] D. E. Mann, N. Acquista, and K. Plyler. Vibrational Spectra of Tetrafluoroethylene and Tetrachloroethylene. *Journal of Research of the National Bureau of Standards*, 52(2), 1954.

[138] M. J. Frisch, G. W. Trucks, H. B. Schlegel, G. E. Scuseria, M. A. Robb, J. R. Cheeseman, G. Scalmani, V. Barone, G. A. Petersson, H. Nakatsuji, X. Li, M. Caricato, A. V. Marenich, J. Bloino, B. G. Janesko, R. Gomperts, B. Mennucci, H. P. Hratchian, J. V. Ortiz, A. F. Izmaylov, J. L. Sonnenberg, D. Williams Young, F. Ding, F. Lipparini, F. Egidi, J. Goings, B. Peng, A. Petrone, T. Henderson, D. Ranasinghe, V. G. Zakrzewski, J. Gao, N. Rega, G. Zheng, W. Liang, M. Hada, M. Ehara, K. Toyota, R. Fukuda, J. Hasegawa, M. Ishida, T. Nakajima, Y. Honda, O. Kitao, H. Nakai, T. Vreven, K. Throssell, Jr. J. A. Montgomery, J. E. Peralta, F. Ogliaro, M. J. Bearpark, J. J. Heyd, E. N. Brothers, K. N. Kudin, V. N. Staroverov, T. A. Keith, R. Kobayashi, J. Normand, K. Raghavachari, A. P. Rendell, J. C. Burant, S. S. Iyengar, J. Tomasi, M. Cossi, J. M. Millam, M. Klene, C. Adamo, R. Cammi, J. W. Ochterski, R. L. Martin, K. Morokuma, O. Farkas, J. B. Foresman, and D. J. Fox. Gaussian 16 Revision C.01, 2016. Gaussian Inc. Wallingford CT.

[139] S. Grimme, S. Ehrlich, and L. Goerigk. Effect of the Damping Function in Dispersion Corrected Density Functional Theory. *Journal of Computational Chemistry*, 32:1456–1465, 2011.

[140] F. Weigend and R. Ahlrichs. Balanced Basis Sets of Split Valence and Quadruple Zeta Valence Qualtiy for H to Rn: Design and Assessment of Accuracy. *Physical Chemistry Chemical Physics*, 7:3297–3305, 2005.

[141] J. Tomasi, B. Mennucci, and R. Cammi. Quantum Mechanical Continuum Solvation Models. *Chemical Reviews*, 105:2999–3093, 2005.

[142] D. R. Lide, editor. *CRC Handbook of Chemistry and Physics*. CRC Press, New York, 84th edition, 2004.

Danksagung

An dieser Stelle möchte ich mich bei verschiedenen Personen bedanken. An erster Stelle gilt mein Dank meinen Doktorvater, Prof. Dr. Vöhringer, der es mir ermöglicht hat, an einem faszienierendem und komplexen Experiment zu promovieren. Darüber hinaus danke ich Prof. Dr. Kirchner für die Übernahme des Zweitgutachtens, sowie Prof. Dr. Lützen und Prof. Dr. Lang für ihre Teilnahme an der Prüfungskommission

Weiterhin möchte ich mich bei Herrn Dr. Jörg Lindner für die Unterstützung bei Fragen rund um den neuen Aufbau des Experiments, sowie Zeit und Geduld beim Korrekturlesen bedanken.

Mein Dank gilt ebenfalls der Feinmechanikwerkstatt rund um Herrn Königshoven und der Elektronikwerkstatt um Herrn Paulig. Ohne ihre Unterstützung und Mithilfe bei der Umsetzung der Ideen wäre das Experiment nicht das, was es heute ist.

Daneben möchte ich mich bei der Arbeitsgruppe bedanken für die schöne gemeinsame Zeit, die kulinarischen Höhepunkte beim Mittagessen, gelegentliches Feiern und die gute Stimmung.

Mein ganz besonderer Dank gilt meiner Familie: für eure immerwährende Unterstützung, euer offenes Ohr, einfach für alles! Schön, dass es euch gibt!